Multi-Component and Multi-Dimensional Mathematical Modeling of Solid Oxide Fuel Cells

by
Mohammed Mujtaba Hussain

A thesis
presented to the University of Waterloo
in fulfillment of the
thesis requirement for the degree of
Doctor of Philosophy
in
Mechanical Engineering

Waterloo, Ontario, Canada, 2008

I hereby declare that I am the sole author of this thesis. This is a true copy of the thesis, including any required final revisions, as accepted by my examiners.

I understand that my thesis may be made electronically available to the public.

Mohammed Mujtaba Hussain

Abstract

Solid oxide fuel cells (SOFCs) are solid-state ceramic cells, typically operating between 1073 K and 1273 K. Because of high operating temperature, SOFCs are mostly applicable in stationary power generation. Among various configurations in which SOFCs exist, the planar configuration of solid oxide fuel cell (SOFC) has the potential to offer high power density due to shorter current path. Moreover, the planar configuration of SOFC is simple to stack and closely resemble the stacking arrangement of polymer electrolyte membrane (PEM) fuel cells. However, due to high operating temperature, there are problems associated with the development and commercialization of planar SOFCs, such as requirement of high temperature gas seals, internal stresses in cell components, and high material and manufacturing costs. Mathematical modeling is an essential tool for the advancement of SOFC technology. Mathematical models can help in gaining insights on the processes occurring inside the fuel cell, and can also aid in the design and optimization of fuel cells by examining the effect of various operating and design conditions on performance.

A multi-component and multi-dimensional mathematical model of SOFCs has been developed in this thesis research. One of the novelties of the present model is its treatment of electrodes. An electrode in the present model is treated as two distinct layers referred to as the backing layer and the reaction zone layer. Reaction zone layers are thin layers in the vicinity of the electrolyte layer where electrochemical reactions occur to produce oxide ions, electrons and water vapor. The other important feature of the present model is its flexibility in fuel choice, which implies not only pure hydrogen but also any reformate composition can be used as a fuel. The modified Stefan-Maxwell equations incorporating Knudsen diffusion are used to model multi-component diffusion in the porous backing and reaction zone layers. The coupled governing equations of species, charge and energy along with the constitutive equations in different layers of the cell are solved for numerical solution using the finite volume method and developed code written in the computer language of C++. In addition, the developed numerical model is validated with various experimental data sets published in the open literature. Moreover, it is verified that the electrode in an SOFC can be treated as two distinct layers referred to as the backing layer and the reaction zone layer.

The numerical model not only predicts SOFC performance at different operating and design conditions but also provides insight on the phenomena occurring within the fuel cell. In an anode-supported SOFC, the ohmic overpotential is the single largest contributor to the cell potential loss. Also, the cathode and electrolyte overpotentials are not negligible even though their thicknesses are negligible relative to the anode thickness. Moreover, methane reforming and water-gas shift reactions aid in significantly reducing the anode concentration overpotential in the thick anode of an anode-supported SOFC. A worthwhile comparison of performance between anode-supported and self-supported SOFCs reveals that anode-supported design of SOFCs is the potential design for operating at reduced temperatures. A parametric study has also been carried out to investigate the effect of various key operating and design parameters on the performance of an anode-supported SOFC. Reducing the operating temperature below 1073 K results in a significant drop in the performance of an anode-supported SOFC; hence ionic conductivity of the ion-conducting particles in the reaction zone layers and electrolyte needs to be enhanced to operate anode-supported SOFCs below 1073 K. Further, increasing the anode reaction zone layer beyond certain thickness has no significant effect on the performance of an anode-supported SOFC. Moreover, there is a spatial limitation to the transport of oxide ions in the reaction zone layer, thereby reflecting the influence of reaction zone thickness on cell performance.

Acknowledgments

I would like to express my profound gratitude to my supervisors, Prof. Xianguo Li and Prof. Ibrahim Dincer, for their support and guidance throughout this thesis. I would also like to thank all my committee members, Prof. Nasser Ashgriz, Prof. Eric Croiset, Prof. Robert Varin, and Prof. Carolyn Ren, for their valuable time in reading this thesis, comments, and constructive criticisms.

I would like to acknowledge Dr. Jeffrey Baschuk, one of my colleagues in our research group, for his endless help throughout his stay at UW. I would also like to acknowledge my other colleagues in the department especially Dr. Waqar Khan, Dr. Shohel Mahmud, and Dr. Muhammad Rashid for their technical and moral support.

Last-but not the least, I would like to thank my parents, my brother and his family, for their prayers and moral support, without their prayers this work would not have been possible.

Dedicated

to

my parents

Contents

List of Tables

List of Figures

List of Symbols

a	Fitting parameter
a_i	Thermodynamic constant
A	Numerical solution constant
A_r	Concentration of the reactant, mole m^{-3}
A_p	Concentration of the product, mole m^{-3}
A_v	Reactive surface area per unit volume, m^{-1}
b	Fitting parameter; width of the channel, m
B	Numerical solution constant
b_i	Thermodynamic constant
$[B]$	Modified Stefan-Maxwell matrix, s m^{-2}
c	Total concentration, mole m^{-3}
c_i	Thermodynamic constant; concentration of species i, mole m^{-3}
c_{pi}	Specific heat of species i at constant pressure, J kg^{-1} K^{-1}
$\bar{c}_{pi}$	Molar specific heat of species i at constant pressure, J $mole^{-1}$ K^{-1}
d_i	Thermodynamic constant
d_p	Pore diameter, μm
D_{ij}	Binary diffusion coefficient, m^2 s^{-1}
$D_{Kn,i}$	Knudsen diffusion coefficient of species i, m^2 s^{-1}
$\mathcal{D}_{ij}$	Combined diffusion coefficient, m^2 s^{-1}
e	Specific energy, J kg^{-1}

E	Cell potential, V
E_r	Reversible cell potential, V
F	Faraday's constant, 96487 C mole^{-1}
$\mathcal{F}_{ix}$	Diffusion flow rate of species i in the x-direction, mole s^{-1}
$\mathcal{F}_{iy}$	Diffusion flow rate of species i in the y-direction, mole s^{-1}
$\mathcal{F}_{iz}$	Diffusion flow rate of species i in the z-direction, mole s^{-1}
$\Delta\bar{g}$	Molar Gibbs function change for a reaction, J mole^{-1}
$\Delta\overline{g}^o$	Molar Gibbs function change for a reaction at standard pressure, J mole^{-1}
h	Heat transfer coefficient, W m^{-2} K^{-1}
h_i	Specific absolute enthalpy of species i, J kg^{-1}
$\overline{h}_i$	Specific molar absolute enthalpy of species i, J mole^{-1}
h_m	Mass transfer coefficient , m s^{-1}
h^o_{fi}	Enthalpy of formation of species i at standard-state condition, J mole^{-1}
$\Delta\bar{h}$	Molar enthalpy change, J mole^{-1}
$\Delta\overline{h}^o$	Molar enthalpy change for a reaction at standard pressure, J mole^{-1}
J	Current density, A m^{-2}
J_{as}	Fitting parameter
J_{avg}	Average current density, A m^{-2}
J_e	Electronic current density, A m^{-2}
J_i	Ionic current density, A m^{-2}
J_{H_2}	Current density produced during hydrogen oxidation, A m^{-2}
$J_o^{H_2}$	Exchange current density for hydrogen oxidation, A m^{-2}
J_{O_2}	Current density produced during oxygen reduction, A m^{-2}
$J_o^{O_2}$	Exchange current density for oxygen reduction, A m^{-2}
J_x	Current density in the x-direction, A m^{-2}
J_y	Current density in the y-direction, A m^{-2}
J_z	Current density in the z-direction, A m^{-2}

k	Reaction rate constant m s^{-1}; thermal conductivity, W m^{-1} K^{-1}
k_{el}	Thermal conductivity of electron-conducting particles, W m^{-1} K^{-1}
k_f	Thermal conductivity of fluid mixture, W m^{-1} K^{-1}
k_i	Thermal conductivity of component i, W m^{-1} K^{-1}
k_{io}	Thermal conductivity of ion-conducting particles, W m^{-1} K^{-1}
k_s	Thermal conductivity of solid phase in the backing layers, W m^{-1} K^{-1}
k_{br}	Backward reaction rate constant for the reforming reaction, mole m^{-3} Pa^{-2} s^{-1}
k_{fr}	Forward reaction rate constant for the reforming reaction, mole m^{-3} Pa^{-2} s^{-1}
k_{bs}	Backward reaction rate constant for the shift reaction, mole m^{-3} Pa^{-2} s^{-1}
k_{fs}	Forward reaction rate constant for the shift reaction, mole m^{-3} Pa^{-2} s^{-1}
K_p	Equilibrium constant for partial pressure
K_{pr}	Equilibrium constant for the reforming reaction
K_{ps}	Equilibrium constant for the shift reaction
Kn	Knudsen number
M_i	Molecular weight of species i, kg $mole^{-1}$
n	Moles of electrons transferred per mole reactant
n_{el}	Number fraction of electron-conducting particles in the reaction zone layers
n_{io}	Number fraction of ion-conducting particles in the reaction zone layers
n_t	Total number of particles in the reaction zone layers per unit volume, m^{-3}
Nu	Nusselt number
N_i	Molar flux of species i, mole m^{-2} s^{-1}
ΔN	Change in number of moles of gaseous species per unit mole fuel
p	Pressure, Pa
p_{el}	Probability of percolation of electron-conducting particles in the reaction zone layers
p_{io}	Probability of percolation of ion-conducting particles in the reaction zone layers
p_i	Partial pressure of species i, Pa
p_0	Standard pressure, Pa

$p^o_{H_2}$	Partial pressure of hydrogen at standard reference state, Pa
$p^o_{H_2O}$	Partial pressure of water vapor at standard reference state, Pa
Q_e	Effective activation energy, J
q_x	Heat flux in the x-direction, W m^{-2}
q_y	Heat flux in the y-direction, W m^{-2}
q_z	Heat flux in the z-direction, W m^{-2}
r_{el}	Radius of electron-conducting particles in the reaction zone layers, m
r_{io}	Radius of ion-conducting particles in the reaction zone layers, m
r_i	Rate of reaction, mole m^{-2} s^{-1}
r_r	Volumetric reforming reaction rate, mole m^{-3} s^{-1}
r_s	Volumetric shift reaction rate, mole m^{-3} s^{-1}
R	Universal gas constant, 8.3143 J $mole^{-1}$ K^{-1}
$\mathcal{R}_a$	Volumetric current density produced due to hydrogen oxidation, A m^{-3}
$\mathcal{R}_c$	Volumetric current density produced due to oxygen reduction, A m^{-3}
R^{ψ}_{es}	Residual of a discretized ψ equation
Sh	Sherwood number
s^o_i	Absolute entropy of species i, J $mole^{-1}$ K^{-1}
$\Delta\bar{s}$	Molar entropy change for a reaction, J $mole^{-1}$ K^{-1}
$\Delta\bar{s}_{H_2}$	Molar entropy change for an overall fuel cell reaction involving hydrogen, J $mole^{-1}$ K^{-1}
$\Delta\bar{s}^o$	Molar entropy change for a reaction at standard pressure, J $mole^{-1}$ K^{-1}
$\dot{S}_c$	Rate of production or consumption of charge, A m^{-3}
$\dot{S}_{e^-}$	Rate of production or consumption of electronic charge, A m^{-3}
$\dot{S}_e$	Energy source term, W m^{-3}
$\dot{S}_{O^{2-}}$	Rate of production or consumption of ionic charge, A m^{-3}
$\dot{S}_{s,i}$	Rate of production or consumption of species i, mole m^{-3} s^{-1} (kg m^{-3} s^{-1})
$\dot{S}_{\psi}$	Numerical source term for a variable
t	Time, s; Thickness, m

T	Temperature, K
T_{op}	Operating temperature, K
T_0	Reference temperature, K
u	Convection velocity in the x-direction, m s^{-1}
U	Total internal energy, J kg^{-1}
u_i	Absolute velocity of species i in the x-direction, m s^{-1}
U_i	Diffusion velocity of species i in the x-direction, m s^{-1}
v	Convection velocity in the y-direction, m s^{-1}
v_m	Mean velocity of the reactant mixture, m s^{-1}
v_i	Absolute velocity of species i in the y-direction, m s^{-1}
V_i	Diffusion velocity of species i in the y-direction, m s^{-1}
w	Convection velocity in the z-direction, m s^{-1}
w_i	Absolute velocity of species i in the z-direction, m s^{-1}
W_i	Diffusion velocity of species i in the z-direction, m s^{-1}
x	Rectangular coordinate, m
x_{H_2}	Mole fraction of hydrogen
x_{H_2O}	Mole fraction of water vapor
x_i	Mole fraction of species i
x_{O_2}	Mole fraction of oxygen
y	Rectangular coordinate, m
y_i	Mass fraction of species i
z	Rectangular coordinate, m
Z	Average coordination number
Z_{el}	Coordination number of electron-conducting particles in the reaction zone layers
Z_{io}	Coordination number of ion-conducting particles in the reaction zone layers

Greek Letters

α	Charge transfer coefficient
γ_{H_2}	Reaction order for hydrogen oxidation reaction
$[\Gamma]$	Inverse of the modified Stefan-Maxwell matrix, $m^2\ s^{-1}$
δ	Distance in finite volume grid, m
ε	Porosity
η_a	Anode overpotential, V
η_c	Cathode overpotential, V
η_{ohm}	Ohmic overpotential, V
θ	Contact angle between electron and ion-conducting particles in the reaction zone layers
κ	Ionic conductivity, S m^{-1}
μ_i	Dynamic viscosity of pure component i, kg $m^{-1}\ s^{-1}$
$\nu_F^{'}$	Number of moles of fuel in the reactant mixture
ν_i	Stoichiometric coefficient of species i involved in the oxidation or reduction reaction
$\nu_i^{'}$	Number of moles of species i in the reactant mixture
$\nu_i^{''}$	Number of moles of species i in the product mixture
λ	Mean free path of the gas molecule, μm
$\Omega_{D,ij}$	Dimensionless function of temperature and intermolecular potential field
ρ	Density, kg m^{-3}
ρ_i	Partial density of species i, kg m^{-3}
ξ	Fraction of entropy change for an overall SOFC reaction
σ	Electronic conductivity, S m^{-1}
σ_{ij}	Collision diameter, ^oA
σ_o	Interface conductivity, S m^{-1}
τ	Tortuosity; Viscous stress, N m^{-2}
ϕ_e	Electronic potential, V
ϕ_i	Ionic potential, V

Φ	Volume fraction of electron-conducting particles in the reaction zone layers
Φ_{ij}	Dimensionless function
ψ	Numerical variable

Miscellaneous

$\forall$	Volume, m^{-3}

Subscripts

act	Activation
an	Anode
abl	Anode backing layer
arl	Anode reaction zone layer
bl	Backing layer
B	Back control volume
b	Back face
ca	Cathode
cbl	Cathode backing layer
con	Concentration
crl	Cathode reaction zone layer
el	Electrolyte
E	East control volume
EB	External boundary condition
e	East face
F	Front control volume
f	Front face

in	Inlet
I	Interface
m	Mean
N	North control volume
n	North face
ohm	Ohmic
ox	Oxidation
P	Control volume center
ref	Reference
rl	Reaction zone layer
s	Surface; South face
S	South control volume
W	West control volume
w	West face

Superscripts

eff	Effective

Acronyms

ANN	Artificial neural network
CFD	Computational fluid dynamics
CV	Control volume
EC	Electrochemical
MTPM	Mean transport pore model
PEM	Polymer electrolyte membrane
RHS	Right hand side

SOFC	Solid oxide fuel cell
SOFCs	Solid oxide fuel cells
TPB	Triple phase boundary
TPBs	Triple phase boundaries
TPBRs	Triple phase boundary regions
YSZ	Yttria stabilized zirconia

Chapter 1

Introduction

Increasing energy demand and diminishing natural resources worldwide due to industrialization and rise in living standards generate the need for efficient use of available energy resources and search for alternative energy conversion technologies. Moreover, the growing environmental concerns such as greenhouse effect, regional acidification and climate change are driving research into cleaner and more efficient ways of producing energy. The features which are required from alternative energy conversion technologies include high energy conversion efficiency, environmental friendliness, compatibility with renewable energy sources and sustainability. One such energy conversion technology which possesses the above characteristics is a device called 'fuel cell'. Fuel cell is an electrochemical device which converts the chemical energy of the reactants directly into electrical energy without an intermediate combustion step. It is considered to be the most important anti-pollution technology in our history [1].

Fuel cells exist in different types, but the two types of fuel cells which received considerable attention from governments, industries and scientific communities are proton exchange membrane or polymer electrolyte membrane (PEM) fuel cell and solid oxide fuel cell (SOFC). PEM fuel cells find application in transportation sector and are considered to have potential to replace internal combustion engines; whereas, solid oxide fuel cells (SOFCs) are mostly applicable in stationary power generation due to their high operating temperature. SOFCs have distinct features from

other fuel cells, which makes them suitable for electric utility power generation in both large central station power plants and distributed or decentralized generation units [2], and the concept of decentralized power grid can be a potential solution to the blackout in North America, few years ago.

SOFCs are all solid state ceramic cells typically operating between 1073 K and 1273 K, thus inhibiting the need of expensive catalysts, such as platinum. Carbon monoxide (CO) is not harmful as in PEM fuel cells, instead can be used as a fuel either directly through electrochemical oxidation or indirectly through water-gas shift reaction. SOFCs reject high quality heat, which can be used for internal reforming, cogeneration or bottoming cycles for additional power generation [3]. Since the electrolyte phase is solid, many of the management issues such as electrode flooding, electrolyte migration and catalyst wetting are not encountered. In addition, cell components of SOFCs can be fabricated into variety of self-supporting shapes and configurations, which might not be feasible with fuel cells employing liquid electrolytes [4].

Among various configurations in which SOFCs exist, the two most common configurations are tubular and planar. Although the tubular configuration of SOFC has achieved significant progress in its development, but possesses high electrical resistance due to longer current paths, resulting in low power density. In contrast to the tubular configuration, the planar configuration of SOFC is simple to manufacture and capable of achieving high power densities due to shorter current paths resulting in low ohmic overpotential [5, 6]. For instance, planar SOFCs are capable of achieving 2 W/cm^2 at 1273 K when compared to 0.25 - 0.3 W/cm^2 for tubular SOFCs [7]. However, due to high temperature operation, there are problems associated with the development and commercialization of planar SOFCs, such as requirement of high temperature gas seals, internal stresses in cell components due to non-uniform temperature distribution and high material and manufacturing costs.

In order to overcome the problems associated with planar SOFCs, much of the efforts are devoted to develop new materials and configurations to improve the performance at reduced operating temperatures, and SOFCs operating between 823 K and 1073 K are referred to as intermediate-

temperature SOFCs [9–13,24]. Intermediate-temperature SOFCs are electrode-supported, in which one of the two electrodes is the thickest component and act as a supporting structure, while the electrolyte is required to have high ionic conductivity and/or small thickness [12]. Anode-supported SOFCs are preferred over cathode-supported, since the latter design is susceptible to significant activation and concentration overpotentials at reduced operating temperatures. By reducing the operating temperature of SOFCs to an intermediate range (823 K and 1073 K), many of the problems associated with planar SOFCs can be resolved. For instance, conventional stainless steel can be used for interconnects instead of more expensive high chrome alloys or oxides resulting in reducing the material and manufacturing costs [12, 14].

The processes influencing the performance in different layers of an SOFC are complex, competing and interdependent. Because of expensive and time consuming physical prototyping, and possibility to explore limited range of design and operating conditions, experimental advances are quite limited. Hence, to enhance the development and understanding of SOFCs, it is imperative to develop a mathematical model which accounts for complex transport processes with chemical and electrochemical reactions. The developed model can be used to predict cell performance and gain insights on the processes occurring in different layers of an SOFC. Thus, the present thesis research develops a mathematical model of planar SOFC incorporating all the relevant physical, chemical and electrochemical processes occurring within the cell. The details of the present thesis research is presented in the later chapters (Chapters 4-6), while the remaining part of this chapter discusses the background of planar SOFC and state the objectives and outline of the present thesis research.

1.1 Background

SOFCs typically operate between 0.5 and 0.7 V, and produce a current density between 0.1 and 0.5 A/cm^2 [15]. The power requirement of an application is satisfied by connecting single cells in series forming a cell stack. Improving the performance of planar SOFC stacks at low operating temperature is the major challenge for the commercialization of an SOFC technology. The performance of the stack depends on the performance of individual cells in the stack. Therefore, the present thesis

research focuses on the modeling of a single planar SOFC.

Planar SOFCs are generally manufactured in three basic designs, namely electrolyte-supported, cathode-supported, and anode-supported. In electrolyte-supported cells, anode and cathode layers are deposited on a thicker electrolyte ($\geq$150 μm), and such cells are suitable for operation around 1273 K [9]. Due to the thickness of the electrolyte, the ohmic overpotential of the electrolyte is significant in these cells. Whereas, in electrode-supported (anode or cathode) cell designs, the ohmic contribution of the electrolyte is smaller than electrolyte-supported SOFCs due to very thin electrolytes (20 μm), and are preferred for low temperature operation between 823-1073 K [17]. However, in electrode-supported SOFCs, concentration overpotential due to resistance to the transport of reactants to the reaction sites becomes significant at high utilization. Therefore, the thicknesses of different components of the cell should be optimized to have a self-supported design of SOFC which minimizes both ohmic and concentration overpotentials and provides better performance.

Figure 1.1 illustrates different layers of an SOFC. A typical SOFC consists of three major layers such as anode electrode (backing) layer, electrolyte layer and cathode electrode (backing) layer. Two additional layers which are shown in Figure 1.1 between the electrode (backing) and electrolyte layers are referred to as the anode reaction zone layer and the cathode reaction zone layer. The reaction zone layers on either side of the electrolyte layer are considered to be distinct layers because of the fact that the electrochemical reactions not only occur on the interface between the anode and the electrolyte, and the cathode and the electrolyte, but also extend to a depth of 10-50 μm inside the electrode (backing) layers [18–23].

Typically, the electrolyte of an SOFC is made from Zirconia doped with 8-10% yttria (YSZ). The ionic conductivity of YSZ is 0.02 S/cm at 1073 K and 0.1 at 1273 K [16]. The current state-of-the-art electrolyte material exhibiting excellent ionic conductivity ($\geq$ 0.1 S/cm) at 1073 K is LaSrGaMgO (LSGM), and is considered to be a potential candidate to replace YSZ in a SOFC operating at 1073 K [11, 24, 25]. However, there are still stability issues to be addressed in the reducing and oxidizing environments before LSGM could replace the typical YSZ.

The anode of a typical SOFC is a cermet made of nickel and YSZ. Zirconia provides thermal

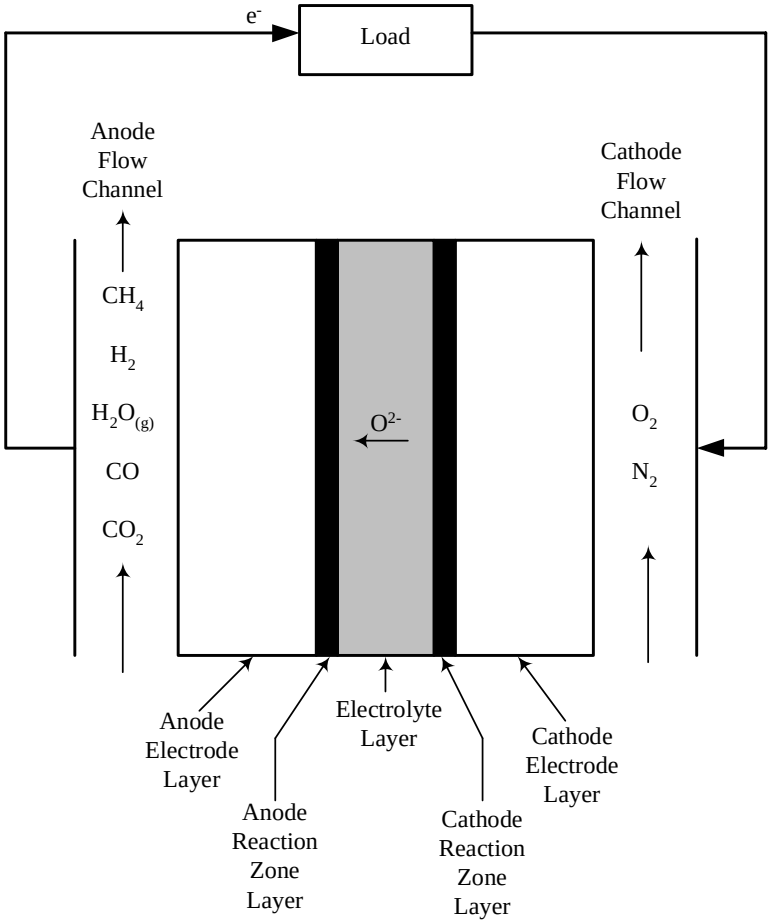

Figure 1.1: Illustration of different layers of an SOFC.

expansion coefficient equivalent to that of the typical electrolyte and inhibits sintering of metallic nickel particles. On the other hand, cathode is made of strontium doped lanthanum manganite in a typical SOFC. The current state-of-the-art anode and cathode materials are Ni-samaria-doped ceria cermet and lanthanum strontium ferrite (lanthanum strontium cobaltite), respectively [16,24].

The chemical energy stored in the reactants is converted into electrical energy, heat, and water vapor and/or carbon dioxide (CO_2) in the reaction zone layers. The reaction zone layers are mixture of ion-conducting particles, electron-conducting particles and void space occupied by reactant gases, often referred to as triple phase boundary regions (TPBRs). The overall half-cell reaction in the anode reaction zone layer is:

$$H_2 + O^{2-} \rightarrow H_2O_{(g)} + 2e^- \tag{1.1}$$

and/or

$$CO + O^{2-} \rightarrow CO_2 + 2e^- \tag{1.2}$$

In the cathode reaction zone layer, oxygen combines with electrons to produce oxide ions

$$\frac{1}{2}O_2 + 2e^- \rightarrow O^{2-} \tag{1.3}$$

The combination of half-cell reactions given in Equations (1.1) and (1.3), and (1.2) and (1.3) are the overall SOFC reactions:

$$H_2 + \frac{1}{2}O_2 \rightarrow H_2O_{(g)} + \text{Heat} + \text{Electrical Energy} \tag{1.4}$$

$$CO + \frac{1}{2}O_2 \rightarrow CO_2 + \text{Heat} + \text{Electrical Energy} \tag{1.5}$$

The gas stream on the anode side of an SOFC is a multi-component mixture, which include hydrogen (H_2), water vapor (H_2O), carbon monoxide (CO), and carbon dioxide (CO_2). In addition, methane (CH_4) could also be present, if internal reforming of methane is considered within the cell. CO acts as a fuel either directly through electrochemical reaction given in Equation (1.2) or indirectly through water-gas shift reaction converting to hydrogen and carbon dioxide, which is given as:

$$CO + H_2O \rightleftharpoons CO_2 + H_2 \tag{1.6}$$

On the cathode side, oxygen (O_2) is the main reactant with nitrogen (N_2) being present if air is used as oxidant.

The transport processes occurring inside different layers of SOFCs are summarized in Table 1.1. The phenomena generally occurring within the backing layers are (i) transport of multi-component mixture to and from the reaction sites in the reaction zone layers, (ii) transport of electrons in the solid portion of the porous backing layers, and (iii) transport of energy due to heat conduction and species diffusion. In addition, species are produced and consumed due to chemical reactions in the anode backing layer, which also result in heat generation/consumption. Moreover, electron

transport also generates heat within the backing layers due to Joule heating effect. The phenomena occurring in the reaction zone layers are similar to the backing layers. Additionally, due to ion-conducting particles in the reaction zone layers, transport of ions in the ion-conducting particles takes place in the reaction zone layers. Further, species are produced and consumed due to electrochemical oxidation and reduction reactions in the anode and cathode reaction zone layers, respectively. Since electrochemical reactions are exothermic reactions, heat is produced in the reaction zone layers in addition to Joule heating due to electron and ion migration in the electron and ion-conducting particles of the reaction zone layers. Unlike the backing and reaction zone layers, the electrolyte layer is fully dense with no interconnected porosity and acts as an insulator for the electrons. The phenomena occurring in the electrolyte layer are transport of oxide ions and transport of energy due to heat conduction. The ion transport in the electrolyte layer generates heat through Joule heating.

Table 1.1: Transport processes in each layer of an SOFC.

Layer	Processes
Anode/cathode electrode (backing) layer	Multi-component species transport Electron transport Energy transport
Anode/cathode reaction zone layer	Multi-component species transport Electron transport in electron-conducting particles Ion transport in ion-conducting particles Energy transport
Electrolyte layer	Ion transport Energy transport

In general, cell potential of any cell can be obtained by deducting the overpotentials from the reversible cell potential

$$E = E_r - \eta_{\text{act}} - \eta_{\text{ohm}} - \eta_{\text{con}} \tag{1.7}$$

where E_r represents the reversible cell potential of a fuel cell obtained at thermodynamically reversible condition, also called the maximum theoretical electric potential for a given fuel cell reaction. Under typical operating conditions of an SOFC, such as 1273 K and 1 atm, the reversible

cell potential is approximately 0.9 V when hydrogen is used as a fuel. The overpotentials such as activation (η_{act}), ohmic (η_{ohm}) and concentration (η_{con}) arise from irreversibilities within the SOFC due to resistance to the electrochemical reactions, resistance to the transport of electrons through the electron-conducting particles and oxide ions through the ion-conducting particles and resistance to the transport of reactant species to the reaction sites in the reaction zone layers, respectively.

Due to the adverse effects of high temperature operation of SOFCs such as non-homogenous temperature distribution inside the cell, mismatch in thermal expansion coefficient among cell components, corrosion of cell components, much attention is being focused on reducing the operating temperature through various designs and materials. Therefore, the present thesis research developed a mathematical model of planar SOFC, which can predict the performance both at high and intermediate operating temperatures. In order to simulate the performance of an SOFC, electrochemical reactions in the reaction zone layers, electron migration in the solid matrix of the backing layers and electron-conducting particles in the reaction zone layers, oxide ion transport through the electrolyte and ion-conducting particles of the reaction zone layers, and mass transport of the reactants and products in the backing as well as reaction zone layers must be included in the mathematical model.

1.2 Thesis Objectives and Outline

The processes occurring within each layer of the cell affects the performance of an SOFC. Because of high operating temperature and thinness of the layers in an SOFC, extensive experimental measurements within the cell layers are quite difficult. Thus, mathematical modeling and simulation has become the valuable tool for better understanding and optimization of SOFCs. Therefore, the objectives of this thesis are to

- verify modeling an electrode as two distinct layers.
- develop a mathematical model of planar SOFC satisfying the following requirements:
  - flexibility in fuel choice: not only pure hydrogen (H_2) but also any reformate composition

composed of multi-component mixture such as methane (CH_4), hydrogen (H_2), water vapor ($H_2O_{(g)}$), carbon monoxide (CO), and carbon dioxide (CO_2) can be used as a fuel.

  - reaction zone layers as finite volumes: electrochemical reactions not only occur at the interfaces between the electrodes and the electrolyte but also extend to a depth of 10-50 μm inside the electrodes; therefore, reaction zone layers are treated as finite volumes rather than mathematical surfaces (boundary conditions).
  - chemical reactions in the anode: methane reforming and water-gas shift reactions are possible in the anode.
  - Knudsen diffusion in the porous layers: both ordinary and Knudsen diffusion in the porous layers of an SOFC are of comparable magnitude and therefore Knudsen diffusion has to be considered in addition to ordinary diffusion.
  - versatility of the physical domain: able to simulate self-supported (high-temperature) as well as anode-supported (intermediate-temperature) designs of SOFCs.

- develop the numerical solution of the mathematical model using finite volume method and the computer language of C++,
- provide numerical results simulating the performance of anode-supported (intermediate-temperature) and self-supported (high-temperature) SOFCs, and
- examine the effect of key operating and design parameters on the performance of anode-supported (intermediate-temperature) and self-supported (high-temperature) SOFCs.

Based on the verification of modeling an electrode in an SOFC, the mathematical model treats the electrode as two distinct layers, referred to as the backing layer and the reaction zone layer. Transport phenomena in these layers are governed by conservation equations. Reaction zone layers are regions where reaction sites are active and most of the electrochemical reactions occur within a distance of the order of 10 μm from the electrode/electrolyte interfaces in the electrodes. Often, reaction zone layers are treated as mathematical surfaces or boundary conditions in the existing

models. Treating the reactions zone layers as boundary conditions simplifies the model significantly, and thereby loses the insights on the physical, chemical and electrochemical processes occurring in these thin layers. Further, most of the existing models in the open literature are valid for binary mixtures, thus neglecting one of the important characteristics of SOFCs in terms of flexibility in fuel choice. Therefore, in the present mathematical model, reaction zone layers are treated as finite volumes, and conservation equations together with the constitutive equations such as the modified Stefan-Maxwell equations incorporating Knudsen diffusion for multi-component diffusion are solved in the backing as well as the reaction zone layers, and it is a unique contribution of this thesis research to the field, which has been published as Hussain et al. [26, 27].

A brief outline of the present thesis is as follows. SOFC models published in the open literature are reviewed in Chapter 2. Chapter 3 presents the formulation and calculation of reversible cell potential (E_r) at different operating conditions. Model formulation of backing layers, reaction zone layers, and electrolyte layer are presented in Chapter 4 along with boundary conditions. Numerical implementation of the present mathematical model is documented in Chapter 5. Validation of the present model, verification of modeling an electrode as two distinct layers, and the results obtained from numerical simulation of anode-supported and self-supported SOFCs are presented in Chapter 6. Lastly, some key conclusions and recommendations for future work are outlined in Chapter 7.

Chapter 2

Literature Review

High energy conversion efficiency, low emissions, and flexibility in fuel choice have initiated the research and development of solid oxide fuel cells (SOFCs) for applications in centralized as well as decentralized power generation units. Over the past few years, many research studies have been undertaken with the goal of improving the performance of an SOFC and its characteristics at reduced operating temperature. Mathematical modeling is an important tool in the research and development of any technology, as it helps in reducing the need of repetitive and costly experimentation. Modeling efforts on SOFCs may serve two purposes. Firstly, it helps in predicting the performance of an SOFC, which means predicting the polarization or cell potential versus current density curve. Secondly, it provides insight on the electrochemical processes and transport phenomena occurring within the fuel cell.

Numerous modeling studies on SOFCs exist in the published literature and can generally be classified into electrode and cell/stack models. Electrode models aim at developing better electrodes through detailed studies of the processes occurring within the electrodes and involve investigation of structural parameters influencing the performance of electrodes. On the other hand, cell models are developed with the goal of optimizing the performance based on operating and design parameters, and involves parametric studies [28]. In this chapter, electrode and cell models of SOFCs published in the open literature are reviewed.

2.1 Electrode Models

Electrode models in SOFCs can be categorized into micro or macro models depending on the treatment of electrodes. In the micro modeling studies, electrodes are treated as porous structures of electron- and ion-conducting particles. Essentially, electrodes in micro models are treated as reaction zone layers having triple phase boundaries (TPBs) scattered throughout the electrodes. In contrast to the micro models, electrodes in macro models are treated as porous structures of pure electron-conducting particles and electrochemical reactions are considered to occur exclusively at the electrode/electrolyte interfaces, thereby treating the reaction zone layers as boundary conditions.

One of the earlier models classified under "micro models" was developed by Costamagna *et al.* [29]. They developed a one-dimensional model which takes into account the electron and ion transport through electron- and ion-conducting particles of the electrode and considered mass transport of species through the pores to be negligible. In other words, they assumed uniform concentration of species throughout the electrode, which is not true. Since the reactant is consumed at the reaction sites, the assumption of uniform concentration of species throughout the electrode is not valid. Later Chan and Xia [30] developed a model which considers mass transport through the anode. Their model was also one-dimensional with hydrogen as the only anodic reactant. Moreover, the exchange current density in the Butler-Volmer equation was assumed to be constant, which instead is a strong function of temperature and concentration of reactant in the electrode [3]. Then, Xia *et al.* [31] improved the model developed previously by Chan and Xia [30], and considered the exchange current density as a function of reactant and product concentration, expressed as

$$J_o = nFk(A_r)^{(1-\alpha)}(A_p)^{(\alpha)} \tag{2.1}$$

where n is the number of electrons transferred per mole of fuel consumed, F is the Faraday's constant, k is the reaction rate constant, A_r is the concentration of reactant, A_p is the concentration of product, and α is the charge transfer coefficient.

Recently, Chen *et al.* [32] and Deseure *et al.* [33] have applied micro modeling approach to an SOFC cathode. Their models were also one dimensional and isothermal. The model of Deseure *et al.* [33] accounts for activation and mass transport processes only; however, all forms of overpotentials contribute to the total electrode overpotential. Hence, a model must predict activation, ohmic and concentration overpotentials of an electrode to determine the true contribution of an electrode to the total cell potential loss.

In the macro modeling studies of electrodes, Yakabe *et al.* [14], Lehnert *et al.* [18], and Suwanwarangkul *et al.* [34] developed models describing the transport of gaseous species inside the porous anode. Yakabe *et al.* [14] and Lehnert *et al.* [18] used the dusty-gas model to model the mass transport through the porous anode; whereas, Suwanwarangkul *et al.* [34] used three different models, namely Fick's model, dusty-gas model and Stefan-Maxwell model, to simulate two binary (H_2-H_2O and CO-CO_2) and a ternary system (H_2-H_2O-Ar) inside the porous anode. The similarity in their models [14, 18, 34] was the consideration of the reaction zone layer as a boundary condition, consistent with the macro modeling approach of treating electrodes. However, it is widely reported in the open literature that the electrochemical reaction not only occurs on the electrode/electrolyte interface but also extends to a distance of 10-50 μm from the electrolyte [18–23, 36]. Moreover, the models of Yakabe *et al.* [14], Lehnert *et al.* [18], and Suwanwarangkul *et al.* [34] can only predict the concentration overpotential in the anode. However, as stated before, all forms of overpotentials (activation, ohmic, and concentration) in the electrodes contribute to the total cell potential loss.

More recently, Hussain *et al.* [26] have developed a mathematical model describing the transport of multi-component mixture inside the anode of an SOFC. The novelty of the model is its treatment of the electrode. An electrode is treated as two distinct layers referred to as the backing layer and the reaction zone layer, thus serving as a bridge connecting the micro and macro approaches of modeling electrodes. Moreover, the model is fuel flexible and uses the modified Stefan-Maxwell model incorporating Knudsen diffusion to model multi-component diffusion in the porous electrodes. Further, the model can predict all forms of overpotentials in the electrode, thus determining the true contribution of an electrode to the cell potential loss [35].

2.2 Cell Models

Electrode micro models are effective in determining the performance of electrodes with respect to structural parameters; whereas, electrode macro models are effective in determining the rate of mass transport through the porous electrodes, and neither of them represent the performance of a complete cell. The performance of a complete cell is influenced by the transport of multi-component mixture within the electrodes, transport of oxide ions from the cathode reaction zone layer to the anode reaction zone layer through the electrolyte layer, transport of electrons through the electron-conducting particles of the backing and and reaction zone layers and electrochemical reactions in the anode and cathode reaction zone layers.

Similar to the electrode models, cell models on SOFCs can also be categorized into micro and macro cell models depending upon the treatment of electrodes. However, most of the researchers used the macro modeling approach to model electrodes in their cell models; only recently Nam and Jeon [36] used the micro modeling approach to model electrodes in their cell model for an intermediate-temperature SOFC. They developed a 1-D isothermal model with binary mixture in the anode, thereby neglected the fuel flexibility characteristic of SOFCs. Moreover, the thickness of the electrodes were limited to 50 μm.

One of the earliest complete cell models of SOFCs was developed by Ferguson *et al.* [37]. The model includes electrode layers, electrolyte layer, fuel and air channels, and interconnects. Only conservation of species was applied to the gases in the fuel and air channels, assuming to have no pressure drop in the direction of main flow. Electrochemical reactions were assumed to occur at the interfaces of electrodes and electrolyte. Further, in the porous electrodes, Fick's law of diffusion was used to account for multi-component diffusion, which according to Krishna and Wesselingh [38] is strictly valid for binary or dilute mixtures.

Later, Kim *et al.* [9] developed an empirical model for an anode-supported SOFC operating between 923 K and 1073 K. They performed a simple one-dimensional analysis based on binary diffusion for estimating concentration polarization and considered activation polarization in the Tafel limit, which is only valid for small exchange current densities (J_0) or large activation overpotential.

The equation describing the performance is given as

$$E(J) = E_r - JR_J - a - bln[J] + \frac{RT}{4F}ln\left[1 - \frac{J}{J_{cs}}\right] + \frac{RT}{2F}ln\left[1 - \frac{J}{J_{as}}\right] - \frac{RT}{2F}ln\left[1 + \frac{p^o_{H_2}J}{p^o_{H_2O}J_{as}}\right] \quad (2.2)$$

where E_r is the reversible cell potential, J is the cell current density, and R_J, J_{as}, J_{cs}, a and b are fitting parameters.

Chan *et al.* [39] developed a 1-D polarization model of an SOFC. Only two species were considered in the electrodes and used Fick's law of diffusion to model the diffusion flux. The temperature was assumed to be uniform throughout the cell components. Moreover, the exchange current density (J_o), which is a strong function of temperature and concentration of the reactants, was considered as constant. Then, Nagata *et al.* [40] also developed a 1-D model to compute temperature and concentration distributions in a tubular SOFC. Ohmic polarization due to resistance to the transport of electrons in the electrodes was neglected. Further, the Knudsen diffusion was neglected in the porous electrodes. However, the exchange current density (J_o) was considered as a function of temperature, which is given as

$$J_o = \frac{\sigma_o RT}{(2+\alpha)F} \quad (2.3)$$

where β is the charge transfer coefficient, R is the universal gas constant, σ_o is the interface conductivity and F is the Faraday's constant.

Later, Chan *et al.* [41] also developed an SOFC model for tubular design fed with natural gas. Only the thermodynamic aspect and electrochemical processes of the cell operation were considered. However, the exchange current density (J_o) was considered as a function of temperature, unlike their previous study [39], but did not provide the functional relationship between the exchange current density and temperature.

Artificial neural network (ANN) was also used to predict the performance of an SOFC by Arriagada *et al.* [42]. In order to predict the performance of an SOFC, ANN was trained with some data generated from a validated cell model. The applicability of ANN in predicting the performance of an SOFC was showed and claimed that ANN would predict the performance in less time and

good accuracy.

A 3-D mathematical model for a planar SOFC was developed by Yakabe *et al.* [43]. Thermo-fluid calculations were performed using the commercial CFD package "STAR-CD", and used "ABAQUS" to determine thermal stress distributions in the electrolyte and interconnects. The details of coupling between the thermo-fluid model and their electrochemical model were not provided. Later, Recknagle *et al.* [5] also developed a 3-D model for a planar SOFC. They also used the commercial CFD package "STAR-CD" to perform thermo-fluid calculations. Further, the electrochemical model which was used to link between thermo-fluid and electrochemical calculations contains several adjustable parameters, which were obtained from a small single cell (1 in. diameter) operating at different fuel compositions and temperatures.

Petruzzi *et al.* [44] developed a thermo-electrochemical model for an SOFC system. The major drawbacks of their study were the consideration of concentration polarization to be negligible and use of Tafel equation to model activation polarization.

A mathematical model representing electrolyte-electrode-assembly of an anode-supported planar SOFC was developed by Zhu and Kee [46]. The temperature was considered to be uniform throughout the electrolyte-electrode-assembly and electrochemical reactions were assumed to occur at the interfaces between the electrodes and electrolyte. However, they believed that electrochemical reactions could occur in the vicinity of electrolyte/electrode interfaces and the depth of reaction zone layers could extend upto 50 μm, as reported by Lehnert *et al.* [18] and Williford and Chick [19].

Pasaogullari and Wang [17] developed a CFD model of planar SOFC, using the commercial CFD software FLUENT. The model assumes ohmic polarization in the electron-conducting particles of porous electrodes to be negligible and electrochemical kinetics of the electrodes were approximated by Tafel kinetics, which is applicable for high activation polarization. Moreover, only binary species were considered in their model.

Beale *et al.* [28] also developed a numerical model for performance prediction of a planar SOFC. They also used commercial packages such as PHOENICS and FLUENT to solve the governing equations supplemented with a code for electrochemical reactions. Electrochemical reactions were

assumed to occur at the interfaces between the electrodes and electrolyte. They also solved species transport equation for binary species. Further, ohmic polarization was estimated through an empirical model developed by Dong *et al.* [47].

A 2-D mathematical model describing the mass and heat transport in porous electrodes of a planar SOFC was developed by Ackmann *et al.* [48]. The Mean transport pore model (MTPM) was used to model the transport of gases in the porous electrodes. The current densities were calculated using the linear current-potential relation, which is valid for activation polarization less than 0.1 V [39].

The effect of radiation heat transfer in an SOFC was studied by VanderSteen and Pharoah [49, 50]. A commercial CFD code was used to perform the calculations. The calculations were performed at a constant current density of 0.8 A/cm^2, which is higher than the typical operating current density of 0.5 A/cm^2 [15]. They claimed that neglecting radiation would result in over predicting the temperature by 30 K. This seems to be an over optimistic conclusion. Radiation heat transfer is considered to be negligible in almost all of the modeling studies on SOFC due to two reasons. First, the aspect ratios (length-to-height) of flow channels are extremely large, approximately 100:1 on the cathode side and 200:1 on the anode side, which makes the view factors too small enough to neglect the effect of radiation heat transfer [5]. Second, it is computationally expensive; the time required to perform calculations when radiation heat transfer is considered is ten times higher than without considering the radiation heat transfer [43]. Recently, Damm and Fedorov [51] and Daun *et al.* [52] also found from their study that the radiation heat transfer has a negligible effect on the temperature field, and Daun *et al.* [52] concluded that the radiation heat transfer does not need to be accommodated in comprehensive thermal models of planar SOFCs.

Khaleel *et al.* [6] developed an electrochemical (EC) module for modeling a planar SOFC. The EC module was coupled to a commercial finite element analysis code, MARC. Flow and thermal calculations were performed by MARC based on the given initial and boundary conditions, and the heat generation was calculated by the EC module. The current-potential relation used in the EC module was the empirical model developed by Kim *et al.* [9]. Further, the effect of Knudsen

diffusion was neglected in their model. Furthermore, the ohmic resistance in the electrolyte was calculated using the following relation:

$$\eta_{ohm} = t_e c_e T exp\left(\frac{Q_e}{T}\right) \tag{2.4}$$

where t_e is the thickness of the electrolyte and Q_e is the effective activation energy.

In the last few years, many researchers have developed models on anode-supported SOFCs. Aguiar *et al.* [12] developed a 1-D model of a planar anode-supported SOFC. The model is based on the assumption that the principal gaseous species are H_2 and H_2O in the anode, and O_2 and N_2 in the cathode. Further, it has been assumed that the electrochemical reactions occur only at the electrode/electrolyte interfaces. Moreover, the equations used to obtained the concentration of reactants and products at the reaction sites are similar to the relations developed by Kim *et al.* [9]. Later Yuan and Sunden [53] performed a numerical investigation of the transport processes in a planar anode-supported SOFC. The physical domain includes the porous layer, gas flow duct, and solid interconnects. They also treated reaction zone layers as boundary conditions. Further, only binary fuel mixture (H_2+H_2O) was considered on the anode side. Although in their recent work, Yuan and Sunden [54] have considered multi-component mixture in the anode, yet treated the reaction zone layer as boundary condition.

Recently, Suwanwarangkul *et al.* [55] developed a 2-D isothermal model of an SOFC for button cell geometry operating on syngas. Operating temperature was limited to 1073 K and 1173 K. Mass transport and ohmic resistances within the electrodes were neglected, implying electrode subdomains were neglected in their model. Moreover, electrochemical reactions and the water-gas shift reaction were considered to occur exclusively at the electrode/electrolyte interfaces. However, they acknowledged that electrochemical reactions in an SOFC take place at TPBs in the vicinity of electrode/electrolyte interface.

More recently, Hussain *et al.* [27] have developed a mathematical model predicting the performance of a planar SOFC. One of the novel features of the model is the consideration of reaction zone layers as finite volumes. The other important characteristic of the model is the flexibility

of fuel choice, not only pure H_2 but also any reformate composition can be used as a fuel. The modified Stefan-Maxwell model incorporating Knudsen diffusion is used to model multi-component mass transport inside the porous layers. Moreover, the general Butler-Volmer equation is used to model the electrochemical reactions in the reaction zone layers.

2.3 Summary

SOFC models can be classified into electrode or cell models. Depending upon the approach used to model the electrodes, electrode models can further be categorized into micro or macro models. Similar to the electrode models, cell models can also be classified into micro or macro models; however, micro models are electrode-level models predicting the electrochemical characteristics of an electrode, either anode or cathode; only recently Nam and Jeon [36] integrated this approach into a cell-level model.

In micro models, electrodes are modeled as porous structures of electron- and ion-conducting particles. Essentially, electrodes in micro models are treated as reaction zone layers having TPBs scattered throughout the electrodes. However, it is widely reported in the open literature that the TPBs are most active at the electrode/electrolyte interface and most of the electrochemical reactions in the electrodes occur within a distance of the order of 10 μm from the electrolyte. On the other hand, in macro models, electrodes are modeled as porous structures of electron-conducting particles and electrochemical reactions are considered to occur exclusively at the electrode/electrolyte interfaces, thereby treating the reaction zone layers as boundary conditions. However, incorporation of micro characteristics of the electrodes into macro models not only helps in better understanding of the processes occurring within the electrodes but also enhances the predicting capability of the overall cell model.

Therefore, the objectives of this thesis research is to verify and treat an electrode as two distinct layers referred to as the backing layer and the reaction zone layer, thus serving as a bridge connecting the micro and macro approaches of modeling electrodes. Although many researchers [9,14,18,19,34, 46, 48] have indicated a region in the vicinity of an electrode/electrolyte interface, often referred to

as a "reaction zone", where most of the electrochemical reaction occurs, but no one has attempted to model this region as a finite volume, rather assumed to be a boundary condition. One of the reasons to consider this region as a boundary condition is because of its thickness (10-50 μm) relative to the thickness of the backing layer. In addition, conservation equations are not required to be solved in this thin layer if it is assumed as a boundary condition. However, many of the physical, chemical and electrochemical processes would have to be neglected while considering the reaction zone layer as a boundary condition. The other important objective of this thesis research is to develop a model which is fuel flexible, satisfying one of the main driving forces for SOFC research and development. By fuel flexible, we mean the model should able to predict the performance and other characteristics for not only pure H_2 as a fuel but also any reformate composed of H_2, H_2O, CO, CO_2 and CH_4. In order to develop a model which is fuel flexible, we need to consider multi-component mixture transport in the backing and reaction zone layers. Stefan-Maxwell model or dusty gas model has to be used to describe multi-component diffusion rather than Fick's law of diffusion. Moreover, the effect of Knudsen diffusion has to be considered in addition to ordinary diffusion in the porous layers as ordinary and Knudsen diffusion are of comparable magnitude in the porous layers of an SOFC [39, 46]. The modified Stefan-Maxwell model incorporating Knudsen diffusion is used to describe multi-component diffusion in the present thesis research. In addition, due to the presence to multi-component mixture, chemical reactions such as the water-gas shift and methane reforming are possible in the anode; therefore, the developed model considers chemical reactions as well. Finally, the important features or characteristics of the present SOFC model are outlined as follows.

- Fuel flexibility: Able to simulate not only pure hydrogen (H_2) but also any reformate composition composed of multi-component mixture such as methane (CH_4), hydrogen (H_2), water vapor ($H_2O_{(g)}$), carbon monoxide (CO), and carbon dioxide (CO_2).

- Reaction zone layers: The conservation equations are applied to the regions in the vicinity of the electrodes and the electrolyte to model various transport processes along with chemical and electrochemical reactions.

- Chemical reactions: Methane reforming and water-gas shift reactions are considered in the anode.
- Knudsen diffusion: Both ordinary and Knudsen diffusion are included in the model.
- Multi-dimensional: The model is three-dimensional.
- Versatile physical domain: The model can simulate anode-supported and self-supported SOFC designs suitable for operation at high- and intermediate-temperatures.

Chapter 3

Reversible Cell Potential

This chapter presents the formulation and calculation of reversible cell potential as a function of operating conditions. The potential of a fuel cell at thermodynamic reversible condition is called reversible cell potential, which is the maximum theoretical electric potential for a given fuel cell reaction. This potential can be determined based on the thermodynamic analysis and is related to the change in Gibbs function between the products and the reactants for a given fuel cell reaction. Since the change in Gibbs function depends on temperature, pressure and concentration of the reactants, so does the reversible cell potential. For a given fuel cell reaction, the change in Gibbs function ($\Delta\overline{g}$) is related to the reversible cell potential (E_r) as follows:

$$E_r = -\frac{\Delta\overline{g}}{nF} \tag{3.1}$$

where n is the number of moles of electrons transferred per mole of fuel consumed and F is the Faraday's constant.

3.1 Thermodynamic Formulation

For the calculation of reversible cell potential, an overall fuel cell reaction involving N species can be expressed in the following general form [3]:

$$\sum_{i=1}^{N} \nu_i^{'} M_i \Rightarrow \sum_{i=1}^{N} \nu_i^{''} M_i \tag{3.2}$$

where M_i is the chemical formula for species i; $\nu_i^{'}$ and $\nu_i^{''}$ are the number of moles of species i in the reactant and product mixture, respectively.

The change in Gibbs function per unit mole of fuel can be written as

$$\Delta\overline{g} = \Delta\overline{h} - T\Delta\overline{s} \tag{3.3}$$

where $\Delta\overline{h}$ is the enthalpy change per unit mole of fuel, and $\Delta\overline{s}$ is the entropy change per mole of fuel for an overall fuel cell reaction.

Assuming the gaseous reactants and products as ideal gases, the reversible cell potential as a function of temperature, pressure and concentration of the reactants, can be expressed in the general form of Nernst equation as

$$E_r\left(T, p, p_i\right) = -\frac{\Delta\overline{g}^o\left(T\right)}{nF} - \frac{\Delta N RT}{nF}\ln\left(\frac{p}{p_0}\right) - \frac{RT}{nF}\ln K_p \tag{3.4}$$

where $\Delta\overline{g}^o\left(T\right)$ is the molar Gibbs function change for fuel, oxidant and exhaust streams at reference pressure p_0. Usually, T_0 is taken as 298 K, and p_0 as 1 atm, and these conditions are often referred to as the standard temperature and pressure. ΔN represents the change in number of moles of gaseous species per unit mole of fuel during the reaction, and K_p is called equilibrium constant for partial pressure defined as

$$K_p = \prod_{i=1}^{N}\left(\frac{p_i}{p}\right)^{\left(\frac{\nu_i^{''} - \nu_i^{'}}{\nu_F^{'}}\right)} \tag{3.5}$$

In terms of mole fractions, K_p can be written as

$$K_p = \prod_{i=1}^{N} (x_i)^{\left(\frac{\nu_i'' - \nu_i'}{\nu_F'}\right)} \tag{3.6}$$

The Nernst potential given in Equation (3.4) for an overall H_2-O_2 fuel cell reaction

$$H_2\,(g) + \frac{1}{2} O_2\,(g) \rightleftharpoons H_2O\,(g) \tag{3.7}$$

reduces to

$$E_r\,(T, p, x_i) = -\frac{\Delta \overline{g}^o\,(T)}{nF} - \frac{RT}{2nF} \ln\left(\frac{p_0}{p}\right) - \frac{RT}{nF} \ln\left(\frac{x_{H_2O}}{x_{H_2} x_{O_2}^{\frac{1}{2}}}\right) \tag{3.8}$$

where the first term on the right-hand side of the above equation shows the effect of temperature on the reversible cell potential, while the second and third terms show the effect of pressure and concentration of the reactants on the reversible cell potential, respectively.

It can be seen from Equation (3.3) that the change in Gibbs function as a function of temperature, $\Delta \overline{g}^o\,(T)$, requires that the enthalpy and entropy changes to be determined. The enthalpy and entropy changes for an overall fuel cell reaction can be obtained as

$$\Delta \overline{h}^o\,(T) = \sum_{i=1}^{N} \left(\nu_i'' - \nu_i'\right) \left(h_{fi}^o + \int_{T_0}^{T} \overline{c}_{pi} dT\right) \tag{3.9}$$

$$\Delta \overline{s}^o\,(T) = \sum_{i=1}^{N} \left(\nu_i'' - \nu_i'\right) \left(s_i^o + \int_{T_0}^{T} \frac{\overline{c}_{pi}}{T} dT\right) \tag{3.10}$$

where ν_i' and ν_i'' are the number of moles of species i in the reactant and product mixture, respectively, h_{fi}^o is the enthalpy of formation of species i, s_i^o is the absolute entropy of species i, and the values of these properties are given in Table 3.1, and $\overline{c}_{pi}$ is the specific heat at constant pressure, which is approximated as follows:

$$\overline{c}_{pi} = a_i + b_i T + c_i T^2 + d_i T^3 \tag{3.11}$$

where the coefficients a_i, b_i, c_i, and d_i are given in Table 3.2.

Table 3.1: Thermodynamic properties.

Species	h^o_{fi} (J mole^{-1})	s^o_i (J mole^{-1} K^{-1})
H_2	0	130.68
O_2	0	205.14
H_2O (g)	-2418260	188.83

Source: Cengel and Boles [96].

Table 3.2: Heat capacity constants.

Species	a_i	$b_i \times 10^{-2}$	$c_i \times 10^{-5}$	$d_i \times 10^{-9}$	T range, K
H_2	29.11	-0.1916	0.4003	-0.8704	273-1800
O_2	25.48	1.520	-0.7155	1.312	273-1800
H_2O (g)	32.24	0.1923	1.055	-3.595	273-1800

Source: Cengel and Boles [96].

The Gibbs function change for an overall reaction at temperature T and pressure p_0 can be calculated using Equation (3.3). Then, Equation (3.8) can be used to determine the reversible cell potential for a given set of operating conditions (temperature, pressure and concentration of the reactants).

3.2 Reversible Potential

Typically, SOFCs operate in the temperature range of 1073 K and 1273 K. The water produced is in the vapor phase for the SOFC reaction given in Equation (3.7). Using the equations presented in the above section, the reversible cell potential (E_r), as a function of temperature, pressure and concentration of the reactants is calculated, and the results obtained are shown in Figures 3.1-3.4.

It can be seen from Figure 3.1 that the reversible cell potential decreases with the increase of operating temperature. The calculated values of reversible cell potential (E_r) with pure hydrogen as fuel are 0.97741 V at 1073 K and 1 atm and 0.91923 V at 1273 K and 1 atm, which is consistent with Li [3] and Minh and Takahashi [93]. The decrease in reversible cell potential with increase in operating temperature for the fuel cell reaction given in Equation (3.7) is due to decrease in entropy change between the products and the reactants. This is attributed to the fact that there are less

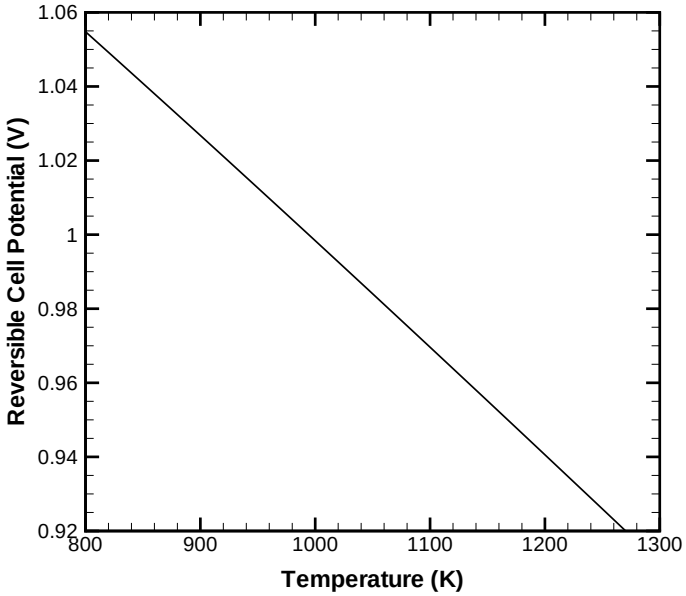

Figure 3.1: Effect of operating temperature on the reversible cell potential at 1 atm.

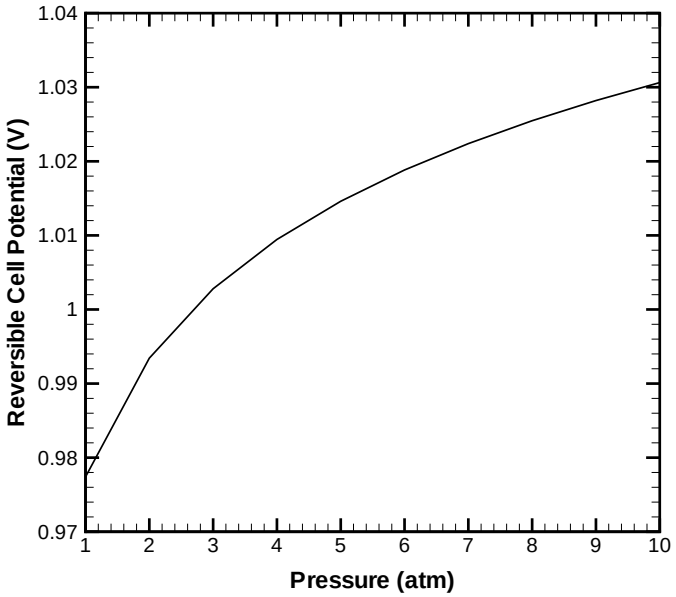

Figure 3.2: Effect of operating pressure on the reversible cell potential at 1073 K.

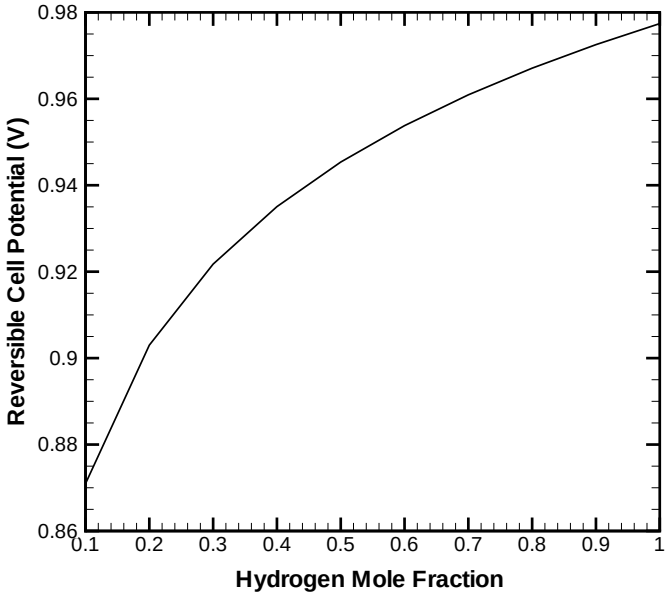

Figure 3.3: Effect of hydrogen mole fraction on the reversible cell potential at 1073 K and 1 atm.

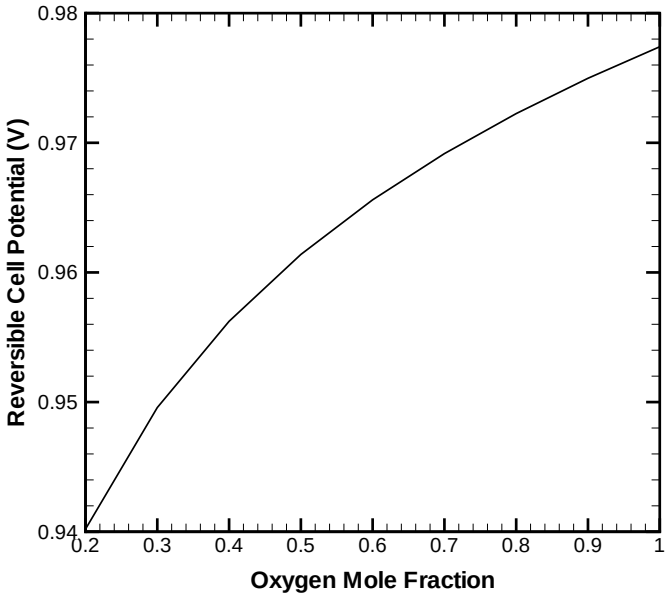

Figure 3.4: Effect of oxygen mole fraction on the reversible cell potential at 1073 K and 1 atm.

molecules in the products than in reactants for the fuel cell reaction given in Equation (3.7), which results in decreasing disorder or randomness with increasing temperature [3].

The effect of operating pressure on reversible cell potential (E_r) at 1073 K is shown in Figure 3.2. The reversible cell potential (E_r) increases with the increase of pressure. This is due to decrease in number of moles of gaseous species between the products and the reactants. Lastly, Figures 3.3 and 3.4 show the effect of mole fractions of hydrogen and oxygen on the reversible cell potential at 1073 K and 1 atm, respectively. It can be seen that increasing the concentration of reactants increases the reversible cell potential. This is due to decrease in Nernst loss with the increase in concentration of the reactants; in other words, less diluents in the reactant streams.

3.3 Summary

The maximum theoretical electric potential for a given fuel cell reaction at thermodynamic reversible condition is often referred to as the reversible cell potential. It can be determined using thermodynamic analysis, and is related to the change in Gibbs function between the products and the reactants for a given fuel cell reaction. It is a function of temperature, pressure and concentration of the reactants. Increasing the operating temperature decreases the reversible cell potential; whereas, increasing the pressure increases the reversible cell potential. Also, increasing the concentration of reactants increases the reversible cell potential.

Chapter 4

Model Formulation

This chapter deals with the development of mathematical model for SOFCs. The physical domain of the model is presented at the outset, followed by the assumptions considered in the development of the mathematical model. Then, the conservation equations governing the processes in the backing layers are presented in section 4.3. Then, the equations governing the processes in the reaction zone layers and electrolyte layer are presented in sections 4.4 and 4.5, respectively. Finally, the boundary conditions required to complete the model formulation are presented in section 4.6.

4.1 Physical Domain

The physical domain of an SOFC is shown in Figure 4.1. Part (a) of Figure 4.1 shows the three-dimensional representation of the physical domain with multiple channels; whereas, part (b) of Figure 4.1 shows the cross-sectional representation of a symmetric portion of the physical domain. The computational domain is shown by the dashed line, which includes the land portion of the interconnects interfacing the backing layers, the porous portion of the backing layers interfacing the flow channels, the backing layers, the reaction zone layers, and the electrolyte layer.

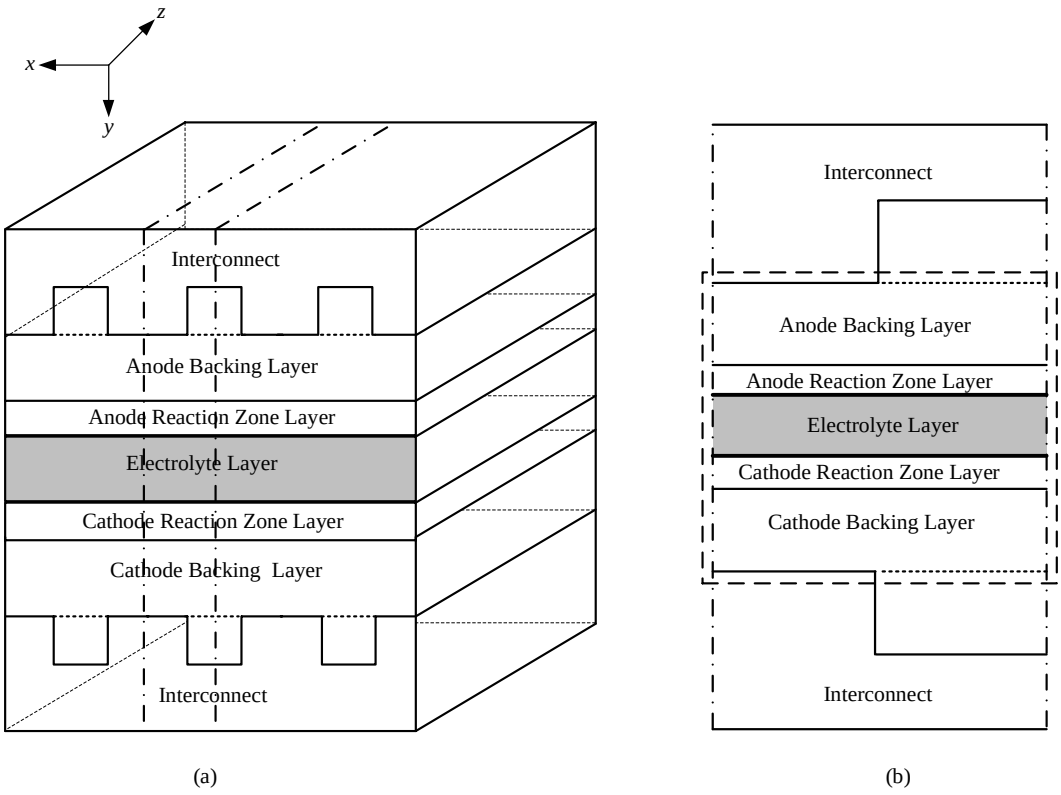

Figure 4.1: Physical domain of an SOFC: (a) 3-D view of a single cell with multiple channels, (b) cross-sectional view of a symmetric portion.

4.2 Assumptions

The cell is assumed to operate under steady state conditions. The convective flux is negligible in the porous backing and reaction zone layers when compared to the diffusive flux of gaseous species, which means the primary mode of species transport in the porous backing and reaction zone layers is by diffusion [9]. For instance, according to Yakabe [14], the calculated diffusion flux of H_2 at 1 A/cm^2 is about 0.23 mole/m^{2}s, which is four orders of magnitude higher than convective flux (1×10^{-4} mole/m^{2}s). The reactant gas mixtures are approximated as ideal gases with negligible Soret, Dofour and gravity effects. Further, radiation effects are considered to be negligible, which is consistent with findings of Damm and Fedorov [51] and Daun *et al.* [52]. Since the reaction zone layers are considered as distinct regions, there are no electrochemical reactions (either oxidation or reduction) in the backing layers. Reaction zone layers consist of porous mixtures of electron- and

ion-conducting particles, which can be modeled as composite electrodes. The macroscopic porous-electrode approach is used to model the reaction zone layers, which is based on the assumption that the reaction zone layers are represented by continuous-average quantities of electron- and ion-conducting particles packed together at random and disregards the actual geometric details of individual particles, and is considered to be the most practical approach for applied research [20]. It is also assumed that there is no electrochemical oxidation of CO in the anode reaction zone layer. Moreover, the electrolyte layer is assumed to be a dense solid and an electron insulator. Lastly, the thermophysical properties are assumed to be constant.

4.3 Backing Layers

The processes that need to be modeled in the backing layers are transport of multi-component mixture to and from the reaction sites in the reaction zone layers along with chemical reactions (reforming and water-gas shift), transport of electrons in the solid phase of the porous layers, and transport of energy due to heat conduction and species diffusion along with heat generation/consumption due to chemical reactions and electron migration. The conservation equations governing the processes in the backing layers are conservation of species, conservation of electric charge and conservation of energy. The mathematical model governing the processes in the backing layers is formulated by applying these conservation equations along with their constitutive equations. The following section presents the governing equations in the backing layers in more detail.

4.3.1 Conservation of Species

Consider a control volume (CV) "dxdydz" as shown in Figure 4.2.

The conservation statement for species "i" can be written as:

$$\begin{pmatrix} \text{Rate of accumulation} \\ \text{or depletion of species } i \\ \text{within the CV} \end{pmatrix} = \begin{pmatrix} \text{Net rate of species} \\ (\text{IN} - \text{OUT}) \end{pmatrix} + \begin{pmatrix} \text{Rate of production or} \\ \text{consumption of} \\ \text{species } i \end{pmatrix} \tag{4.1}$$

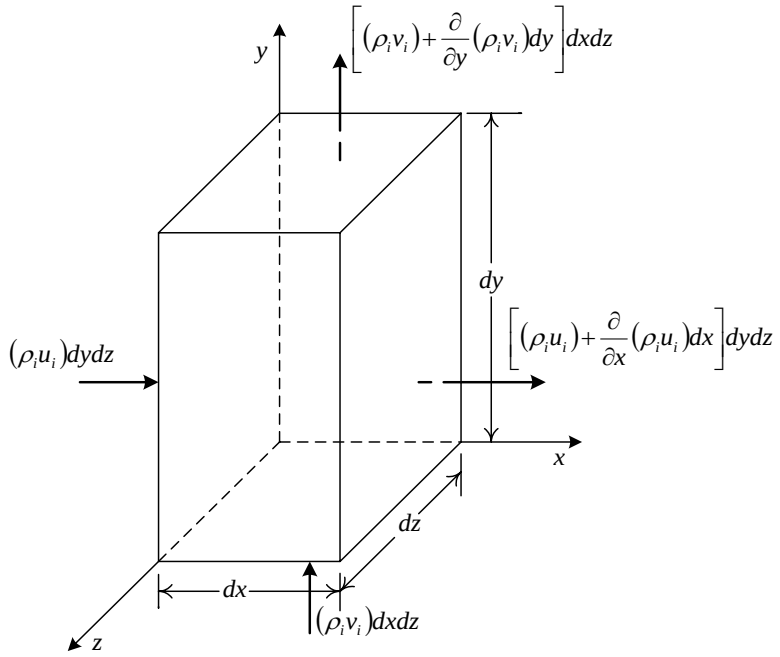

Figure 4.2: Control volume "dxdydz" showing the mass flux of species i

The above conservation statement can be expressed in the mathematical form as

$$\begin{aligned}\frac{\partial}{\partial t}\left(\rho_i dxdydz\right) &= \left(\rho_i u_i dydz\right) - \left(\rho_i u_i + \frac{\partial}{\partial x}\left(\rho_i u_i\right)dx\right)dydz \\ &+ \left(\rho_i v_i dxdz\right) - \left(\rho_i v_i + \frac{\partial}{\partial y}\left(\rho_i v_i\right)dy\right)dxdz \\ &+ \left(\rho_i w_i dxdy\right) - \left(\rho_i w_i + \frac{\partial}{\partial z}\left(\rho_i w_i\right)dz\right)dxdy \\ &+ \dot{S}_{s,i}dxdydz\end{aligned} \tag{4.2}$$

Substituting the absolute velocity of species "i" in terms of convection and diffusion components and invoking the steady state assumption, Equation (4.2) reduces to

$$\frac{\partial}{\partial x}\left[\rho_i\left(u+U_i\right)\right] + \frac{\partial}{\partial y}\left[\rho_i\left(v+V_i\right)\right] + \frac{\partial}{\partial z}\left[\rho_i\left(w+W_i\right)\right] = \dot{S}_{s,i} \tag{4.3}$$

where ρ_i is the density of species "i", u, v, and w are the convection or bulk motion velocity components in the x, y, and z directions, respectively. Similarly, U_i, V_i, and W_i are the diffusion

velocity components of species "i" in the x, y, and z directions, respectively, and $\dot{S}_{s,i}$ is the rate of production or consumption of species "i" per unit volume.

In a compact form, Equation (4.3) can be written as

$$\nabla \cdot \left\{ \rho_i \left(\overrightarrow{v} + \overrightarrow{V}_i \right) \right\} = \dot{S}_{s,i} \tag{4.4}$$

Equation (4.4) is also called species continuity equation [56]. The left hand side of Equation (4.4) comprises of convectional and diffusional fluxes. Since in the present formulation, the convectional flux is assumed to be negligible relative to the diffusional flux, the species continuity equation reduces to

$$\nabla \cdot \left(\rho_i \overrightarrow{V}_i \right) = \dot{S}_{s,i} \tag{4.5}$$

In terms of diffusional flux, the conservation of species in the backing layers can be represented as

$$\nabla \cdot \left(\overrightarrow{N}_i \right) = \dot{S}_{s,i} \tag{4.6}$$

where $\overrightarrow{N}_i$ is the molar diffusional flux of species i, and $\dot{S}_{s,i}$ represents the volumetric production or consumption of species i expressed in $\mathrm{mole\,m^{-3}\,s^{-1}}$.

The molar diffusional flux can be explicitly expressed as [56]:

$$\overrightarrow{N}_i = \overrightarrow{N}_i^{(c)} + \overrightarrow{N}_i^{(p)} + \overrightarrow{N}_i^{(g)} + \overrightarrow{N}_i^{(T)} \tag{4.7}$$

where $\overrightarrow{N}_i^{(c)}$, $\overrightarrow{N}_i^{(p)}$, $\overrightarrow{N}_i^{(g)}$, and $\overrightarrow{N}_i^{(T)}$ represent ordinary (concentration) diffusion, pressure diffusion, body-force diffusion and thermal diffusion (Soret effect), respectively.

In comparison with ordinary (concentration) diffusion, all other diffusion terms are negligible. Hence, the diffusion flux in the backing layer reduces to ordinary (concentration) diffusion, which means

$$\overrightarrow{N}_i = \overrightarrow{N}_i^{(c)} \tag{4.8}$$

The concentration diffusion flux can be obtained using any constitutive models such as Fick's law

of diffusion, Stefan-Maxwell model or Dusty-gas model. The one which provides the most general and convenient approach to describe the multi-component mass transport inside the porous layers is the Stefan-Maxwell model [38]. In multi-component diffusion having n components, the diffusive flux of each species depends on the concentration gradient of other $n-1$ species, and this dependence is evident in the Stefan-Maxwell model [57]. Further, the Stefan-Maxwell model can be modified to include the effect of Knudsen diffusion due to collisions between the gas molecules and the pore walls of the porous electrodes, which is described in more detail in the following subsection.

Modified Stefan-Maxwell Model for Multi-component Systems

The diffusion process inside porous electrode layers can be characterized by the Knudsen number, which is defined as [58]:

$$Kn = \frac{\lambda}{d_p} \tag{4.9}$$

where λ is the mean free path of the gas molecule and d_p is the pore diameter.

According to Kast and Hohenthanner [59], diffusion in porous media can be classified into three regimes:

- Continuum regime: $Kn < 0.01$
- Transition regime: $0.01 < Kn < 1$
- Knudsen regime: $Kn > 1$

Typically, in SOFC electrodes, both ordinary diffusion and Knudsen diffusion are comparable [46], which means diffusion in SOFC electrodes is in the transition regime.

For multi-component systems involving n species, the Stefan-Maxwell equations are given as [38]:

$$\bigtriangledown x_i = -\sum_{j=1}^{n} \left(\frac{x_i x_j}{D_{ij}} \right) \left(\overrightarrow{V}_i - \overrightarrow{V}_j \right) \tag{4.10}$$

Converting the diffusion velocities into diffusion fluxes through the following relation

$$\rho_i \overrightarrow{V}_i = \overrightarrow{N}_i M_i \Longrightarrow \overrightarrow{V}_i = \frac{\overrightarrow{N}_i M_i}{\rho_i} = \frac{\overrightarrow{N}_i M_i}{c_i M_i} = \frac{\overrightarrow{N}_i \forall}{n_i} = \frac{\overrightarrow{N}_i \forall}{x_i n} = \frac{\overrightarrow{N}_i}{x_i c} \tag{4.11}$$

we obtain

$$\bigtriangledown x_i = \sum_{j=1}^{n} \frac{1}{cD_{ij}} \left(x_i \overrightarrow{N}_j - x_j \overrightarrow{N}_i \right) \tag{4.12}$$

where c is the concentration of the mixture, D_{ij} is the ordinary diffusion coefficient of species i in j, x_i is the mole fraction of species i, and $\overrightarrow{N}_i$ is the diffusion flux of species i.

The above diffusion model takes into account only ordinary diffusion due to concentration gradient. However, in SOFC electrodes both ordinary and Knudsen diffusion occur simultaneously [39]. Knudsen diffusion occurs when pore size is small in comparison to mean free path of the gas molecules; as a result, molecules collide more frequently with the pore walls than with other molecules. Hence, the effect of Knudsen diffusion is included in the above model and expressed as

$$\bigtriangledown x_i = \sum_{j=1}^{n} \frac{1}{cD_{ij}} \left(x_i \overrightarrow{N}_j - x_j \overrightarrow{N}_i \right) + \frac{\overrightarrow{N}_i}{D_{Kn,i}} \tag{4.13}$$

where D_{ij} is the ordinary or binary diffusion coefficient and $D_{Kn,i}$ is the Knudsen diffusion coefficient of species i.

Mathematically, the two terms on the right hand side of Equation (4.13) can be combined to obtain the modified Stefan-Maxwell model for multi-component diffusion in the porous electrodes, and can be expressed in the original form of the Stefan-Maxwell model given in Equation (4.12) as

$$\bigtriangledown x_i = \sum_{j=1}^{n} \frac{1}{c\mathcal{D}_{ij}} \left(x_i \overrightarrow{N}_j - x_j \overrightarrow{N}_i \right) \tag{4.14}$$

where $\mathcal{D}_{ij}$ is the combined diffusion coefficient, defined as

$$\mathcal{D}_{ij} = \left(\frac{D_{ij} D_{Kn,i}}{D_{ij} + D_{Kn,i}} \right) \tag{4.15}$$

Ordinary or binary diffusion coefficients can be calculated using the Chapman-Enskog formula [56]:

$$D_{ij} = 1.8583 \times 10^{-7} \frac{\sqrt{T^3 \left(\frac{1}{M_i} + \frac{1}{M_i}\right)}}{p\sigma_{ij}^2 \Omega_{D,ij}} \tag{4.16}$$

where D_{ij} is in m^2/s, T is the temperature in K, p is the total pressure in atm, σ_{ij} is the collision diameter in ^oA and $\Omega_{D,ij}$ is a dimensionless function of temperature and intermolecular potential field.

Knudsen diffusion coefficients can be calculated using the following expression [58, 60]:

$$D_{Kn,i} = \frac{1}{3} d_p \sqrt{\frac{8RT}{\pi M_i}} \tag{4.17}$$

where d_p is the pore diameter, R is the universal gas constant in $\mathrm{J\,mole^{-1}\,K^{-1}}$, T is the temperature in K, and M_i is the molecular weight of species i in $\mathrm{kg\,mole^{-1}}$.

Since the backing layers as well as the reaction zone layers are porous structures, the combined diffusion coefficient $\mathcal{D}_{ij}$ is corrected with some geometric factors [57]. The correction factor which is commonly used in SOFC literature is a function of porosity and tortuosity. Hence, the combined effective diffusivity is obtained using the following relation [39, 46]:

$$\mathcal{D}_{ij}^{\text{eff}} = \frac{\varepsilon}{\tau} \mathcal{D}_{ij} \tag{4.18}$$

where ε and τ are porosity and tortuosity of the porous layers, respectively, which can be defined as [57]:

$$\varepsilon = \frac{\text{volume of void space}}{\text{total volume}} \tag{4.19}$$

$$\tau = \left(\frac{\text{actual path length}}{\text{point} - \text{to} - \text{point path length}} \right) \tag{4.20}$$

Replacing the combined diffusion coefficient with the effective combined diffusion coefficient,

the modified Stefan-Maxwell equations given in Equation (4.14) become

$$\bigtriangledown x_i = \sum_{j=1}^{n} \frac{1}{c\mathcal{D}_{ij}^{\text{eff}}} \left(x_i \overrightarrow{N}_j - x_j \overrightarrow{N}_i \right) \tag{4.21}$$

The above equations provide the implicit relationship between the mole fraction of species i and molar fluxes. Hence, it is difficult to obtain the numerical solution of the modified Stefan-Maxwell model without resorting to matrix formulation. Thus, matrix formulation of the modified Stefan-Maxwell model is the most convenient way of expressing molar fluxes in terms of mole fractions of species, which is described as follows.

Matrix Formulation of Modified Stefan-Maxwell Model for Multi-component Systems

The modified Stefan-Maxwell model given in Equation (4.14) can be written in a matrix form as [38]:

$$c\left(\bigtriangledown x_i\right) = -[B]\left(\overrightarrow{N}_i\right) \tag{4.22}$$

where $[B]$ is a square matrix of order $n-1$, whose elements are

$$B_{ii} = \frac{x_i}{\mathcal{D}_{in}^{\text{eff}}} + \sum_{k=1, i\neq k}^{n} \frac{x_k}{\mathcal{D}_{ik}^{\text{eff}}} \tag{4.23}$$

$$B_{ij} = -x_i \left(\frac{1}{\mathcal{D}_{ij}^{\text{eff}}} - \frac{1}{\mathcal{D}_{in}^{\text{eff}}} \right) \tag{4.24}$$

Multiplying Equation (4.22) with the inverse of $[B]$, we get

$$c\left[B\right]^{-1}\left(\bigtriangledown x_i\right) = -\left[B\right]^{-1}\left[B\right]\left(\overrightarrow{N}_i\right) \tag{4.25}$$

After simplification, we obtain

$$\left(\overrightarrow{N}_i\right) = -c\left[B\right]^{-1}\left(\bigtriangledown x_i\right) \tag{4.26}$$

The inverse of $[B]$ can be written as

$$[B]^{-1} = [\Gamma] = \begin{bmatrix} \Gamma_{11} & \Gamma_{12} & \cdots & \Gamma_{1,n-1} \\ \Gamma_{21} & \Gamma_{22} & \cdots & \Gamma_{2,n-1} \\ \vdots & & & \vdots \\ \Gamma_{n-1,1} & \Gamma_{n-1,2} & \cdots & \Gamma_{n-1,n-1} \end{bmatrix} \tag{4.27}$$

It is worthwhile to note that the elements of $[B]$ or the inverse of $[B]$ are not constants, but are functions of operating and design parameters such as temperature, pressure, species concentrations, pore size, porosity and tortuosity.

The diffusion fluxes of different species can be explicitly expressed as

$$\begin{aligned} \overrightarrow{N}_1 &= -c\left(\Gamma_{11}\nabla x_1 + \Gamma_{12}\nabla x_2 + \cdots + \Gamma_{1,n-1}\nabla x_{n-1}\right) \\ \overrightarrow{N}_2 &= -c\left(\Gamma_{21}\nabla x_1 + \Gamma_{22}\nabla x_2 + \cdots + \Gamma_{2,n-1}\nabla x_{n-1}\right) \\ &\vdots \\ \overrightarrow{N}_{n-1} &= -c\left(\Gamma_{n-1,1}\nabla x_1 + \Gamma_{n-1,2}\nabla x_2 + \cdots + \Gamma_{n-1,n-1}\nabla x_{n-1}\right) \end{aligned} \tag{4.28}$$

The above diffusion fluxes are substituted in Equation (4.5) to express the conservation of species in terms of gradients of mole fractions of species i.

Chemical Reaction Rate

The term on the right hand side of Equation (4.5) is the species source term, representing the rate of production or consumption of species due to chemical reactions in the backing layers. Since there is no chemical reaction in the cathode backing layer, the species source term in Equation (4.5) corresponds to zero; whereas, in the anode backing layer, the species source term represents the rate of production or consumption of species due to methane reforming and water-gas shift reactions. Methane reforming and water gas shift reactions are given as follows

- Methane reforming:

$$CH_4 + H_2O \rightleftharpoons 3H_2 + CO \qquad \Delta H_{298} = 206\,kJ/mole \tag{4.29}$$

- Water-gas shift:

$$CO + H_2O \rightleftharpoons H_2 + CO_2 \qquad \Delta H_{298} = -41.1\,kJ/mole \tag{4.30}$$

The volumetric reaction rates for the above reactions can be written as

$$r_r = k_{fr} p_{CH_4} p_{H_2O} - k_{br} p_{H_2}^3 p_{CO} \tag{4.31}$$

$$r_s = k_{fs} p_{CO} p_{H_2O} - k_{bs} p_{CO_2} p_{H_2} \tag{4.32}$$

where r_r and r_s are the volumetric reaction rates for methane reforming and water-gas shift reactions expressed in $\mathrm{mole\,m^{-3}\,s^{-1}}$, k_{fr} and k_{br} are the forward and backward reaction rate constants for the reforming reaction, respectively, and k_{fs} and k_{bs} are the forward and backward reaction rate constants for the water-gas shift reaction, respectively.

In terms of mole fractions, Equations (4.31) and (4.32) can be written as

$$r_r = p^2 \left[k_{fr} x_{CH_4} x_{H_2O} - p^2 k_{br} x_{H_2}^3 x_{CO} \right] \tag{4.33}$$

$$r_s = p^2 \left[k_{fs} x_{CO} x_{H_2O} - k_{bs} x_{CO_2} x_{H_2} \right] \tag{4.34}$$

where p is the total pressure.

The equilibrium constants for the methane reforming and water-gas shift reactions are obtained using the following empirical relations [61]:

$$K_{pr} \equiv \frac{k_{fr}}{k_{br}} = 1.0267 \times 10^{10} \times \exp(-0.2513\zeta^4 + 0.3665\zeta^3 + 0.5810\zeta^2 - 27.134\zeta + 3.2770) \tag{4.35}$$

$$K_{ps} \equiv \frac{k_{fs}}{k_{bs}} = \exp\left(-0.2935\zeta^3 + 0.635\zeta^2 + 4.1788\zeta + 0.3169\right) \tag{4.36}$$

where

$$\zeta = \frac{1000}{T\,(K)} - 1 \tag{4.37}$$

The forward reaction rate constants for the methane reforming and water-gas shift reactions are given as [61]:

$$k_{fr} = 2395 \exp\left(-\frac{231266}{RT}\right) \left(\text{mole}\,\text{m}^{-3}\,\text{Pa}^{-2}\,\text{s}^{-1}\right) \tag{4.38}$$

$$k_{fs} = 0.0171 \exp\left(-\frac{103191\ \text{J}\,\text{mole}^{-1}}{RT}\right) \left(\text{mole}\,\text{m}^{-3}\,\text{Pa}^{-2}\,\text{s}^{-1}\right) \tag{4.39}$$

where R is the universal gas constant and T is the temperature in K.

Knowing the forward reaction rate constants and equilibrium constants for the methane reforming and water-gas shift reactions, the backward reaction rate constants can be obtained using the first equality in Equations (4.35) and (4.36).

Finally, the rates of production or consumption of various species in the anode backing layer can be formulated as follows:

$$\dot{S}_{s,CH_4} = -r_r \tag{4.40}$$

$$\dot{S}_{s,H_2} = 3r_r + r_s \tag{4.41}$$

$$\dot{S}_{s,H_2O} = -r_r - r_s \tag{4.42}$$

$$\dot{S}_{s,CO} = r_r - r_s \tag{4.43}$$

$$\dot{S}_{s,CO_2} = r_s \tag{4.44}$$

4.3.2 Conservation of Electric Charge

In addition to the transport of reactant species through void spaces, electrons migrate through solid portion of the porous backing layers. The conservation statement for electric charge applied

to a differential control volume (CV) "dxdydz" shown in Figure 4.3 can be written as

$$\left(\begin{array}{c}\text{Rate of accumulation}\\ \text{of electric charge}\\ \text{within the CV}\end{array}\right) = \left(\begin{array}{c}\text{Net change of current}\\ \text{(IN} - \text{OUT)}\end{array}\right) + \left(\begin{array}{c}\text{Rate of production or}\\ \text{consumption of}\\ \text{electric charge}\end{array}\right) \tag{4.45}$$

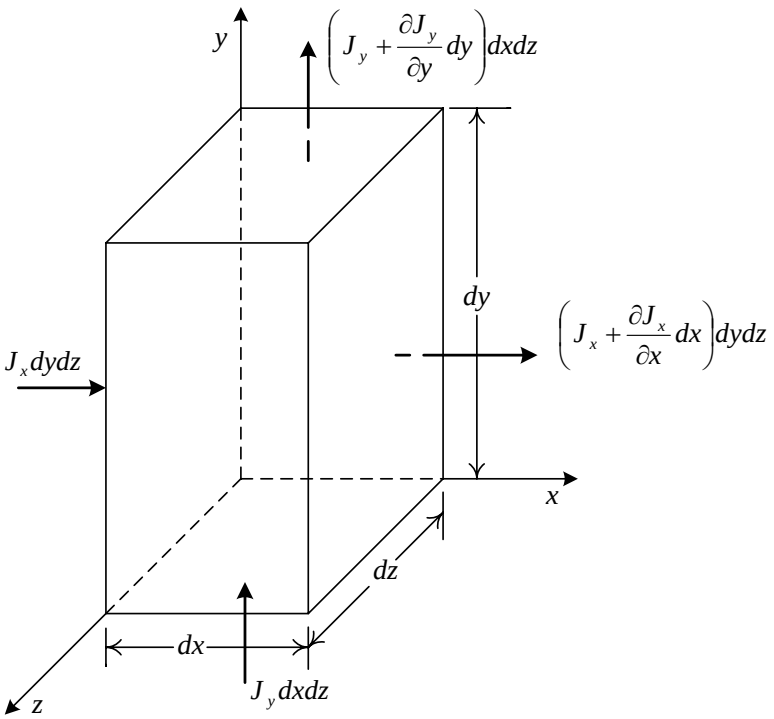

Figure 4.3: Control volume "dxdydz" showing the current density in x and y directions.

The above conservation statement can be expressed in mathematical form as

$$\begin{aligned} 0 \;=\; & (J_x dydz) - \left(J_x + \frac{\partial J_x}{\partial x} dx\right) dydz \\ & + (J_y dxdz) - \left(J_y + \frac{\partial J_y}{\partial y} dy\right) dxdz \\ & + (J_z dxdy) - \left(J_z + \frac{\partial J_z}{\partial z} dz\right) dxdy \\ & + \dot{S}_c dxdydz \end{aligned} \tag{4.46}$$

Simplifying the above equation, we get

$$\frac{\partial J_x}{\partial x} + \frac{\partial J_y}{\partial y} + \frac{\partial J_z}{\partial z} = \dot{S}_c \tag{4.47}$$

where J_x, J_y, and J_z are the current densities in the x, y, and z directions, respectively, and $\dot{S}_c$ is the rate of production or consumption of charge per unit volume.

In a compact form, Equation (4.47) can be written as

$$\nabla \cdot \left(\overrightarrow{J}\right) = \dot{S}_c \tag{4.48}$$

Replacing the current density ($\overrightarrow{J}$) with the electronic current density ($\overrightarrow{J_e}$), and assigning the source term to zero, since there is no production or consumption of electric charge in the backing layers, the above equation reduces to

$$\nabla \cdot \left(\overrightarrow{J_e}\right) = 0 \tag{4.49}$$

Converting the electronic current density into electronic potential through the Ohm's law, the above equation becomes

$$\nabla \cdot \left(\sigma_{\text{bl}}^{\text{eff}} \nabla \phi_e\right) = 0 \tag{4.50}$$

where $\sigma_{\text{bl}}^{\text{eff}}$ is the effective electronic conductivity of the backing layers, defined as

$$\sigma_{\text{bl}}^{\text{eff}} = \left(\frac{1-\varepsilon}{\tau}\right)\sigma \tag{4.51}$$

where ε and τ are porosity and tortuosity of the porous backing layers, respectively, and σ is the electronic conductivity of the backing layer material.

4.3.3 Conservation of Energy

Consider a control volume (CV) "dxdydz" shown in Figure 4.4. Writing the conservation statement for energy as

$$\begin{pmatrix}\text{Rate of change}\\ \text{of energy}\\ \text{within the CV}\end{pmatrix} = \begin{pmatrix}\text{Net rate of energy}\\ \text{into the CV}\\ \text{by convection}\end{pmatrix} + \begin{pmatrix}\text{Net rate of}\\ \text{heat addition}\\ \text{by conduction including}\\ \text{heat generation}\end{pmatrix} - \begin{pmatrix}\text{Net rate of}\\ \text{work done by}\\ \text{the CV on}\\ \text{surroundings}\end{pmatrix} \tag{4.52}$$

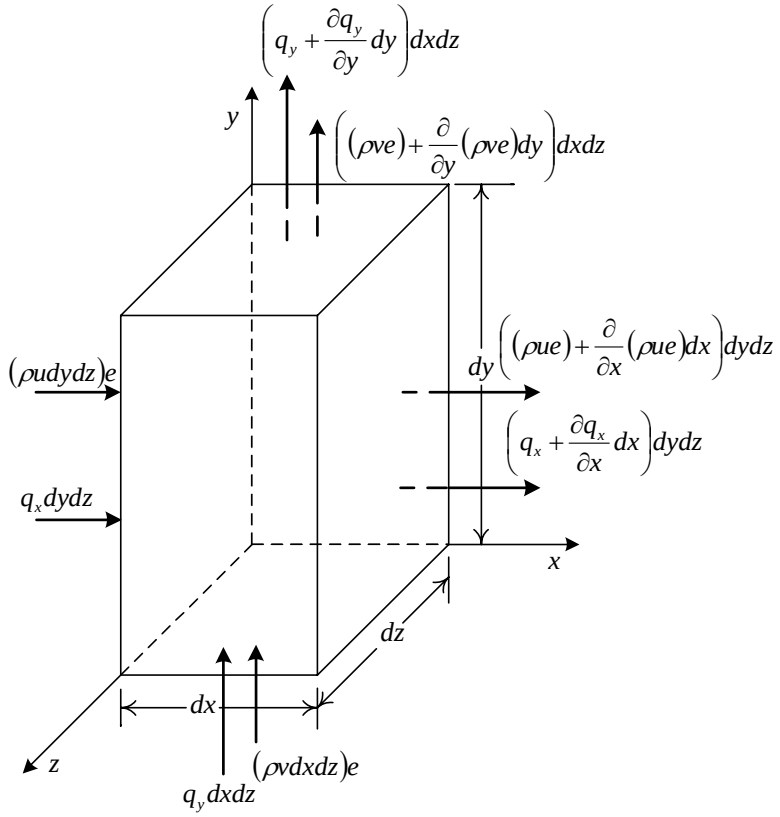

Figure 4.4: Control volume "dxdydz" showing the energy fluxes in x and y directions.

Figure 4.5 shows the rate of work done by the pressure and viscous stresses. Only viscous stresses in the x-direction are shown for clarity. Writing the above conservation statement in the

mathematical form as

$$\begin{aligned}\frac{\partial}{\partial t}\left(\rho e dxdydz\right) &= -\frac{\partial}{\partial x}\left(\rho ue\right)dxdydz - \frac{\partial}{\partial y}\left(\rho ve\right)dxdydz - \frac{\partial}{\partial z}\left(\rho we\right)dxdydz \\ &-\frac{\partial q_x}{\partial x}dxdydz - \frac{\partial q_y}{\partial y}dxdydz - \frac{\partial q_z}{\partial z}dxdydz + \dot{S}_e dxdydz \\ &-\frac{\partial\left(pu\right)}{\partial x}dxdydz - \frac{\partial\left(pv\right)}{\partial y}dxdydz - \frac{\partial\left(pw\right)}{\partial z}dxdydz \\ &+\rho g_x dxdydz + \rho g_y dxdydz + \rho g_z dxdydz \\ &+\frac{\partial}{\partial x}\left(u\tau_{xx}\right)dxdydz + \frac{\partial}{\partial y}\left(v\tau_{xy}\right)dxdydz + \frac{\partial}{\partial z}\left(w\tau_{xz}\right)dxdydz \\ &+\frac{\partial}{\partial x}\left(v\tau_{yx}\right)dxdydz + \frac{\partial}{\partial y}\left(v\tau_{yy}\right)dxdydz + \frac{\partial}{\partial z}\left(w\tau_{yz}\right)dxdydz \\ &+\frac{\partial}{\partial x}\left(w\tau_{zx}\right)dxdydz + \frac{\partial}{\partial y}\left(w\tau_{zy}\right)dxdydz + \frac{\partial}{\partial z}\left(w\tau_{zz}\right)dxdydz\end{aligned} \tag{4.53}$$

where e is the specific energy, which is the sum of internal and kinetic energies, and $\dot{S}_e$ is the volumetric heat source term.

Assuming the contributions of kinetic energy, gravitational potential energy, and work done by pressure and viscous stresses to be negligible, the above equation after invoking the steady state assumption reduces to

$$\rho\overrightarrow{v}\cdot\nabla U = -\nabla\cdot\overrightarrow{q} + \dot{S}_e - p\nabla\cdot\overrightarrow{v} \tag{4.54}$$

where U is the internal energy, and $\overrightarrow{q}$ is the heat flux.

For mixtures, the heat flux $\overrightarrow{q}$ is given as [56]:

$$\overrightarrow{q} = \overrightarrow{q}_c + \overrightarrow{q}_d + \overrightarrow{q}_x \tag{4.55}$$

where $\overrightarrow{q}_c$, $\overrightarrow{q}_d$, and $\overrightarrow{q}_x$ are flux due to heat conduction, flux due to interdiffusion of species, and flux due to Dufour or diffusion-thermo effect, respectively. Assuming the Dufour effect to be negligible, the heat flux becomes

$$\overrightarrow{q} = -k_{\text{bl}}^{\text{eff}}\nabla T + \sum_{i=1}^{n} h_i\rho_i\overrightarrow{V}_i \tag{4.56}$$

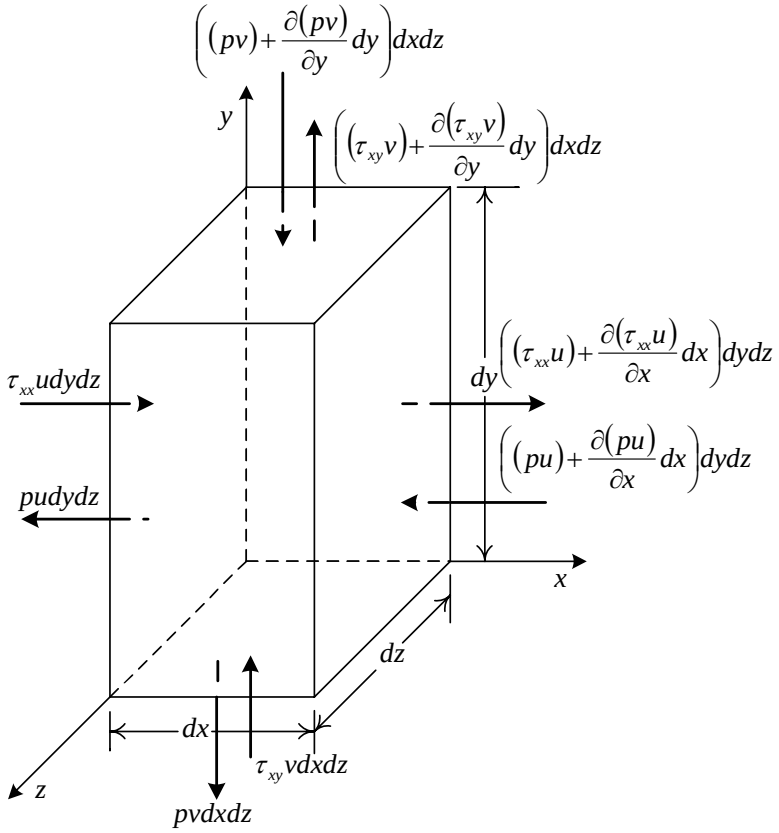

Figure 4.5: Rate of work done by the pressure and viscous stresses.

where $k_{\text{bl}}^{\text{eff}}$ is the effective thermal conductivity of the backing layers, h_i is the specific absolute enthalpy, ρ_i is the density of species i, and $\overrightarrow{V}_i$ is the species diffusion velocity.

Substituting the heat flux $\overrightarrow{q}$ in Equation (4.54), we have

$$\rho\overrightarrow{v}\cdot\nabla U+\nabla\cdot\left(\sum_{i=1}^{n}h_i\rho_i\overrightarrow{V}_i\right)+p\nabla\cdot\overrightarrow{v}=\nabla\cdot\left(k_{\text{bl}}^{\text{eff}}\nabla T\right)+\dot{S}_e \tag{4.57}$$

The term $(p\nabla\cdot\overrightarrow{v})$ can be replaced by $\left(\rho\overrightarrow{v}\cdot\nabla\left(\frac{p}{\rho}\right)\right)$ using continuity equation, we obtain

$$\rho\overrightarrow{v}\cdot\nabla\left(U+\frac{p}{\rho}\right)+\nabla\cdot\left(\sum_{i=1}^{n}h_i\rho_i\overrightarrow{V}_i\right)=\nabla\cdot\left(k_{\text{bl}}^{\text{eff}}\nabla T\right)+\dot{S}_e \tag{4.58}$$

Using the thermodynamic relation $\left(h = U + \frac{p}{\rho}\right)$, the above equation is simplified as

$$\rho \overrightarrow{v} \cdot \nabla h + \nabla \cdot \left(\sum_{i=1}^{n} h_i \rho_i \overrightarrow{V}_i \right) = \nabla \cdot \left(k_{\text{bl}}^{\text{eff}} \nabla T \right) + \dot{S}_e \tag{4.59}$$

Substituting $h = \sum_{i=1}^{n} y_i h_i$ in the above equation, we have

$$\rho \overrightarrow{v} \cdot \nabla \left(\sum_{i=1}^{n} y_i h_i \right) + \nabla \cdot \left(\sum_{i=1}^{n} h_i \rho_i \overrightarrow{V}_i \right) = \nabla \cdot \left(k_{\text{bl}}^{\text{eff}} \nabla T \right) + \dot{S}_e \tag{4.60}$$

where y_i is the mass fraction of species i.

The first term on the left hand side of the above equation can be expressed as

$$\rho \overrightarrow{v} \cdot \nabla \left(\sum_{i=1}^{n} (y_i h_i) \right) = \rho \overrightarrow{v} \cdot \sum_{i=1}^{n} (y_i \nabla h_i) + \rho \overrightarrow{v} \cdot \sum_{i=1}^{n} (h_i \nabla y_i) \tag{4.61}$$

From species continuity equation, we have

$$\rho \overrightarrow{v} \cdot \nabla y_i = \dot{S}_{s,i} - \nabla \cdot \left(\rho_i \overrightarrow{V}_i \right) \tag{4.62}$$

Substituting the above equation in Equation (4.61), the first term of the energy equation becomes

$$\rho \overrightarrow{v} \cdot \nabla \left(\sum_{i=1}^{n} (y_i h_i) \right) = \rho \overrightarrow{v} \cdot \left(\sum_{i=1}^{n} (y_i c_{pi}) \right) \nabla T + \sum_{i=1}^{n} h_i \left(\rho \overrightarrow{v} \cdot \nabla y_i \right) \tag{4.63}$$

$$\rho \overrightarrow{v} \cdot \nabla \left(\sum_{i=1}^{n} (y_i h_i) \right) = \rho c_p \overrightarrow{v} \cdot \nabla T + \sum_{i=1}^{n} \left(h_i \left[\dot{S}_{s,i} - \nabla \cdot \left(\rho_i \overrightarrow{V}_i \right) \right] \right) \tag{4.64}$$

where (∇h_i) is being replaced by $(c_{pi} \nabla T)$.

Replacing the first term of the energy equation with the above equation, the energy equation becomes

$$\rho c_p \overrightarrow{v} \cdot \nabla T + \nabla \cdot \left(\sum_{i=1}^{n} h_i \rho_i \overrightarrow{V}_i \right) = \nabla \cdot \left(k_{\text{bl}}^{\text{eff}} \nabla T \right) + \dot{S}_e - \sum_{i=1}^{n} h_i \dot{S}_{s,i} + \sum_{i=1}^{n} h_i \nabla \cdot \left(\rho_i \overrightarrow{V}_i \right) \tag{4.65}$$

The second term on the left hand side of the above equation can be written as

$$\nabla \cdot \left(\sum_{i=1}^{n} h_i \rho_i \overrightarrow{V}_i \right) = \sum_{i=1}^{n} h_i \nabla \cdot \left(\rho_i \overrightarrow{V}_i \right) + \sum_{i=1}^{n} \rho_i \overrightarrow{V}_i \cdot \nabla h_i \tag{4.66}$$

$$\nabla \cdot \left(\sum_{i=1}^{n} h_i \rho_i \overrightarrow{V}_i \right) = \sum_{i=1}^{n} h_i \nabla \cdot \left(\rho_i \overrightarrow{V}_i \right) + \sum_{i=1}^{n} \rho_i \overrightarrow{V}_i \cdot c_{pi} \nabla T \tag{4.67}$$

Substituting Equation (4.67) in Equation (4.65), the energy equation becomes

$$\rho c_p \overrightarrow{v} \cdot \nabla T + \sum_{i=1}^{n} \rho_i \overrightarrow{V}_i \cdot c_{pi} \nabla T = \nabla \cdot \left(k_{\text{bl}}^{\text{eff}} \nabla T \right) + \dot{S}_e - \sum_{i=1}^{n} h_i \dot{S}_{s,i} \tag{4.68}$$

Finally, invoking the assumption that the convective flux is negligible when compared to diffusive flux, the above energy equation becomes

$$\sum_{i=1}^{n} \rho_i \overrightarrow{V}_i \cdot c_{pi} \nabla T = \nabla \cdot \left(k_{\text{bl}}^{\text{eff}} \nabla T \right) + \dot{S}_e - \sum_{i=1}^{n} h_i \dot{S}_{s,i} \tag{4.69}$$

In terms of molar diffusional flux, the above equation can be represented as

$$\sum_{i=1}^{n} \left(\overline{c}_{pi} \overrightarrow{N}_i \right) \cdot \nabla T = \nabla \cdot \left(k_{\text{bl}}^{\text{eff}} \nabla T \right) + \dot{S}_e - \sum_{i=1}^{n} \overline{h}_i \dot{S}_{s,i} \tag{4.70}$$

where $\overline{c}_{pi}$ is the molar specific heat of species i at constant pressure, $\overline{h}_i$ is the specific molar absolute enthalpy, and $\overrightarrow{N}_i$ is the diffusion flux of species i.

Replacing the energy source term ($\dot{S}_e$) with the Joule heating term, ($\frac{J_e^2}{\sigma_{\text{bl}}^{\text{eff}}}$), representing the heat generation due to resistance to the electron flow in the solid phase of the backing layers, the energy equation becomes

$$\sum_{i=1}^{n} \left(\overline{c}_{pi} \overrightarrow{N}_i \right) \cdot \nabla T = \nabla \cdot \left(k_{\text{bl}}^{\text{eff}} \nabla T \right) + \frac{J_e^2}{\sigma_{\text{bl}}^{\text{eff}}} - \sum_{i=1}^{n} \overline{h}_i \dot{S}_{s,i} \tag{4.71}$$

where J_e is the electronic current density and $\sigma_{\text{bl}}^{\text{eff}}$ is the effective electronic conductivity in the backing layers.

The rate of heat production or consumption during chemical reactions is accounted by the last

term on the right hand side of Equation (4.71). Further, it is worthwhile to note that the last term on the right hand side of the above equation vanishes for the cathode backing layer since there is no chemical reaction in the cathode.

The effective thermal conductivity of the backing layers ($k_{\text{bl}}^{\text{eff}}$) is defined as

$$k_{\text{bl}}^{\text{eff}} = \varepsilon k_f + (1-\varepsilon)\, k_s \tag{4.72}$$

where k_f is the thermal conductivity of fluid mixture in the backing layers and k_s is the thermal conductivity of the solid phase of the porous backing layers.

The thermal conductivity of the multi-component fluid mixture is obtained as [62]:

$$k_f = \sum_{i=1}^{n} \frac{x_i k_i}{\left(\sum_{j=1}^{n} x_j \Phi_{ij}\right)} \tag{4.73}$$

where x_i is the mole fraction of species i in a mixture, k_i is the thermal conductivity of the component i, and Φ_{ij} is defined as

$$\Phi_{ij} = \frac{1}{\sqrt{8}} \left(1 + \frac{M_i}{M_j}\right)^{-\frac{1}{2}} \left[1 + \left(\frac{\mu_i}{\mu_j}\right)^{\frac{1}{2}} \left(\frac{M_j}{M_i}\right)^{\frac{1}{4}}\right]^2 \tag{4.74}$$

where M_i is the molecular weight of species i, and μ_i is the dynamic viscosity of the pure component i.

4.3.4 Non-dimensionalization of Governing Equations

The governing equations presented in the previous section are non-dimensionalized for better representation of variables into appropriate dimensionless groups. The set of dimensionless variables defined are as follows:

$$x^* = \frac{x}{t_{\text{bl}}} \qquad y^* = \frac{y}{t_{\text{bl}}} \qquad z^* = \frac{z}{t_{\text{bl}}}$$

$$N_{ix}^* = \frac{N_{ix}}{\left(\frac{J_{avg}}{nF}\right)} \qquad N_{iy}^* = \frac{N_{iy}}{\left(\frac{J_{avg}}{nF}\right)} \qquad N_{iz}^* = \frac{N_{iz}}{\left(\frac{J_{avg}}{nF}\right)}$$

$$T^* = \frac{T}{T_{op}} \qquad \phi_e^* = \frac{\phi_e}{E_r} \qquad J_{ex}^* = \frac{J_{ex}}{J_{avg}} \qquad J_{ey}^* = \frac{J_{ez}}{J_{avg}} \quad J_{ez}^* = \frac{J_{ez}}{J_{avg}}$$

where x^*, y^*, and z^* are dimensionless distances in the x, y, and z directions, respectively, t_{bl} is the characteristic backing layer thickness; N_{ix}^*, N_{iy}^*, and N_{iz}^* are the dimensionless diffusive fluxes of species i in x, y, and z directions, respectively; $\left(\frac{J_{avg}}{nF}\right)$ is the molar flux of reactant species, T^* is the dimensionless temperature, T_{op} is the specified cell operating temperature, ϕ_e^* is the dimensionless electronic potential, E_r is the reversible cell potential, and J_{ex}^*, J_{ey}^* and J_{ez}^* are the dimensionless electronic current densities in the x, y and z directions, respectively.

Using the above dimensionless variables, the governing equations for the backing layers are non-dimensionalized as follows

$$\text{Species}: \ \nabla \cdot (N_i^*) = E_{1,i} \tag{4.75}$$

where $E_{1,i}$ is a dimensionless parameter representing the ratio of rate of production or consumption of species i due to chemical reactions to the rate of molar diffusion of reactant species, which can be expressed as

$$E_{1,i} = \frac{\dot{S}_{s,i} t_{\text{bl}}}{\left(\frac{J_{avg}}{nF}\right)} \tag{4.76}$$

Since the mass transport model for multi-component diffusion has dimensions, it also needs to be non-dimensionalized. The modified Stefan-Maxwell model in non-dimensionalized form can be expressed as

$$\text{Modified Stefan} - \text{Maxwell Model}: \ (\bigtriangledown x_i) = -T^*[B^*]\left(\overrightarrow{N}_i^*\right) \tag{4.77}$$

where $(\bigtriangledown x_i)$ and $\left(\overrightarrow{N}_i^*\right)$ are column vectors, which can also be expressed as

$$(\nabla x_i) = \begin{pmatrix} \nabla x_1 \\ \nabla x_2 \\ \vdots \\ \nabla x_{n-1} \end{pmatrix} \tag{4.78}$$

$$\left(\overrightarrow{N_i^*}\right) = \begin{pmatrix} N_1^* \\ N_2^* \\ \vdots \\ N_{n-1}^* \end{pmatrix} \tag{4.79}$$

and $[B^*]$ is a dimensionless square matrix of order $n-1$, whose elements are defined as

$$B_{ii}^* = E_{2,in}x_i + \sum_{k=1,i\neq k}^{n} E_{2,ik}x_k \tag{4.80}$$

$$B_{ij}^* = -x_i\left(E_{2,ij} - E_{2,in}\right) \tag{4.81}$$

where $E_{2,ij}$ represents the ratio of molar diffusional flux of reactant species to the molar diffusional flux for pairs of binary species, which is expressed as

$$E_{2,ij} = \frac{\left(\frac{J_{avg}}{nF}\right)}{\left(\frac{c\mathcal{D}_{ij}^{\text{eff}}}{t_{\text{bl}}}\right)} \tag{4.82}$$

where c is the concentration of the mixture, and $\mathcal{D}_{ij}^{\text{eff}}$ is the effective combined diffusion coefficient.

Assuming the effective electronic conductivity and the effective thermal conductivity of the backing layers to be constant, the governing equations for electronic charge and energy in non-dimensional form can be represented as

$$\text{Electronic Charge}: \ \nabla^2\phi_e^* = 0 \tag{4.83}$$

$$\text{Energy}: \ \nabla^2 T^* - \left(\sum_{i=1}^{n} E_{3,i}\overrightarrow{N_i^*}\right)\cdot\nabla T^* + E_4\left(\overrightarrow{J_e^*}\right)^2 - \left(\sum_{i=1}^{n} E_{5,i}\right) = 0 \tag{4.84}$$

where $E_{3,i}$ represents the relative importance of energy transfer due to species diffusion to energy transfer due to heat conduction, E_4 represents the ratio of heat generation due to Joule heating to energy transfer due to heat conduction, and $E_{5,i}$ represents the ratio of heat production or consumption due to chemical reactions to the rate of conduction heat transfer. The above dimensionless

parameters can be expressed as

$$E_{3,i} = \frac{\overline{c}_{pi} J_{avg} t_{\rm bl}}{nF k_{\rm bl}^{\rm eff}} \tag{4.85}$$

$$E_4 = \frac{J_{avg}^2 t_{\rm bl}^2}{\sigma_{\rm bl}^{\rm eff} k_{\rm bl}^{\rm eff} T_{op}} \tag{4.86}$$

$$E_{5,i} = \frac{\overline{h}_i \dot{S}_{s,i} t_{\rm bl}^2}{k_{\rm bl}^{\rm eff} T_{op}} \tag{4.87}$$

The non-dimensionalized governing equations in the backing layers are summarized in Table 4.1.

Table 4.1: Non-dimensionalized governing equations in the backing layers.

Governing Equations	Anode backing layer	Cathode backing layer
Species	$\nabla \cdot (N_i^*) = E_{1,i}$	$\nabla \cdot (N_i^*) = 0$
Modified S-M Model	$(\bigtriangledown x_i) = -T^*[B^*]\left(\overrightarrow{N}_i^*\right)$	$(\bigtriangledown x_i) = -T^*[B^*]\left(\overrightarrow{N}_i^*\right)$
Electronic Charge	$\nabla^2 \phi_e^* = 0$	$\nabla^2 \phi_e^* = 0$
Energy	$\nabla^2 T^* - \left(\sum_{i=1}^{n} E_{3,i}\overrightarrow{N}_i^*\right) \cdot \nabla T^* + E_4\left(\overrightarrow{J}_e^*\right)^2 - \sum_{i=1}^{n} E_{5,i} = 0$	$\nabla^2 T^* - \left(\sum_{i=1}^{n} E_{3,i}\overrightarrow{N}_i^*\right) \cdot \nabla T^* + E_4\left(\overrightarrow{J}_e^*\right)^2 = 0$

4.4 Reaction Zone Layers

Reaction zone layers are relatively thin layers having thicknesses of the order of 10 μm. These are the regions where fuel and oxidant are electrochemically converted into electrical work, heat and water. Since the electron- and ion-conducting particles co-exist with the reactant species, these regions are often referred to as triple phase boundary regions (TPBRs), and can be treated as composite electrodes.

Reaction zone layers have been modeled as thin film models, random resistor network models, random packing sphere models or macroscopic porous-electrode models, respectively. The thin film models [63, 64] are based on the assumption that the three phases of the reaction zone layers (i.e., electronic, ionic, and gas) form straight paths from the electrolyte layer to the backing layers. Because of this assumption of thin film models, the reaction zone layers are represented by a very

ordered structure in place of highly disordered structure as observed in the experimental features of composite electrodes [20]. In random resistor network models [65,66], the composite electrode is assumed to consists of electron- and ion- conducting particles packed together to form a continuous network. These models involve storage of information in terms of individual particle locations and connectivity with other particles to construct resistor networks, followed with calculation of electric potential at each particle location. Due to high computational costs, the use of random resistor network models are limited to problems with small specimen size [36]. In random packing sphere models [29, 30, 32], the composite electrode is assumed as spherical particles of electron- and ion-conducting materials packed together at random. Due to randomness of these models, the random resistor network models and random packing sphere models are also referred to as Monte Carlo resistor network models and Monte Carlo packing sphere models, respectively. On the other hand, the macroscopic porous-electrode model is based on the assumption that the composite electrode is represented by the particles of electron- and ion-conducting materials packed together at random and disregards the actual geometric details of the individual particles. Instead, the composite electrode is described in terms of continuous-average quantities. Hence, in the present model, the macroscopic porous-electrode approach is used to model the reaction zone layers, which according to Sunde [20] is the most practical method for applied research.

The processes that need to be modeled in the reaction zone layers are transport of multi-component mixture to and from the reaction sites along with chemical (water-gas shift and reforming) and electrochemical reactions, transport of electrons and ions in the respective electron- and ion-conducting particles, and transfer of energy due to heat conduction and species diffusion along with heat generation/consumption due to chemical and electrochemical reactions and electron and ion migration.

The conservation equations in the reaction zone layers are similar to the backing layers except the source terms, which also account for the consumption or production of neutral or charged species due to electrochemical reactions. Following sub-sections present the governing equations in the reaction zone layers in more detail.

4.4.1 Conservation of Species

The conservation of species governing the transport of multi-component mixture in the reaction zone layers is similar to Equation (4.5), which can be expressed as

$$\nabla \cdot \left(\overrightarrow{N}_i\right) = \dot{S}_{s,i} \tag{4.88}$$

where the species source term ($\dot{S}_{s,i}$) accounts for the consumption or production of species due to electrochemical reactions in addition to the chemical reactions.

Again, the modified Stefan-Maxwell model given in Equation (4.14) is used to model multi-component diffusion in the reaction zone layers. Since in the reaction zone layers, species are produced or consumed due to electrochemical reactions, the task is to obtain the expression for volumetric reaction rate due to electrochemical reactions.

Electrochemical Reaction Rates

In general, an elementary electrochemical reaction can be written as follows [3]:

$$\sum_{i=1}^{N} \nu_i^{'} M_i \xrightarrow{k} \sum_{i=1}^{N} \nu_i^{''} M_i \tag{4.89}$$

where k is a reaction rate constant.

According to the law of mass action, the rate of reaction for species i is expressed in terms of $\mathrm{mole\,m^{-2}\,s^{-1}}$ as

$$r_i = \left(\nu_i^{''} - \nu_i^{'}\right) k \prod_{i=1}^{N} \left[M_i\right]^{\nu_i^{'}} \tag{4.90}$$

Then, Faraday's law relates the rate of electrochemical reaction in the reaction zone layers to the current density as

$$J = -nFr_i \tag{4.91}$$

where n is the number of electrons transferred during the electrochemical reaction and F is the Faraday's constant.

In the anode reaction zone layer, electrochemical oxidation of hydrogen occurs at the reactive sites (TPBs). The overall half-cell reaction in the anode reaction zone layer is

$$H_2 + O^{2-} \rightarrow H_2O + 2e^- \tag{4.92}$$

The above half-cell reaction is not a simple one step reaction, it involves many elementary reactions with intermediate species. The knowledge of elementary reactions during the electrochemical oxidation of hydrogen in SOFCs is still unknown and a subject of active research [67–69]. However, the concept of "rate-determining step" of an overall half-cell reaction is mostly used for the calculation of electrochemical reaction rate. The rate-determining step is defined as the reaction step which determines the rate of an overall reaction [3]. The rate-determining step for hydrogen oxidation reaction in the anode reaction zone layer of an SOFC could be dissociative adsorption of hydrogen, formation of hydroxyl ion, a charge transfer reaction, or desorption of water [46]. All of these rate determining reactions depend on the operating conditions and design parameters of the electrode. Assuming the charge transfer reaction as a single rate determining step, the reaction rate is related to the current density produced through Faraday's law as described above. The equation which provides the general relation between the current density and the anode overpotential (η_a) is often referred to as the Butler-Volmer equation, expressed as

$$J_{H_2} = J_o^{H_2} \left\{ \exp\left(\frac{\alpha n F \eta_a}{RT}\right) - \exp\left(-\frac{(1-\alpha)\, nF\eta_a}{RT}\right) \right\} \tag{4.93}$$

where $J_o^{H_2}$ is the exchange current density for the hydrogen oxidation reaction, η_a is the anode overpotential, α is the charge transfer coefficient (or symmetry factor), whose value lies between zero and one, and n is the number of electrons participating in the electrochemical reaction.

The exchange current density is a measure of electron transfer activity at the equilibrium electrode potential, i.e., when no current is being produced. It is a strong function of reactant

concentration and temperature, and can be obtained using the following expression [3]:

$$J_o^{H_2} = J_{o,ref}^{H_2} \left(\frac{x_{H_2}}{x_{H_2,ref}} \right)^{\gamma_{H_2}} \left(\frac{p}{p_{ref}} \right)^{\gamma_{H_2}} \left(\frac{T_{ref}}{T} \right)^{\gamma_{H_2}} \tag{4.94}$$

where $J_{o,ref}^{H_2}$ is the reference exchange current density for the hydrogen oxidation reaction measured at reference temperature (T_{ref}) and reference pressure (p_{ref}), and γ_{H_2} is the reaction order.

The anode overpotential η_a is defined as

$$\eta_a = \phi_i - \phi_e \tag{4.95}$$

where ϕ_i and ϕ_e are the potentials in the ion- and electron-conducting particles of the anode reaction zone layer, respectively.

In terms of volumetric current density produced in the anode reaction zone layer, the Butler-Volmer equation for hydrogen oxidation can be written as

$$\begin{aligned} \mathcal{R}_a &= A_v J_{o,ref}^{H_2} \left(\frac{x_{H_2}}{x_{H_2,ref}} \right)^{\gamma_{H_2}} \left(\frac{p}{p_{ref}} \right)^{\gamma_{H_2}} \left(\frac{T_{ref}}{T} \right)^{\gamma_{H_2}} \times \\ &\quad \times \left\{ \exp\left(\frac{\alpha n F \left(\phi_i - \phi_e \right)}{RT} \right) - \exp\left(-\frac{(1-\alpha)\, n F \left(\phi_i - \phi_e \right)}{RT} \right) \right\} \end{aligned} \tag{4.96}$$

where $\mathcal{R}_a$ is the volumetric current produced in the anode reaction zone layer, and A_v is the reactive surface area per unit volume.

Finally, the species source term in the anode reaction zone layer due to electrochemical oxidation reaction is related to volumetric current density produced through Faraday's law of electrochemical reaction and is expressed as

$$\dot{S}_{s,i} = -\frac{\nu_i \mathcal{R}_a}{nF} \tag{4.97}$$

where $\mathcal{R}_a$ is the volumetric current density produced in the anode reaction zone layer due to hydrogen oxidation, n is the number of electrons participating in the electrochemical reaction, F is the Faraday's constant, and ν_i is the stoichiometric coefficient of the species involved in the

oxidation reaction expressed in the following form [70]:

$$H_2 + O^{2-} - H_2O \rightarrow 2e^- \tag{4.98}$$

On the other hand, electrochemical reduction of oxygen occurs at the reactive sites in the cathode reaction zone layer. The overall half-cell reaction in the cathode reaction zone layer is

$$\frac{1}{2}O_2 + 2e^- \rightarrow O^{2-} \tag{4.99}$$

The above overall half-cell reaction in the cathode reaction zone layer involves a series of elementary reactions, such as oxygen adsorption and dissociation on the electrode surface, diffusion of intermediate species on the surface, charge transfer, and oxygen incorporation into the lattice of the electrolyte [46, 71]. Any of these reaction steps could be rate-determining step for the overall half-cell reaction in the cathode reaction zone layer. In order to identify the rate-determining step of the overall half-cell reaction in the cathode reaction zone layer, many studies which have been conducted; however, a generally accepted reaction model has not yet found [72–80]. Therefore, assuming a charge transfer reaction as the rate-determining step, the reaction rate during oxygen reduction in the cathode reaction zone layer is determined by using the Butler-Volmer equation, expressed as

$$J_{O_2} = J_o^{O_2} \left\{ \exp\left(-\frac{\alpha n F \eta_c}{RT}\right) - \exp\left(\frac{(1-\alpha)\, n F \eta_c}{RT}\right) \right\} \tag{4.100}$$

where $J_o^{O_2}$ is the exchange current density for the oxygen reduction reaction, η_c is the cathode overpotential.

The exchange current density for the oxygen reduction reaction can be obtained similar to the exchange current density for the hydrogen oxidation reaction, and can be expressed as

$$J_o^{O_2} = J_{o,ref}^{O_2} \left(\frac{x_{O_2}}{x_{O_2,ref}}\right)^{\gamma_{O_2}} \left(\frac{p}{p_{ref}}\right)^{\gamma_{O_2}} \left(\frac{T_{ref}}{T}\right)^{\gamma_{O_2}} \tag{4.101}$$

where $J_{o,ref}^{O_2}$ is the reference exchange current density for the oxygen reduction reaction measured

at reference temperature (T_{ref}) and reference pressure (p_{ref}), and γ_{O_2} is the reaction order.

Similarly, the cathode overpotential η_c is defined as

$$\eta_c = \phi_i - \phi_e \tag{4.102}$$

where ϕ_i and ϕ_e are the potentials in the ion- and electron-conducting particles of the cathode reaction zone layer, respectively.

Again, in terms of volumetric current density produced in the cathode reaction zone layer, the Butler-Volmer equation for the oxygen reduction reaction can be written as

$$\begin{aligned} \mathcal{R}_c &= A_v J^{O_2}_{o,ref} \left(\frac{x_{O_2}}{x_{O_2,ref}}\right)^{\gamma_{O_2}} \left(\frac{p}{p_{ref}}\right)^{\gamma_{O_2}} \left(\frac{T_{ref}}{T}\right)^{\gamma_{O_2}} \times \\ &\quad \times \left\{ \exp\left(-\frac{\alpha n F\left(\phi_i - \phi_e\right)}{RT}\right) - \exp\left(\frac{(1-\alpha)\, nF\left(\phi_i - \phi_e\right)}{RT}\right) \right\} \end{aligned} \tag{4.103}$$

where $\mathcal{R}_c$ is the volumetric current produced in the cathode reaction zone layer, and A_v is the reactive surface area per unit volume.

Again, the species source term in the cathode reaction zone layer due to electrochemical reduction reaction is related to volumetric current density produced through Faraday's law of electrochemical reaction, and is expressed as

$$\dot{S}_{s,i} = -\frac{\nu_i \mathcal{R}_c}{nF} \tag{4.104}$$

where $\mathcal{R}_c$ is the volumetric current density produced in the cathode reaction zone layer due to oxygen reduction reaction, n is the number of electrons participating in the electrochemical reaction, F is the Faraday's constant, and ν_i is the stoichiometric coefficient of the species involved in the reduction reaction expressed in the following form [70]:

$$\frac{1}{2}O_2 - O^{2-} \rightarrow 2e^- \tag{4.105}$$

Reactive Surface Area Per Unit Volume ($\mathbf{A}_v$)

In order to incorporate the microstructural effects into the model and thereby enhancing its predicting capability, the expression used to obtain the reactive surface per unit volume is given by Costamagna *et al.* [29]:

$$A_v = \pi \sin^2 \theta r_{el}^2 n_t n_{el} n_{io} \frac{Z_{el} Z_{io}}{Z} p_{el} p_{io} \tag{4.106}$$

where θ is the contact angle between electron- and ion-conducting particles in the reaction zone layers, r_{el} is the radius of the electron-conducting particles, n_t is the total number of particles per unit volume, n_{el} and n_{io} are the number fractions of electron- and ion-conducting particles in the reaction zone layers, respectively, Z_{el} and Z_{io} are the coordination numbers of electron- and ion-conducting particles in the reaction zone layers, respectively, Z is the total average number of contacts of each particle and p_{el} and p_{io} are the probabilities of electron- and ion-conducting particles in the reaction zone layers, respectively.

The parameters required to obtain the reactive surface area per unit volume (A_v) are calculated using the following expressions [20,29]. The total number of particles per unit volume in the reaction zone layer is given as

$$n_t = \frac{1-\varepsilon}{\frac{4}{3}\pi r_{el}^3 \left[n_{el} + (1-n_{el}) \left(\frac{r_{io}}{r_{el}} \right)^3 \right]} \tag{4.107}$$

where ε is the porosity of the reaction zone layers.

Similarly, the number fraction of electron-conducting particles in the reaction zone layer is given as

$$n_{el} = \frac{\Phi}{\left[\Phi + \frac{(1-\Phi)}{\left(\frac{r_{io}}{r_{el}} \right)^3} \right]} \tag{4.108}$$

where Φ is the volume fraction of the electron conducting particles in the reaction zone layers.

The coordination numbers for the electron- and ion-conducting particles in the reaction zone

layer are given as

$$Z_{el} = 3 + \frac{(Z-3)}{\left[n_{el} + (1-n_{el})\left(\frac{r_{io}}{r_{el}}\right)^2\right]} \tag{4.109}$$

$$Z_{io} = 3 + \frac{(Z-3)\left(\frac{r_{io}}{r_{el}}\right)^2}{\left[n_{el} + (1-n_{el})\left(\frac{r_{io}}{r_{el}}\right)^2\right]} \tag{4.110}$$

where Z is the total average coordination number, equal to 6 [20].

Finally, the probabilities of electron- and ion-conducting particles in the reaction zone layer are given as

$$p_{el} = \left[1 - (2 - Z_{el-el}/2)^{2.5}\right]^{0.4} \tag{4.111}$$

$$p_{io} = \left[1 - (2 - Z_{io-io}/2)^{2.5}\right]^{0.4} \tag{4.112}$$

where

$$Z_{el-el} = \frac{n_{el} Z_{el}^2}{Z} \tag{4.113}$$

$$Z_{io-io} = \frac{n_{io} Z_{io}^2}{Z} \tag{4.114}$$

4.4.2 Conservation of Electronic Charge

The conservation of electronic charge in the anode and cathode reaction zone layers can be obtained based on the derived equation given in Equation (4.49), and can be expressed as

- *Anode Reaction Zone Layer*:

$$\nabla \cdot \left(\overrightarrow{J_e}\right) = \mathcal{R}_a \tag{4.115}$$

- *Cathode Reaction Zone Layer*:

$$\nabla \cdot \left(\overrightarrow{J_e}\right) = -\mathcal{R}_c \tag{4.116}$$

Converting the electronic current density ($\overrightarrow{J_e}$) into electronic potential through the Ohm's law, the above equations become

- *Anode Reaction Zone Layer*:

$$\nabla \cdot \left(\sigma_{\mathrm{rl}}^{\mathrm{eff}} \nabla \phi_e \right) = -\mathcal{R}_a \tag{4.117}$$

- *Cathode Reaction Zone Layer*:

$$\nabla \cdot \left(\sigma_{\mathrm{rl}}^{\mathrm{eff}} \nabla \phi_e \right) = \mathcal{R}_c \tag{4.118}$$

where $\sigma_{\mathrm{rl}}^{\mathrm{eff}}$ is the effective electronic conductivity in the reaction zone layer, defined as follows [33]:

$$\sigma_{\mathrm{rl}}^{\mathrm{eff}} = \Phi \left(\frac{1-\varepsilon}{\tau} \right) \sigma \tag{4.119}$$

where Φ is the volume fraction of electron-conducting particles in the reaction zone layers, ε is the porosity of the reaction zone layers, τ is the tortuosity of the reaction zone layer, and σ is the conductivity of the electron-conducting particles.

4.4.3 Conservation of Ionic Charge

In the similar manner, the conservation of ionic charge in the anode and cathode reaction zone layers can be written as

- *Anode Reaction Zone Layer*:

$$\nabla \cdot \left(\overrightarrow{J_i} \right) = -\mathcal{R}_a \tag{4.120}$$

- *Cathode Reaction Zone Layer*:

$$\nabla \cdot \left(\overrightarrow{J_i} \right) = \mathcal{R}_c \tag{4.121}$$

Again, converting the ionic current density ($\overrightarrow{J_i}$) into ionic potential through the Ohm's law, the above equations become

- *Anode Reaction Zone Layer*:

$$\nabla \cdot \left(\kappa_{\mathrm{rl}}^{\mathrm{eff}} \nabla \phi_i \right) = \mathcal{R}_a \tag{4.122}$$

- *Cathode Reaction Zone Layer*:

$$\nabla \cdot \left(\kappa_{\mathrm{rl}}^{\mathrm{eff}} \nabla \phi_i\right) = -\mathcal{R}_c \tag{4.123}$$

where $\kappa_{\mathrm{rl}}^{\mathrm{eff}}$ is the effective ionic conductivity in the reaction zone layer, defined as [33]:

$$\kappa_{\mathrm{rl}}^{\mathrm{eff}} = (1-\Phi)\left(\frac{1-\varepsilon}{\tau}\right) \tag{4.124}$$

where Φ is the volume fraction of the electron conducting particles in the reaction zone layers, κ is the conductivity of the ion-conducting material.

4.4.4 Conservation of Energy

The conservation of energy equation in the reaction zone layers is similar to the backing layers except the source term, and can be expressed as

$$\sum_{i=1}^{n}\left(\overline{c}_{pi}\overrightarrow{N}_i\right)\cdot\nabla T = \nabla\cdot\left(k_{\mathrm{rl}}^{\mathrm{eff}}\nabla T\right) - \left(\sum_{i=1}^{n}\overline{h}_i\dot{S}_{s,i}\right) + \dot{S}_e \tag{4.125}$$

where $k_{\mathrm{rl}}^{\mathrm{eff}}$ is the effective thermal conductivity of the reaction zone layers, defined as

$$k_{\mathrm{rl}}^{\mathrm{eff}} = \varepsilon k_f + (1-\varepsilon)\left[\Phi k_{el} + (1-\Phi)\,k_{io}\right] \tag{4.126}$$

where k_f is the thermal conductivity of fluid mixture in the reaction zone layers, which can be obtained using Equation (4.73), Φ is the volume fraction of the electron conducting particles in the reaction zone layers, k_{el} and k_{io} are the thermal conductivities of the electron and ion-conducting particles, respectively.

The energy source term in the anode and cathode reaction zone layers are represented as

- *Anode Reaction Zone Layer*:

$$\dot{S}_e = \frac{\left|J_e^2\right|}{\sigma_{\mathrm{rl}}^{\mathrm{eff}}} + \frac{\left|J_i^2\right|}{\kappa_{\mathrm{rl}}^{\mathrm{eff}}} + \left|\frac{\mathcal{R}_a}{nF}\right|\left(-T\left(\Delta\bar{s}\right)_{H_{2,ox}}\right) + \mathcal{R}_a\eta_a \tag{4.127}$$

where the first term on right hand side (RHS), $\left(\frac{|J_e^2|}{\sigma_{\text{rl}}^{\text{eff}}}\right)$, represents the Joule heating effect due to resistance to the electron flow in the electron-conducting particles of the anode reaction zone layer, the second term, $\left(\frac{|J_i^2|}{\kappa_{\text{rl}}^{\text{eff}}}\right)$, represents the Joule heating effect due to resistance to the ion flow in the ion-conducting particles of the anode reaction zone layer, the third term, $\left(\left|\frac{\mathcal{R}_a}{nF}\right|\left(-T\left(\Delta\bar{s}\right)_{H_{2,ox}}\right)\right)$, represents the reversible heat generation due to electrochemical oxidation reaction, and the last term, $\mathcal{R}_a\eta_a$, represents the irreversible heat generation due to electrochemical oxidation reaction.

In order to find the reversible heat generation due to electrochemical reaction in the anode reaction zone layer, the entropy change between the products and the reactants has to be determined. However, entropy of formation for the ions and electrons are not known [70]. Therefore, entropy change for the overall SOFC reaction is determined in place of an overall half-cell reaction. The overall SOFC reaction is

$$H_2 + \frac{1}{2}O_2 \rightleftharpoons H_2O_{(g)} \tag{4.128}$$

The change in entropy between the products and reactants for the above SOFC reaction becomes

$$\left(\Delta\bar{s}\right)_{H_2} = \bar{s}_{H_2O} - \bar{s}_{H_2} - \frac{1}{2}\bar{s}_{O_2} \tag{4.129}$$

Assuming the entropy change in the anode reaction zone layer during electrochemical oxidation reaction to be a fraction of the entropy change for the overall SOFC reaction, the energy source term in the anode reaction zone layer becomes

$$\dot{S}_e = \frac{|J_e^2|}{\sigma_{\text{rl}}^{\text{eff}}} + \frac{|J_i^2|}{\kappa_{\text{rl}}^{\text{eff}}} + \left|\frac{\mathcal{R}_a}{nF}\right|\left(-T\xi_{H_2}\left(\Delta\bar{s}\right)_{H_2}\right) + \mathcal{R}_a\eta_a \tag{4.130}$$

where ξ_{H_2} is the fraction of entropy change for the overall SOFC reaction involving hydrogen.

- *Cathode Reaction Zone Layer*

$$\dot{S}_e = \frac{|J_e^2|}{\sigma_{\text{rl}}^{\text{eff}}} + \frac{|J_i^2|}{\kappa_{\text{rl}}^{\text{eff}}} + \left|\frac{\mathcal{R}_c}{nF}\right|\left(-T\left(1-\xi_{H_2}\right)\left(\Delta\bar{s}\right)_{H_2}\right) + \mathcal{R}_c\eta_c \tag{4.131}$$

where the first term on right hand side (RHS), $\left(\frac{\left|J_e^2\right|}{\sigma_{\mathrm{rl}}^{\mathrm{eff}}}\right)$, represents the Joule heating effect due to resistance to the electron flow in the electron-conducting particles of the cathode reaction zone layer, the second term, $\left(\frac{\left|J_i^2\right|}{\kappa_{\mathrm{rl}}^{\mathrm{eff}}}\right)$, represents the Joule heating effect due to resistance to the ion flow in the ion-conducting particles of the cathode reaction zone layer, the third term, $\left(\left|\frac{\mathcal{R}_c}{nF}\right|\left(-T(1-\xi_{H_2})\left(\Delta\bar{s}\right)_{H_2}\right)\right)$, represents the reversible heat generation due to electrochemical reduction reaction, and the last term, $\mathcal{R}_c\eta_c$, represents the irreversible heat generation due to electrochemical reduction reaction.

4.4.5 Non-dimensionalization of Governing Equations

The governing equations presented above for the reaction zone layers are non-dimensionalized by using the following dimensionless variables

$$x^* = \frac{x}{t_{\mathrm{rl}}} \qquad y^* = \frac{y}{t_{\mathrm{rl}}} \qquad z^* = \frac{z}{t_{\mathrm{rl}}}$$
$$N_{ix}^* = \frac{N_{ix}}{\left(\frac{J_{avg}}{nF}\right)} \qquad N_{iy}^* = \frac{N_{iy}}{\left(\frac{J_{avg}}{nF}\right)} \qquad N_{iz}^* = \frac{N_{iz}}{\left(\frac{J_{avg}}{nF}\right)}$$
$$T^* = \frac{T}{T_{op}} \qquad \phi_e^* = \frac{\phi_e}{E_r} \qquad \phi_i^* = \frac{\phi_i}{E_r}$$
$$J_{ex}^* = \frac{J_{ex}}{J_{avg}} \qquad J_{ey}^* = \frac{J_{ey}}{J_{avg}} \quad J_{ez}^* = \frac{J_{ez}}{J_{avg}}$$
$$J_{ix}^* = \frac{J_{ix}}{J_{avg}} \qquad J_{iy}^* = \frac{J_{iy}}{J_{avg}} \quad J_{iz}^* = \frac{J_{iz}}{J_{avg}}$$
$$\eta_a^* = \frac{\eta_a}{E_r} \qquad \eta_c^* = \frac{\eta_c}{E_r}$$
$$\mathcal{R}_a^* = \frac{\mathcal{R}_a}{A_v J_{o,ref}^{H_2}} \qquad \mathcal{R}_c^* = \frac{\mathcal{R}_c}{A_v J_{o,ref}^{O_2}}$$

where t_{rl} is the characteristic reaction zone thickness, η_a^* and η_c^* are dimensionless anode and cathode overpotential, respectively, and $\mathcal{R}_a^*$ and $\mathcal{R}_c^*$ are respective dimensionless volumetric current densities in the anode and cathode reaction zone layers.

Using the above dimensionless variables, the governing equations in the reaction zone layers are non-dimensionalized, and are presented as follows

$$\text{Species}: \nabla \cdot (N_i^*) = R_{1,i} \tag{4.132}$$

where $R_{1,i}$ is a dimensionless parameter representing the ratio of rate of production or consumption of species i due to chemical and electrochemical reactions to the rate of molar diffusion of reactant species, which is expressed as

$$R_{1,i} = \frac{\dot{S}_{s,i} t_{\mathrm{rl}}}{\left(\frac{J_{avg}}{nF}\right)} \tag{4.133}$$

Again, due to the presence of dimensions in the mass transport model, it also needs to be non-dimensionalized. The modified Stefan-Maxwell model in non-dimensionalized form can be expressed as

$$\text{Modified Stefan} - \text{Maxwell Model}: \ (\bigtriangledown x_i) = -T^*[B^*]\left(\overrightarrow{N}_i^*\right) \tag{4.134}$$

where $[B^*]$ is a dimensionless square matrix of order $n-1$, whose elements are defined as

$$B_{ii}^* = R_{2,in} x_i + \sum_{k=1, i\neq k}^{n} R_{2,ik} x_k \tag{4.135}$$

$$B_{ij}^* = -x_i \left(R_{2,ij} - R_{2,in}\right) \tag{4.136}$$

where $R_{2,ij}$ represents the ratio of molar diffusional flux of reactant species to the molar diffusional flux for pairs of binary species, which is defined as

$$R_{2,ij} = \frac{\left(\frac{J_{avg}}{nF}\right)}{\left(\frac{c\mathcal{D}_{ij}^{\mathrm{eff}}}{t_{\mathrm{rl}}}\right)} \tag{4.137}$$

where c is the concentration of the mixture and $\mathcal{D}_{ij}^{\mathrm{eff}}$ is the effective combined diffusion coefficient.

Assuming the effective electronic and ionic conductivities of the reactions layers to be constant, the governing equations for electronic and ionic charge in non-dimensional form can be represented as

- *Anode Reaction Zone Layer*:

$$\text{Electronic Charge}: \ \nabla^2 \phi_e^* = -R_3 \mathcal{R}_a^* \tag{4.138}$$

$$\text{Ionic Charge}: \nabla^2 \phi_i^* = R_4 \mathcal{R}_a^* \tag{4.139}$$

- *Cathode Reaction Zone Layer*:

$$\text{Electronic Charge}: \nabla^2 \phi_e^* = R_5 \mathcal{R}_c^* \tag{4.140}$$

$$\text{Ionic Charge}: \nabla^2 \phi_i^* = -R_6 \mathcal{R}_c^* \tag{4.141}$$

where R_3 and R_4 represent the ratios of potentials in the electron- and ion-conducting particles of the anode reaction zone layer for hydrogen oxidation reaction to the reversible cell potential; similarly, R_5 and R_6 represent the ratios of potentials in the electron- and ion-conducting particles of the cathode reaction zone layer for oxygen reduction reaction to the reversible cell potential, expressed as

$$R_3 = \frac{\left(\frac{t_{\text{rl}}^2 A_v J_{o,ref}^{H_2}}{\sigma_{\text{rl}}^{\text{eff}}} \right)}{E_r} \tag{4.142}$$

$$R_4 = \frac{\left(\frac{t_{\text{rl}}^2 A_v J_{o,ref}^{H_2}}{\kappa_{\text{rl}}^{\text{eff}}} \right)}{E_r} \tag{4.143}$$

$$R_5 = \frac{\left(\frac{t_{\text{rl}}^2 A_v J_{o,ref}^{O_2}}{\sigma_{\text{rl}}^{\text{eff}}} \right)}{E_r} \tag{4.144}$$

$$R_6 = \frac{\left(\frac{t_{\text{rl}}^2 A_v J_{o,ref}^{O_2}}{\kappa_{\text{rl}}^{\text{eff}}} \right)}{E_r} \tag{4.145}$$

The dimensionless volumetric current densities $\mathcal{R}_a^*$ and $\mathcal{R}_c^*$ produced in the anode and cathode reaction zone layers due to hydrogen oxidation and oxygen reduction reactions, respectively, are expressed as

$$\begin{aligned} \mathcal{R}_a^* &= \left(\frac{x_{H_2}}{x_{H_2,ref}} \right)^{\gamma_{H_2}} \left(\frac{p}{p_{ref}} \right)^{\gamma_{H_2}} \left(\frac{R_7}{T^*} \right)^{\gamma_{H_2}} \times \\ &\quad \times \left\{ \exp\left(\frac{\alpha R_8 \left(\phi_i^* - \phi_e^* \right)}{T^*} \right) - \exp\left(-\frac{(1-\alpha) R_8 \left(\phi_i^* - \phi_e^* \right)}{T^*} \right) \right\} \end{aligned} \tag{4.146}$$

$$\mathcal{R}_c^* = \left(\frac{x_{O_2}}{x_{O_2,ref}}\right)^{\gamma_{O_2}} \left(\frac{p}{p_{ref}}\right)^{\gamma_{O_2}} \left(\frac{R_7}{T^*}\right)^{\gamma_{O_2}} \times \left\{\exp\left(-\frac{\alpha R_8\left(\phi_i^* - \phi_e^*\right)}{T^*}\right) - \exp\left(\frac{(1-\alpha) R_8\left(\phi_i^* - \phi_e^*\right)}{T^*}\right)\right\} \tag{4.147}$$

where $R_7 = \frac{T_{ref}}{T_{op}}$ and $R_8 = \frac{E_r}{\left(\frac{RT_{op}}{nF}\right)}$.

The non-dimensionalized form of energy equation in the reaction zone layers can be expressed as

$$\text{Energy}: \nabla^2 T^* - \left(\sum_{i=1}^{n} R_{9,i}\overrightarrow{N_i^*}\right) \cdot \nabla T^* - \left(\sum_{i=1}^{n} R_{14,i}\right) + \dot{S}_e^* = 0 \tag{4.148}$$

where $R_{9,i}$ represents the relative importance of energy transfer due to species diffusion to energy transfer due to heat conduction, and $R_{14,i}$ represents the ratio of heat production or consumption during chemical reactions to the rate of conduction heat transfer. The dimensionless parameters are expressed as

$$R_{9,i} = \frac{\overline{c}_{pi} J_{avg} t_{\text{rl}}}{nF k_{\text{rl}}^{\text{eff}}} \tag{4.149}$$

$$R_{14,i} = \frac{\overline{h}_i \dot{S}_{s,i} t_{\text{rl}}^2}{k_{\text{rl}}^{\text{eff}} T_{op}} \tag{4.150}$$

The dimensionless energy source term ($\dot{S}_e^*$) in the anode and cathode reaction zone layers can be expressed as

- *Anode Reaction Zone Layer*:

$$\dot{S}_e^* = R_{10}\left(\overrightarrow{J_e^*}\right)^2 + R_{11}\left(\overrightarrow{J_i^*}\right)^2 - R_{12}\mathcal{R}_a^*\xi_{H_2} + R_{13}\mathcal{R}_a^*\eta_a^* \tag{4.151}$$

- *Cathode Reaction Zone Layer*:

$$\dot{S}_e^* = R_{10}\left(\overrightarrow{J_e^*}\right)^2 + R_{11}\left(\overrightarrow{J_i^*}\right)^2 - R_{12}\mathcal{R}_c^*\left(1 - \xi_{H_2}\right) + R_{13}\mathcal{R}_c^*\eta_c^* \tag{4.152}$$

where R_{10} and R_{11} represent the ratios of heat generation due to Joule heating to energy transfer due to heat conduction, and R_{12} and R_{13} represent the ratios of reversible and irreversible heat

generation during electrochemical reactions to the rate of conduction heat transfer, respectively. The above dimensionless parameters can be expressed as

$$R_{10} = \frac{J_{avg}^2 t_{\mathrm{rl}}^2}{\sigma_{\mathrm{rl}}^{\mathrm{eff}} k_{\mathrm{rl}}^{\mathrm{eff}} T_{op}} \tag{4.153}$$

$$R_{11} = \frac{J_{avg}^2 t_{\mathrm{rl}}^2}{\kappa_{\mathrm{rl}}^{\mathrm{eff}} k_{\mathrm{rl}}^{\mathrm{eff}} T_{op}} \tag{4.154}$$

$$R_{12} = \frac{t_{\mathrm{rl}}^2 A_v \left(J_{o,ref}^{H_2} / J_{o,ref}^{O_2}\right) \left(\Delta \bar{s}\right)_{H_2}}{nF k_{\mathrm{rl}}^{\mathrm{eff}}} \tag{4.155}$$

$$R_{13} = \frac{t_{\mathrm{rl}}^2 A_v \left(J_{o,ref}^{H_2} / J_{o,ref}^{O_2}\right) E_r}{nF k_{\mathrm{rl}}^{\mathrm{eff}} T_{op}} \tag{4.156}$$

The non-dimensionalized form of governing equations in the reaction zone layers are summarized in Table 4.2.

Table 4.2: Non-dimensionalized governing equations in the reaction zone layers.

Governing Equations	Anode reaction zone layer	Cathode reaction zone layer
Species	$\nabla \cdot (N_i^*) = R_{1,i}$	$\nabla \cdot (N_i^*) = R_{1,i}$
Modified S-M	$(\bigtriangledown x_i) = -T^*[B^*]\left(\overrightarrow{N}_i^*\right)$	$(\bigtriangledown x_i) = -T^*[B^*]\left(\overrightarrow{N}_i^*\right)$
Electronic Charge	$\nabla^2 \phi_e^* = -R_3 \mathcal{R}_a^*$	$\nabla^2 \phi_e^* = R_5 \mathcal{R}_c^*$
Ionic Charge	$\nabla^2 \phi_i^* = R_4 \mathcal{R}_a^*$	$\nabla^2 \phi_i^* = -R_6 \mathcal{R}_c^*$
Energy	$\nabla^2 T^* - \left(\sum_{i=1}^{n} R_{9,i} \overrightarrow{N}_i^*\right) \cdot \nabla T^*$	$\nabla^2 T^* - \left(\sum_{i=1}^{n} R_{9,i} \overrightarrow{N}_i^*\right) \cdot \nabla T^*$
	$+R_{10}\left(\overrightarrow{J}_e^*\right)^2 + R_{11}\left(\overrightarrow{J}_i^*\right)^2 - R_{12}\mathcal{R}_a^* \xi_{H_2}$	$+R_{10}\left(\overrightarrow{J}_e^*\right)^2 + R_{11}\left(\overrightarrow{J}_i^*\right)^2$
	$+R_{13}\mathcal{R}_a^* \eta_a^* - \sum_{i=1}^{n} R_{14,i} = 0$	$-R_{12}\mathcal{R}_c^*\left(1 - \xi_{H_2}\right) + R_{13}\mathcal{R}_c^* \eta_c^* = 0$

4.5 Electrolyte Layer

Electrolyte layer in an SOFC is fully dense with no interconnected porosity. The major function of the electrolyte is to conduct oxide ions produced in the cathode reaction zone layer to the anode reaction zone layer, thus completing the electrical circuit.

The processes that need to be modeled in the electrolyte layer are oxide ion transfer and energy transfer due to heat conduction. The conservation equations required to model the processes in the electrolyte layer are conservation of ionic charge and conservation of energy.

4.5.1 Conservation of Ionic Charge

The conservation of ionic charge in the electrolyte layer can be represented as

$$\nabla \cdot \overrightarrow{J}_i = 0 \tag{4.157}$$

where $\overrightarrow{J}_i$ is the ionic current density, which is equal to the total current density $\overrightarrow{J}$.

Using Ohm's law, the ionic current density is expressed in terms of ionic potential as

$$\overrightarrow{J}_i = -\kappa \nabla \phi_i \tag{4.158}$$

where κ is the ionic conductivity of the electrolyte layer.

Substituting Equation (4.158) into Equation (4.157) yields

$$\nabla \cdot (\kappa \nabla \phi_i) = 0 \tag{4.159}$$

4.5.2 Conservation of Energy

The conservation of energy equation in the electrolyte layer becomes

$$\nabla \cdot \overrightarrow{q} = \dot{S}_e \tag{4.160}$$

where $\overrightarrow{q}$ is the conduction heat flux, and $\dot{S}_e$ is the energy source term representing the heat generation due to resistance to the transport of oxide ions in the electrolyte layer, which is expressed as

$$\dot{S}_e = \frac{J^2}{\kappa} \tag{4.161}$$

Using Fourier's law of heat conduction, the conservation of energy equation in the electrolyte layer becomes

$$\nabla \cdot (k_{\text{el}} \nabla T) + \frac{J^2}{\kappa} = 0 \tag{4.162}$$

where k_{el} is the thermal conductivity of the electrolyte layer.

4.5.3 Non-dimensionalization of Governing Equations

The governing equations in the electrolyte layer are non-dimensionalized using the following dimensionless variables:

$$x^* = \frac{x}{t_{\text{el}}} \qquad y^* = \frac{y}{t_{\text{el}}} \qquad z^* = \frac{z}{t_{\text{el}}}$$
$$T^* = \frac{T}{T_{op}} \qquad \phi_i^* = \frac{\phi_i}{E_r}$$
$$J_x^* = \frac{J_x}{J_{avg}} \qquad J_y^* = \frac{J_y}{J_{avg}} \quad J_z^* = \frac{J_z}{J_{avg}}$$

where t_{el} is the characteristic electrolyte layer thickness.

Using the above dimensionless variables, the non-dimensionalized governing equations in the electrolyte layer can be expressed as

$$\text{Ionic Charge}: \ \nabla^2 \phi_i^* = 0 \tag{4.163}$$

$$\text{Energy}: \ \nabla^2 T^* + E_l \left(\overrightarrow{J^*}\right)^2 = 0 \tag{4.164}$$

where E_l is the dimensionless parameter representing the rate of heat generation due to resistance to the migration of oxide ions to the rate of heat conduction, expressed as

$$E_l = \frac{\left(\frac{J_{avg}^2}{\kappa}\right)}{\left(\frac{kT_{op}}{t_{\text{el}}^2}\right)} \tag{4.165}$$

The non-dimensionalized form of governing equations in the electrolyte layer are summarized in Table 4.3.

Table 4.3: Non-dimensionalized governing equations in the electrolyte layer.

Governing Equations	Electrolyte layer
Ionic Charge	$\nabla^2 \phi_i^* = 0$
Energy	$\nabla^2 T^* + E_l \left(\overrightarrow{J^*}\right)^2 = 0$

4.6 Boundary Conditions

In order to complete the model formulation of an SOFC, boundary conditions at different locations are required. Further, due to interdependent transport processes in different components of an SOFC, the definition of boundary conditions involve both external and internal boundary conditions [81]. The locations at which boundary conditions are required in the model are illustrated in Figure 4.6. The locations of the external boundary conditions are represented as E1, E2, E3, E4, E5, and E6; whereas, the locations of the internal boundary conditions are represented as I1, I2, I3, and I4.

Since a symmetric portion of the physical domain is considered as a computational domain for the present model, the boundary conditions applicable at boundaries E1 and E4 are symmetric boundary conditions, which can be expressed in mathematical form as

$$\left.\begin{array}{l} \frac{\partial x_i}{\partial x^*} = 0 \\ \frac{\partial \phi_e^*}{\partial x^*} = 0 \\ \frac{\partial \phi_i^*}{\partial x^*} = 0 \\ \frac{\partial T^*}{\partial x^*} = 0 \end{array}\right\} \tag{4.166}$$

The boundaries E2 and E6 represent the interfaces between the gas channels and the backing layers, where composition of the reactant species are specified based on the current density drawn from the cell, electronic current densities are zero and convective boundary conditions are applied for the energy equation. The composition of reactant species along the channel is calculated based on the assumption that the current density is constant. Accordingly, the mean mole fraction of

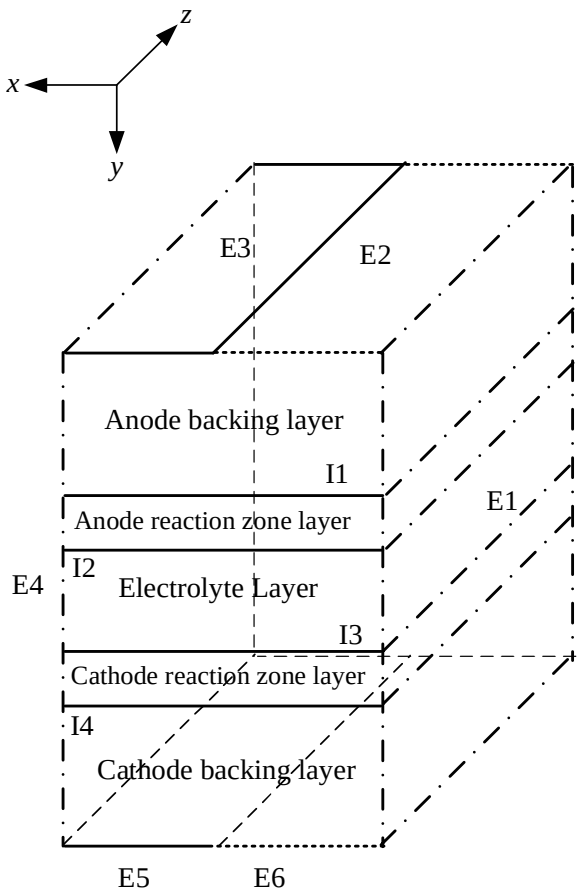

Figure 4.6: Illustration of locations at which external and internal boundary conditions are required in the model.

reactant species decreases linearly along the channel, and is expressed as [3]:

$$x_{i,m}(z) = x_{i,m,in} - \frac{\left(\frac{J_{avg}}{cnF}\right)}{bv_m} z \tag{4.167}$$

where $x_{i,m,in}$ is the mean mole fraction of the reactant species at the inlet of the channel, J_{avg} is the average current density drawn from the cell, n is the mole of electrons transferred per mole of reactant consumed, F is the Faraday's constant, c is the concentration of the reactant mixture, b is the width of the gas channel, v_m is the mean velocity of the reactant mixture, and z is the distance along the channel.

Knowing the mean mole fraction of reactant species along the channel, the mole fraction of the

reactant species at the surface of the backing layers can be obtained as

$$x_{i,s}(z) = x_{i,m,in} - \left(\frac{J_{avg}}{cnF}\right)\left[\frac{z}{bv_m} - \frac{1}{h_m}\right] \tag{4.168}$$

where h_m is the mass transfer coefficient over the backing layer surface, which can be obtained based on the definition of Sherwood (Sh) number. For uniform surface mass flux, the value of Sherwood (Sh) number is given as 5.39 [3].

In non-dimensional form, the above equation can be written as

$$x_{i,s}(z^*) = x_{i,m,in} - B_1 - B_2 z^* \tag{4.169}$$

where B_1 and B_2 are dimensionless parameters, defined as

$$B_1 = \frac{\left(\frac{J_{avg}}{nF}\right)}{ch_m} \tag{4.170}$$

$$B_2 = \frac{\left(\frac{J_{avg}}{nF}\right)t_{\mathrm{bl}}}{cbv_m} \tag{4.171}$$

where t_{bl} is the characteristic backing layer thickness.

The boundary conditions applicable for the electronic potential at external boundaries E2 and E6 are insulated electronic current densities, which means

$$\frac{\partial \phi_e^*}{\partial y^*} = 0 \tag{4.172}$$

Similarly, the boundary conditions applicable for the energy equation at external boundaries E2 and E6 can be expressed mathematically as

$$-k_{\mathrm{bl}}^{\mathrm{eff}}\frac{\partial T}{\partial y} = h\left(T - T_m\right) \tag{4.173}$$

where $k_{\mathrm{bl}}^{\mathrm{eff}}$ is the thermal conductivity of the backing layer, T is the surface temperature, T_m is the

mean temperature of the reactant mixture in the channel, and h is average heat transfer coefficient, which can be determined by using the definition of Nusselt (Nu) number. The value of Nusselt (Nu) number is given as 3.09 for laminar flow conditions in the gas channels of SOFCs [82].

In terms of dimensionless variable and parameters, the boundary condition becomes

$$\frac{\partial T^*}{\partial y^*} = -B_3 T^* + B_4 \tag{4.174}$$

where B_3 and B_4 are dimensionless parameters, defined as

$$B_3 = \frac{h t_{\text{bl}}}{k_{\text{bl}}^{\text{eff}}} \tag{4.175}$$

$$B_4 = \frac{h t_{\text{bl}} T_m}{k_{\text{bl}}^{\text{eff}} T_{op}} \tag{4.176}$$

where T_{op} is the operating temperature of the cell.

The boundaries E3 and E5 represent the land portions of the interconnects which are in contact with the backing layers, where the mass fluxes of species are zero, electronic potential is specified. Since the computational domain only includes the land portions of the interconnects, the temperatures are specified at boundaries E3 and E5 as first approximations, instead of continuous heat flux boundary conditions, which are applicable when the interconnects are included in the computational domain. The boundary conditions at external boundaries E3 and E5 can be expressed in mathematical form as

$$\left.\begin{aligned} \overrightarrow{N}_i^* \cdot \overrightarrow{n} &= 0 \\ \phi_e^* &= \text{Specified} \\ T^* &= \text{Specified} \end{aligned}\right\} \tag{4.177}$$

The internal boundaries I1 and I4 represent the interfaces between the backing and reaction zone layers. The boundary conditions at these boundaries are continuous flux boundary conditions for gaseous species and electronic potential, where the molar flux of species and electronic current density are continuous; whereas, insulated boundary condition for ionic potential, which implies

ionic current density is zero. In mathematical form, the boundary conditions are

$$\left.\begin{aligned} \overrightarrow{N}_i^* \cdot \overrightarrow{n}|_{\text{bl}} &= \overrightarrow{N}_i^* \cdot \overrightarrow{n}|_{\text{rl}} \\ \overrightarrow{J}_e^* \cdot \overrightarrow{n}|_{\text{bl}} &= \overrightarrow{J}_e^* \cdot \overrightarrow{n}|_{\text{rl}} \\ \overrightarrow{J}_i^* \cdot \overrightarrow{n} &= 0 \\ \overrightarrow{q}^* \cdot \overrightarrow{n}|_{\text{bl}} &= \overrightarrow{q}^* \cdot \overrightarrow{n}|_{\text{rl}} \end{aligned}\right\} \tag{4.178}$$

The interfaces between the reaction zone layers and electrolyte are represented by I2 and I3. Since the electrolyte is an electron insulator with no interconnected porosity, the molar flux of species and electronic current density are zero at these internal boundaries. On the other hand, the boundary condition for ionic potential varies depending upon on the approach used in fuel cell modeling. As it is known in fuel cell modeling, either current density is specified to obtain the cell potential or vice-versa. When current density is specified, the ionic current density at these boundaries (I2 and I3) is set equal to the total current density; however, when cell potential is specified to obtain the current density, the ionic current density at these boundaries (I2 and I3) is continuous. Similarly, the heat flux is continuous at these boundaries irrespective of the approach used for fuel cell modeling. In mathematical form, internal boundary conditions at I2 and I3 are expressed as

$$\left.\begin{aligned} &\overrightarrow{N}_i^* \cdot \overrightarrow{n} = 0 \\ &\overrightarrow{J}_e^* \cdot \overrightarrow{n} = 0 \\ &\overrightarrow{J}_i^* \cdot \overrightarrow{n} = J \text{ (Current Density Approach)} \\ &\overrightarrow{J}_i^* \cdot \overrightarrow{n}|_{\text{rl}} = \overrightarrow{J}_i^* \cdot \overrightarrow{n}|_{\text{el}} \text{ (Cell Potential Approach)} \\ &\overrightarrow{q}^* \cdot \overrightarrow{n}|_{\text{rl}} = \overrightarrow{q}^* \cdot \overrightarrow{n}|_{\text{el}} \end{aligned}\right\} \tag{4.179}$$

Finally, the boundary conditions at different boundaries shown in Figure 4.6 are summarized in Table 4.4.

Table 4.4: Boundary conditions.

External/Interface locations	Boundary conditions
E1 and E4	$\frac{\partial x_i}{\partial x^*} = 0$ $\frac{\partial \phi_e^*}{\partial x^*} = 0$ $\frac{\partial \phi_i^*}{\partial x^*} = 0$ $\frac{\partial T^*}{\partial x^*} = 0$
E2 and E6	$x_{i,s}(z^*) = x_{i,m,in} - B_1 - B_2 z^*$ $\frac{\partial \phi_e^*}{\partial y^*} = 0$ $\frac{\partial T^*}{\partial x^*} = -B_3 T^* + B_4$
E3 and E5	$\overrightarrow{N}_i^* \cdot \overrightarrow{n} = 0$ $\phi_e^* = \text{Specified}$ $T^* = \text{Specified}$
I1 and I4	$\overrightarrow{N}_i^* \cdot \overrightarrow{n}\|_{\text{bl}} = \overrightarrow{N}_i^* \cdot \overrightarrow{n}\|_{\text{rl}}$ $\overrightarrow{J}_e^* \cdot \overrightarrow{n}\|_{\text{bl}} = \overrightarrow{J}_e^* \cdot \overrightarrow{n}\|_{\text{rl}}$ $\overrightarrow{J}_i^* \cdot \overrightarrow{n} = 0$ $\overrightarrow{q}^* \cdot \overrightarrow{n}\|_{\text{bl}} = \overrightarrow{q}^* \cdot \overrightarrow{n}\|_{\text{rl}}$
I2 and I3	$\overrightarrow{N}_i^* \cdot \overrightarrow{n} = 0$ $\overrightarrow{J}_e^* \cdot \overrightarrow{n} = 0$ $\overrightarrow{J}_i^* \cdot \overrightarrow{n} = J$ (Current Density Approach) $\overrightarrow{J}_i^* \cdot \overrightarrow{n}\|_{\text{rl}} = \overrightarrow{J}_i^* \cdot \overrightarrow{n}\|_{\text{el}}$ (Cell Potential Approach) $\overrightarrow{q}^* \cdot \overrightarrow{n}\|_{\text{rl}} = \overrightarrow{q}^* \cdot \overrightarrow{n}\|_{\text{el}}$

4.7 Summary

The equations forming the set of governing equations are conservation of species, conservation of electric charge for the electron- and ion-conducting particles, and conservation of energy. On the anode side of the cell, the conservation of species can be written for species i corresponding to methane, hydrogen, water vapor, carbon monoxide and carbon dioxide. Similarly, on the cathode side, conservation of species can be written for species i corresponding to oxygen and nitrogen. In addition, in the backing layers, we need an equation to solve for temperature and electronic potential. Therefore, the set of governing equations in the anode and cathode backing layers contain a total of six and three equations, respectively.

Since the present model treats the reaction zone layers as finite volumes, the conservation equations in these layers also need to be solved. In addition to the number of equations in the

backing layers, there is an additional equation which needs to be solved for the ionic potential in the reaction zone layers. Thus, there are seven equations in the anode reaction zone layer and four equations in the cathode reaction zone layer to be solved for, thereby highlighting the complexity in considering the reaction zone layers as finite volumes.

In the electrolyte layer, there are two governing equations to be solved for the ionic potential and temperature. Overall, the complete mathematical model consists of twenty-two equations, which are required to be solved to obtain the numerical solution. The numerical procedure employed to solve these governing equations is presented in the next chapter.

Chapter 5

Numerical Implementation

This chapter describes the numerical scheme used to discretize the governing equations. The equations governing the processes inside different layers of an SOFC are based on conservative principle; the discretization scheme commonly used for problems involving conservative laws is a well known method, often referred to as finite volume method or control volume method [83–85]. The discretized governing equations form a system of algebraic equations, whose solution can be obtained using a direct or indirect method. For the present problem, which is highly non-linear involving interdependent variables with multi-component mixture of species, an iterative solution method is used to obtain the solution of the discretized governing equations.

The overall solution methodology used to solve the governing equations is outlined in this chapter. In the beginning, the numerical scheme used to discretize the governing equations is briefly described. Then, the discretized governing equations obtained from the application of numerical scheme are presented. Finally, the solution procedure used to obtain the numerical solution is discussed. It should be noted that the asterisk operator, $(*)$, representing dimensionless variables is omitted from the governing equations presented in this chapter.

5.1 Finite Volume Method

The first step in the finite volume method is to divide the computational domain into a number of non-overlapping control volumes such that there is one control volume enclosing each grid point. The sample grid used for the present SOFC model and its portion used for the discretization scheme are shown in Figure 5.1. Although the grid is continuous, it can be divided into 5 distinct regions corresponding to different layers of an SOFC. The grid is uniform locally but non-uniform globally, which means the mesh size is uniform within each layer or component of the computational domain. Finer mesh sizes are required in the reaction zone layers than in the backing layers to capture the electrochemical reactions and other processes.

The second key step of the finite volume method is the integration of governing equations over each control volume and the variation of a variable between the grid points is expressed in terms of piecewise profiles to evaluate the integral. The resulting equation is a discretization equation expressed in terms of the values of a variable for a group of grid points [83]. The application of finite volume method to fuel cell and other related problems has been recognized by various researchers [37, 86–88].

A portion of the computational grid in two-dimensions (x-y) is also illustrated in Figure 5.1. Although the grid shown is two-dimensional, but the value of a variable (ψ) at the coordinates (i, j, k), P, depends on its east (E), west (W), north (N), south (S), front (F), and back (B) neighbors. In the same manner, the faces of a control volume are denoted as east (e), west (w), north (n), south (s), front (f) and back (b). The discretization equation for a variable (ψ), in general, can be expressed as

$$A_P\psi_P = A_E\psi_E + A_W\psi_W + A_N\psi_N + A_S\psi_S + A_F\psi_F + A_B\psi_B + S_\psi \tag{5.1}$$

where A_E, A_W, A_N, A_S, A_F, and A_B are neighbor coefficients of a control volume, P, A_P is the center-point coefficient, which is the sum of all neighbor coefficients, and S_ψ is the term representing the source term within the control volume, P.

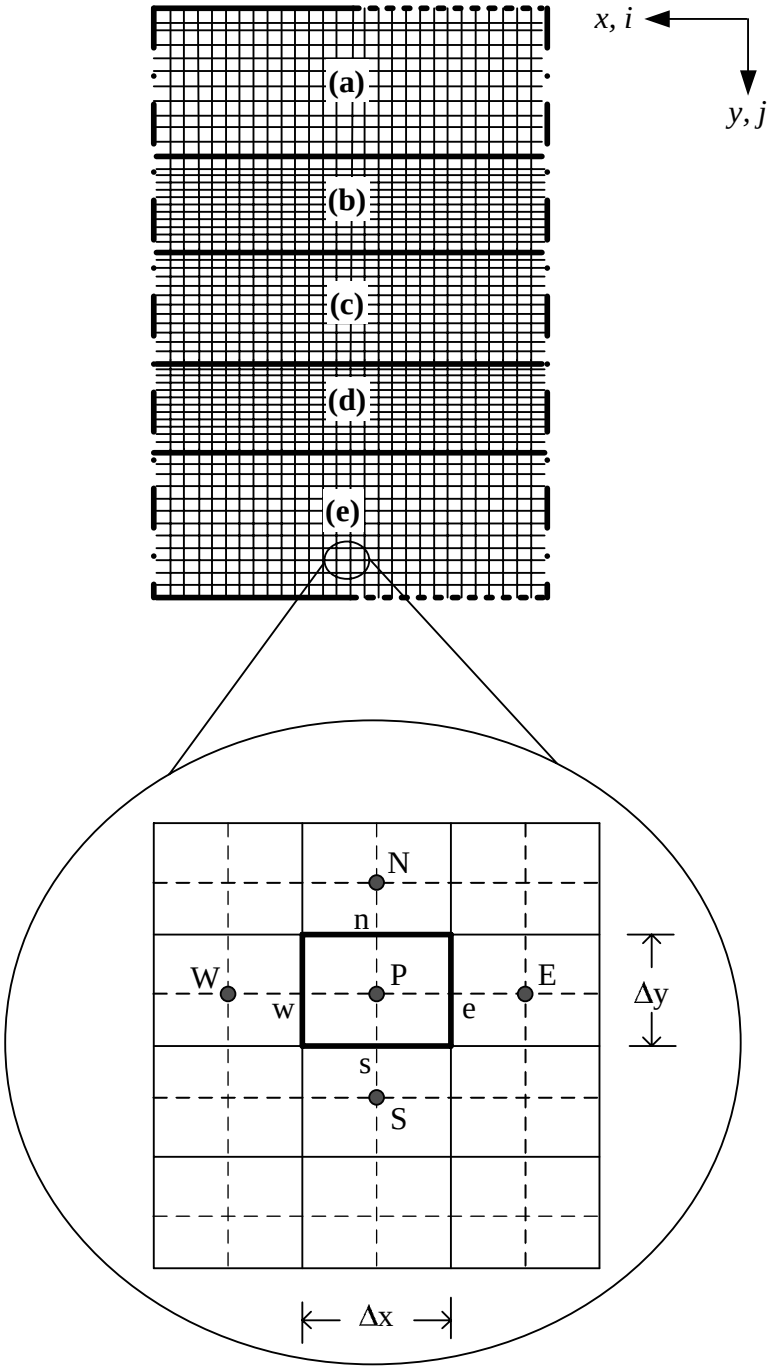

Figure 5.1: The sample grid used for the present SOFC model. The grid is uniform and consists of 5 distinct regions: (a) anode backing layer, (b) anode reaction zone layer, (c) electrolyte layer, (d) cathode reaction zone layer, and (e) cathode backing layer. Note that the figure is not to scale.

5.2 Discretized Governing Equations

The finite volume method discussed above is applied to the governing equations presented in the previous chapter. The resulting discretized equations are presented in the following sections.

5.2.1 Conservation of Species

The conservation of species equation for methane (labeled as 1) in the backing as well as reaction zone layers can be expressed as

$$\begin{aligned}
&\frac{\partial}{\partial x}\left\{-\left(\Gamma_{11}\frac{\partial x_1}{\partial x}+\Gamma_{12}\frac{\partial x_2}{\partial x}+\Gamma_{13}\frac{\partial x_3}{\partial x}+\Gamma_{14}\frac{\partial x_4}{\partial x}\right)\right\} \quad + \\
&\frac{\partial}{\partial y}\left\{-\left(\Gamma_{11}\frac{\partial x_1}{\partial y}+\Gamma_{12}\frac{\partial x_2}{\partial y}+\Gamma_{13}\frac{\partial x_3}{\partial y}+\Gamma_{14}\frac{\partial x_4}{\partial y}\right)\right\} \quad + \\
&\frac{\partial}{\partial z}\left\{-\left(\Gamma_{11}\frac{\partial x_1}{\partial z}+\Gamma_{12}\frac{\partial x_2}{\partial z}+\Gamma_{13}\frac{\partial x_3}{\partial z}+\Gamma_{14}\frac{\partial x_4}{\partial z}\right)\right\} \quad - \\
&\qquad\qquad \dot{S}_{s,1}=0
\end{aligned} \tag{5.2}$$

where the subscripts 1,2,3, and 4 refer to methane, hydrogen, carbon monoxide, and carbon dioxide, respectively; Γ_{11}, Γ_{12}, Γ_{13}, and Γ_{14} are the elements of the inverted modified Stefan-Maxwell matrix, which can be treated as diffusion coefficients in the numerical formulation. It is to be noted that the elements of the inverted modified Stefan-Matrix matrix are not constants but are functions of mole fractions of the species, molecular and Knudsen diffusivities of species, which are in turn functions of design and operating conditions.

Integrating Equation (5.2) over the control volume, ΔV ($\Delta x\ \Delta y\ \Delta z$), results in the following equation

$$\begin{aligned}
&\left[\left(\Gamma_{11}\frac{\partial x_1}{\partial x}\right)_e - \left(\Gamma_{11}\frac{\partial x_1}{\partial x}\right)_w\right]\Delta y\Delta z + \left[\left(\Gamma_{12}\frac{\partial x_2}{\partial x}\right)_e - \left(\Gamma_{12}\frac{\partial x_2}{\partial x}\right)_w\right]\Delta y\Delta z \quad + \\
&\left[\left(\Gamma_{13}\frac{\partial x_3}{\partial x}\right)_e - \left(\Gamma_{13}\frac{\partial x_3}{\partial x}\right)_w\right]\Delta y\Delta z + \left[\left(\Gamma_{14}\frac{\partial x_4}{\partial x}\right)_e - \left(\Gamma_{14}\frac{\partial x_4}{\partial x}\right)_w\right]\Delta y\Delta z \quad + \\
&\left[\left(\Gamma_{11}\frac{\partial x_1}{\partial y}\right)_n - \left(\Gamma_{11}\frac{\partial x_1}{\partial y}\right)_s\right]\Delta x\Delta z + \left[\left(\Gamma_{12}\frac{\partial x_2}{\partial y}\right)_n - \left(\Gamma_{12}\frac{\partial x_2}{\partial y}\right)_s\right]\Delta x\Delta z \quad + \\
&\left[\left(\Gamma_{13}\frac{\partial x_3}{\partial y}\right)_n - \left(\Gamma_{13}\frac{\partial x_3}{\partial y}\right)_s\right]\Delta x\Delta z + \left[\left(\Gamma_{14}\frac{\partial x_4}{\partial y}\right)_n - \left(\Gamma_{14}\frac{\partial x_4}{\partial y}\right)_s\right]\Delta x\Delta z \quad + \\
&\left[\left(\Gamma_{11}\frac{\partial x_1}{\partial z}\right)_f - \left(\Gamma_{11}\frac{\partial x_1}{\partial z}\right)_b\right]\Delta x\Delta y + \left[\left(\Gamma_{12}\frac{\partial x_2}{\partial z}\right)_f - \left(\Gamma_{12}\frac{\partial x_2}{\partial z}\right)_b\right]\Delta x\Delta y \quad + \\
&\left[\left(\Gamma_{13}\frac{\partial x_3}{\partial z}\right)_f - \left(\Gamma_{13}\frac{\partial x_3}{\partial z}\right)_b\right]\Delta x\Delta y + \left[\left(\Gamma_{14}\frac{\partial x_4}{\partial z}\right)_f - \left(\Gamma_{14}\frac{\partial x_4}{\partial z}\right)_b\right]\Delta x\Delta y \quad + \\
&\qquad\qquad \dot{S}_{s,1}\Delta x\Delta y\Delta z = 0
\end{aligned} \tag{5.3}$$

In order to obtain the useful forms of discretized equations, the so-called diffusion coefficients (Γ) and the gradients of the unknown variables at the faces (e, w, n, s, f, b) of the control volume are required. For an uniform grid, the diffusion coefficients at the faces are determined as [85]:

$$(\Gamma)_e = \frac{\Gamma_E + \Gamma_P}{2} \tag{5.4}$$

$$(\Gamma)_w = \frac{\Gamma_P + \Gamma_W}{2} \tag{5.5}$$

$$(\Gamma)_n = \frac{\Gamma_N + \Gamma_P}{2} \tag{5.6}$$

$$(\Gamma)_s = \frac{\Gamma_P + \Gamma_S}{2} \tag{5.7}$$

$$(\Gamma)_f = \frac{\Gamma_F + \Gamma_P}{2} \tag{5.8}$$

$$(\Gamma)_b = \frac{\Gamma_P + \Gamma_B}{2} \tag{5.9}$$

The gradients at the faces are evaluated as

$$\left(\frac{\partial x_i}{\partial x}\right)_e = \left(\frac{x_i|_E - x_i|_P}{\Delta x}\right) \tag{5.10}$$

$$\left(\frac{\partial x_i}{\partial x}\right)_w = \left(\frac{x_i|_P - x_i|_W}{\Delta x}\right) \tag{5.11}$$

$$\left(\frac{\partial x_i}{\partial y}\right)_n = \left(\frac{x_i|_N - x_i|_P}{\Delta y}\right) \tag{5.12}$$

$$\left(\frac{\partial x_i}{\partial y}\right)_s = \left(\frac{x_i|_P - x_i|_S}{\Delta y}\right) \tag{5.13}$$

$$\left(\frac{\partial x_i}{\partial z}\right)_f = \left(\frac{x_i|_F - x_i|_P}{\Delta z}\right) \tag{5.14}$$

$$\left(\frac{\partial x_i}{\partial z}\right)_b = \left(\frac{x_i|_P - x_i|_B}{\Delta z}\right) \tag{5.15}$$

Substituting the above definitions of diffusion coefficients and gradients of the unknown variables at the faces of the CV in Equation (5.3), we obtained the discretized equation for species 1 (methane), which can be expressed as

$$A_P^{x_1} x_1|_P = A_E^{x_1} x_1|_E + A_W^{x_1} x_1|_W + A_N^{x_1} x_1|_N + A_S^{x_1} x_1|_S + A_F^{x_1} x_1|_F + A_B^{x_1} x_1|_B + B_P^{x_1} \tag{5.16}$$

where the coefficients are defined as

$$A_E^{x_1} = \left(\frac{\Gamma_{11}|_e}{\Delta x}\right) \Delta y \Delta z \tag{5.17}$$

$$A_W^{x_1} = \left(\frac{\Gamma_{11}|_w}{\Delta x}\right) \Delta y \Delta z \tag{5.18}$$

$$A_N^{x_1} = \left(\frac{\Gamma_{11}|_n}{\Delta y}\right) \Delta x \Delta z \tag{5.19}$$

$$A_S^{x_1} = \left(\frac{\Gamma_{11}|_n}{\Delta y}\right) \Delta x \Delta z \tag{5.20}$$

$$A_F^{x_1} = \left(\frac{\Gamma_{11}|_f}{\Delta z}\right) \Delta x \Delta y \tag{5.21}$$

$$A_B^{x_1} = \left(\frac{\Gamma_{11}|_b}{\Delta z}\right) \Delta x \Delta y \tag{5.22}$$

$$A_P^{x_1} = A_E^{x_1} + A_W^{x_1} + A_N^{x_1} + A_S^{x_1} + A_F^{x_1} + A_B^{x_1} \tag{5.23}$$

$$
\begin{aligned}
B_P^{x_1} &= \dot{S}_{s,1}\Delta x\Delta y\Delta z + \left(\frac{\Gamma_{12}|_e\Delta y\Delta z}{\Delta x}\right)x_2|_E + \left(\frac{\Gamma_{12}|_w\Delta y\Delta z}{\Delta x}\right)x_2|_W + \left(\frac{\Gamma_{12}|_n\Delta x\Delta z}{\Delta y}\right)x_2|_N \\
&+ \left(\frac{\Gamma_{12}|_s\Delta x\Delta z}{\Delta y}\right)x_2|_S + \left(\frac{\Gamma_{12}|_f\Delta x\Delta y}{\Delta z}\right)x_2|_F + \left(\frac{\Gamma_{12}|_b\Delta x\Delta y}{\Delta z}\right)x_2|_B \\
&+ \left(\frac{\Gamma_{13}|_e\Delta y\Delta z}{\Delta x}\right)x_3|_E + \left(\frac{\Gamma_{13}|_w\Delta y\Delta z}{\Delta x}\right)x_3|_W + \left(\frac{\Gamma_{13}|_n\Delta x\Delta z}{\Delta y}\right)x_3|_N \\
&+ \left(\frac{\Gamma_{13}|_s\Delta x\Delta z}{\Delta y}\right)x_3|_S + \left(\frac{\Gamma_{13}|_f\Delta x\Delta y}{\Delta z}\right)x_3|_F + \left(\frac{\Gamma_{13}|_b\Delta x\Delta y}{\Delta z}\right)x_3|_B \\
&+ \left(\frac{\Gamma_{14}|_e\Delta y\Delta z}{\Delta x}\right)x_4|_E + \left(\frac{\Gamma_{14}|_w\Delta y\Delta z}{\Delta x}\right)x_4|_W + \left(\frac{\Gamma_{14}|_n\Delta x\Delta z}{\Delta y}\right)x_4|_N \\
&+ \left(\frac{\Gamma_{14}|_s\Delta x\Delta z}{\Delta y}\right)x_4|_S + \left(\frac{\Gamma_{14}|_f\Delta x\Delta y}{\Delta z}\right)x_4|_F + \left(\frac{\Gamma_{14}|_b\Delta x\Delta y}{\Delta z}\right)x_4|_B \qquad (5.24)
\end{aligned}
$$

Similarly, the discretized governing equations for the other species can be written as

$$A_P^{x_2}x_2|_P = A_E^{x_2}x_2|_E + A_W^{x_2}x_2|_W + A_N^{x_2}x_2|_N + A_S^{x_2}x_2|_S + A_F^{x_2}x_2|_F + A_B^{x_2}x_2|_B + B_P^{x_2} \qquad (5.25)$$

$$A_P^{x_3}x_3|_P = A_E^{x_3}x_3|_E + A_W^{x_3}x_3|_W + A_N^{x_3}x_3|_N + A_S^{x_3}x_3|_S + A_F^{x_3}x_3|_F + A_B^{x_3}x_3|_B + B_P^{x_3} \qquad (5.26)$$

$$A_P^{x_4}x_4|_P = A_E^{x_4}x_4|_E + A_W^{x_4}x_4|_W + A_N^{x_4}x_4|_N + A_S^{x_4}x_4|_S + A_F^{x_4}x_4|_F + A_B^{x_4}x_4|_B + B_P^{x_4} \qquad (5.27)$$

where the coefficients A and B are defined in the similar manner as expressed in Equations (5.17-5.24).

The mole fraction of the last species (water vapor or species 5) is obtained from the fact that the sum of mole fractions of all species at P is equal to unity, expressed as

$$x_5|_P = 1 - x_1|_P - x_2|_P - x_3|_P - x_4|_P \qquad (5.28)$$

5.2.2 Conservation of Electronic Charge

Consider the general conservation equation for the electronic charge in the backing and reaction zone layers as

$$\frac{\partial^2\phi_e}{\partial x^2} + \frac{\partial^2\phi_e}{\partial y^2} + \frac{\partial^2\phi_e}{\partial z^2} = \mp\dot{S}_{e^-} \qquad (5.29)$$

Integrating the above equation over the control volume, ΔV ($\Delta x\ \Delta y\ \Delta z$), we obtain

$$\left[\left(\frac{\partial \phi_e}{\partial x}\right)_e - \left(\frac{\partial \phi_e}{\partial x}\right)_w\right]\Delta y\Delta z + \left[\left(\frac{\partial \phi_e}{\partial y}\right)_n - \left(\frac{\partial \phi_e}{\partial y}\right)_s\right]\Delta x\Delta z \quad + \\ \left[\left(\frac{\partial \phi_e}{\partial z}\right)_f - \left(\frac{\partial \phi_e}{\partial z}\right)_b\right]\Delta x\Delta y \pm \dot{S}_{e^-}\Delta x\Delta y\Delta z = 0 \tag{5.30}$$

The gradients of the electronic potential at the faces (e, w, n, s, f, b) of the control volume are evaluated similar to the gradients of mole fractions, we obtain the general discretized equation for the electronic potential which can be expressed as

$$A_P^{\phi_e}\phi_e|_P = A_E^{\phi_e}\phi_e|_E + A_W^{\phi_e}\phi_e|_W + A_N^{\phi_e}\phi_e|_N + A_S^{\phi_e}\phi_e|_S + A_F^{\phi_e}\phi_e|_F + A_B^{\phi_e}\phi_e|_B + B_P^{\phi_e} \tag{5.31}$$

where the coefficients are defined as

$$A_E^{\phi_e} = \left(\frac{\Delta y\Delta z}{\Delta x}\right) \tag{5.32}$$

$$A_W^{\phi_e} = \left(\frac{\Delta y\Delta z}{\Delta x}\right) \tag{5.33}$$

$$A_N^{\phi_e} = \left(\frac{\Delta x\Delta z}{\Delta y}\right) \tag{5.34}$$

$$A_S^{\phi_e} = \left(\frac{\Delta x\Delta z}{\Delta y}\right) \tag{5.35}$$

$$A_F^{\phi_e} = \left(\frac{\Delta x\Delta y}{\Delta z}\right) \tag{5.36}$$

$$A_B^{\phi_e} = \left(\frac{\Delta x\Delta y}{\Delta z}\right) \tag{5.37}$$

$$A_P^{\phi_e} = A_E^{\phi_e} + A_W^{\phi_e} + A_N^{\phi_e} + A_S^{\phi_e} + A_F^{\phi_e} + A_B^{\phi_e} \tag{5.38}$$

$$B_P^{\phi_e} = \pm\dot{S}_{e^-}\Delta x\Delta y\Delta z \tag{5.39}$$

5.2.3 Conservation of Ionic Charge

The general conservation equation for the ionic charge in the reaction zone can be written as

$$\frac{\partial^2 \phi_i}{\partial x^2} + \frac{\partial^2 \phi_i}{\partial y^2} + \frac{\partial^2 \phi_i}{\partial z^2} = \pm \dot{S}_{O^{2-}} \tag{5.40}$$

Again, integrating the above equation over the control volume ΔV ($\Delta x\ \Delta y\ \Delta z$), we get

$$\begin{aligned}\left[\left(\frac{\partial \phi_i}{\partial x}\right)_e - \left(\frac{\partial \phi_i}{\partial x}\right)_w\right] \Delta y \Delta z + \left[\left(\frac{\partial \phi_i}{\partial y}\right)_n - \left(\frac{\partial \phi_i}{\partial y}\right)_s\right] \Delta x \Delta z \quad + \\ \left[\left(\frac{\partial \phi_i}{\partial z}\right)_f - \left(\frac{\partial \phi_i}{\partial z}\right)_b\right] \Delta x \Delta y \mp \dot{S}_{O^{2-}} \Delta x \Delta y \Delta z = 0\end{aligned} \tag{5.41}$$

In order to obtain the discretized governing equation for the ionic charge, the gradients of the ionic potential at the faces of the control volume are evaluated in the same manner as the gradients of the mole fractions presented in Equations (5.10-5.15). The discretized governing equation for the ionic potential can be expressed as

$$A_P^{\phi_i} \phi_i|_P = A_E^{\phi_i} \phi_i|_E + A_W^{\phi_i} \phi_i|_W + A_N^{\phi_i} \phi_i|_N + A_S^{\phi_i} \phi_i|_S + A_F^{\phi_i} \phi_i|_F + A_B^{\phi_i} \phi_i|_B + B_P^{\phi_i} \tag{5.42}$$

where the coefficients, $A_P^{\phi_i}$, $A_E^{\phi_i}$, $A_W^{\phi_i}$, $A_N^{\phi_i}$, $A_S^{\phi_i}$, $A_F^{\phi_i}$, and $A_B^{\phi_i}$, are similar to the coefficients, $A_P^{\phi_e}$, $A_E^{\phi_e}$, $A_W^{\phi_e}$, $A_N^{\phi_e}$, $A_S^{\phi_e}$, $A_F^{\phi_e}$, and $A_B^{\phi_e}$, and are given in Equations (5.32-5.38). The coefficient $B_P^{\phi_i}$ is defined as

$$B_P^{\phi_i} = \pm \dot{S}_{O^{2-}} \Delta x \Delta y \Delta z \tag{5.43}$$

The discretized equation for the ionic potential given by Equation (5.42) is also valid for the electrolyte layer, where the coefficient B is set as zero, since there is no consumption or production of ionic charge in the electrolyte layer.

5.2.4 Conservation of Energy

The general conservation of energy equation in the backing and reaction zone layers can be expressed as

$$\frac{\partial^2 T}{\partial x^2}+\frac{\partial^2 T}{\partial y^2}+\frac{\partial^2 T}{\partial z^2}-\left(\sum_{i=1}^{n} c_{pi}N_{ix}\right)\frac{\partial T}{\partial x}-\left(\sum_{i=1}^{n} c_{pi}N_{iy}\right)\frac{\partial T}{\partial y}-\left(\sum_{i=1}^{n} c_{pi}N_{iz}\right)\frac{\partial T}{\partial z}+\dot{S}_e=0 \quad (5.44)$$

Integrating the above equation over the control volume, ΔV ($\Delta x\ \Delta y\ \Delta z$), results in

$$\begin{aligned}\left[\left(\frac{\partial T}{\partial x}\right)_e-\left(\frac{\partial T}{\partial x}\right)_w\right]\Delta y\Delta z+\left[\left(\frac{\partial T}{\partial y}\right)_n-\left(\frac{\partial T}{\partial y}\right)_s\right]\Delta x\Delta z+\left[\left(\frac{\partial T}{\partial z}\right)_f-\left(\frac{\partial T}{\partial z}\right)_b\right]\Delta x\Delta y\\ -\left(\sum_{i=1}^{n} c_{pi}\left[(N_{ix}T)_e-(N_{ix}T)_e\right]\right)\Delta y\Delta z-\left(\sum_{i=1}^{n} c_{pi}\left[(N_{iy}T)_n-(N_{iy}T)_s\right]\right)\Delta x\Delta z\\ -\left(\sum_{i=1}^{n} c_{pi}\left[(N_{iz}T)_f-(N_{iz}T)_b\right]\right)\Delta x\Delta y+\dot{S}_e\Delta x\Delta y\Delta z=0 \quad (5.45)\end{aligned}$$

The gradients of temperature at the faces of the control volume are evaluated similar to the gradients of the mole fractions given in Equations (5.10-5.15), and the scalar quantity, temperature, at the faces are evaluated as

$$(\mathcal{F}_{ix}T)_e=T|_P\max(\mathcal{F}_{ix}|_e,0)-T|_E\max(-\mathcal{F}_{ix}|_e,0) \quad (5.46)$$

$$(\mathcal{F}_{ix}T)_w=T|_W\max(\mathcal{F}_{ix}|_w,0)-T|_P\max(-\mathcal{F}_{ix}|_w,0) \quad (5.47)$$

$$(\mathcal{F}_{iy}T)_n=T|_P\max(\mathcal{F}_{iy}|_n,0)-T|_N\max(-\mathcal{F}_{iy}|_n,0) \quad (5.48)$$

$$(\mathcal{F}_{iy}T)_s=T|_S\max(\mathcal{F}_{ix}|_s,0)-T|_P\max(-\mathcal{F}_{iy}|_s,0) \quad (5.49)$$

$$(\mathcal{F}_{iz}T)_f=T|_P\max(\mathcal{F}_{iz}|_f,0)-T|_F\max(-\mathcal{F}_{iz}|_f,0) \quad (5.50)$$

$$(\mathcal{F}_{iz}T)_b=T|_B\max(\mathcal{F}_{iz}|_b,0)-T|_P\max(-\mathcal{F}_{iz}|_b,0) \quad (5.51)$$

where $\mathcal{F}_{ix}$, $\mathcal{F}_{iy}$, and $\mathcal{F}_{iz}$ are defined as

$$\mathcal{F}_{ix} = N_{ix}\Delta y\Delta z \tag{5.52}$$

$$\mathcal{F}_{iy} = N_{iy}\Delta x\Delta z \tag{5.53}$$

$$\mathcal{F}_{iz} = N_{iz}\Delta x\Delta y \tag{5.54}$$

Substituting the above definitions in Equation (5.45), we obtain the general discretized energy equation as

$$A_P^T T|_P = A_E^T T|_E + A_W^T T|_W + A_N^T T|_N + A_S^T T|_S + A_F^T T|_F + A_B^T T|_B + B_P^T \tag{5.55}$$

where the coefficients are defined as

$$A_E^T = \left(\frac{\Delta y\Delta z}{\Delta x}\right) + \sum_{i=1}^{n}\left[c_{pi}\max\left(-\mathcal{F}_{ix}|_e, 0\right)\right] \tag{5.56}$$

$$A_W^T = \left(\frac{\Delta y\Delta z}{\Delta x}\right) + \sum_{i=1}^{n}\left[c_{pi}\max\left(\mathcal{F}_{ix}|_w, 0\right)\right] \tag{5.57}$$

$$A_N^T = \left(\frac{\Delta x\Delta z}{\Delta y}\right) + \sum_{i=1}^{n}\left[c_{pi}\max\left(-\mathcal{F}_{iy}|_n, 0\right)\right] \tag{5.58}$$

$$A_S^T = \left(\frac{\Delta x\Delta z}{\Delta y}\right) + \sum_{i=1}^{n}\left[c_{pi}\max\left(\mathcal{F}_{iy}|_s, 0\right)\right] \tag{5.59}$$

$$A_F^T = \left(\frac{\Delta x\Delta y}{\Delta z}\right) + \sum_{i=1}^{n}\left[c_{pi}\max\left(-\mathcal{F}_{iz}|_f, 0\right)\right] \tag{5.60}$$

$$A_B^T = \left(\frac{\Delta x\Delta y}{\Delta z}\right) + \sum_{i=1}^{n}\left[c_{pi}\max\left(\mathcal{F}_{iz}|_b, 0\right)\right] \tag{5.61}$$

$$A_P^T = A_E^T + A_W^T + A_N^T + A_S^T + A_F^T + A_B^T \tag{5.62}$$

$$B_P^T = \dot{S}_e\Delta x\Delta y\Delta z \tag{5.63}$$

5.2.5 Boundary Conditions

The boundary conditions in the present model can be broadly classified into three categories: specified boundary conditions, continuous flux boundary conditions and insulated boundary conditions. Specified boundary conditions are external boundary conditions, where mole fractions of species and electronic potential are specified at the boundary control volumes. When the values of the variables are specified at the boundary control volumes, no additional equations are required.

However, when the values of the variables are not known, then there is a need to construct additional equations for the variables at the boundary control volumes. For instance, at the interface between the backing layers and reaction zone layers, the continuous flux boundary conditions exist, where the molar flux of species, electronic current density and heat flux are continuous. Mathematically, the boundary conditions at the interface between the backing and reaction zone layers can be written as

$$\left.\begin{aligned} \overrightarrow{N}_i \cdot \overrightarrow{n}|_{\mathrm{bl}} &= \overrightarrow{N}_i \cdot \overrightarrow{n}|_{\mathrm{rl}} \\ \overrightarrow{J}_e \cdot \overrightarrow{n}|_{\mathrm{bl}} &= \overrightarrow{J}_e \cdot \overrightarrow{n}|_{\mathrm{rl}} \\ \overrightarrow{q} \cdot \overrightarrow{n}|_{\mathrm{bl}} &= \overrightarrow{q} \cdot \overrightarrow{n}|_{\mathrm{rl}} \end{aligned}\right\} \tag{5.64}$$

Using the above boundary conditions, the conditions required for the derivation of additional equations are obtained as

$$\begin{aligned} \text{Species 1}: \left(\Gamma_{11}\frac{\partial x_1}{\partial x}\right)|_I = \left(\gamma_{11}\frac{\partial x_1}{\partial x}\right)|_I + \left(\gamma_{12}\frac{\partial x_2}{\partial x}\right)|_I + \left(\gamma_{13}\frac{\partial x_3}{\partial x}\right)|_I + \left(\gamma_{14}\frac{\partial x_1}{\partial x}\right)|_I \\ - \left(\Gamma_{12}\frac{\partial x_2}{\partial x}\right)|_I - \left(\Gamma_{13}\frac{\partial x_3}{\partial x}\right)|_I - \left(\Gamma_{14}\frac{\partial x_4}{\partial x}\right)|_I \end{aligned} \tag{5.65}$$

$$\text{Electronic Charge}: \left(\sigma_{\mathrm{bl}}^{\mathrm{eff}}\frac{\partial \phi_e}{\partial x}\right)|_I = \left(\sigma_{\mathrm{rl}}^{\mathrm{eff}}\frac{\partial \phi_e}{\partial x}\right)|_I \tag{5.66}$$

$$\text{Temperature}: \left(k_{\mathrm{bl}}^{\mathrm{eff}}\frac{\partial T}{\partial x}\right)|_I = \left(k_{\mathrm{rl}}^{\mathrm{eff}}\frac{\partial T}{\partial x}\right)|_I \tag{5.67}$$

where the subscript "I" refers to the interface between the backing and reaction zone layers, Γ and γ are the elements of the inverted modified Stefan-Maxwell matrix of the backing and reaction zone layers, respectively.

Integrating the respective governing equations over the boundary control volume, and substituting the above conditions at the interface, we obtain the following discretized equations

$$\text{Species 1}: \; (A_P^{x_1} x_1|_P)_I = (A_E^{x_1} x_1|_E)_I + (A_W^{x_1} x_1|_W)_I + (A_N^{x_1} x_1|_N)_I + (A_S^{x_1} x_1|_S)_I + (A_F^{x_1} x_1|_F)_I + (A_B^{x_1} x_1|_B)_I + (B_P^{x_1})_I \tag{5.68}$$

where the coefficients are defined as

$$(A_E^{x_1})_I = \left(\frac{\gamma_{11}|_I}{\Delta x_{\text{rl}}}\right) \Delta y \Delta z \tag{5.69}$$

$$(A_W^{x_1})_I = \left(\frac{\Gamma_{11}|_w}{\Delta x}\right) \Delta y \Delta z \tag{5.70}$$

$$(A_N^{x_1})_I = \left(\frac{\Gamma_{11}|_n}{\Delta y}\right) \Delta x \Delta z \tag{5.71}$$

$$(A_S^{x_1})_I = \left(\frac{\Gamma_{11}|_n}{\Delta y}\right) \Delta x \Delta z \tag{5.72}$$

$$(A_F^{x_1})_I = \left(\frac{\Gamma_{11}|_f}{\Delta z}\right) \Delta x \Delta y \tag{5.73}$$

$$(A_B^{x_1})_I = \left(\frac{\Gamma_{11}|_b}{\Delta z}\right) \Delta x \Delta y \tag{5.74}$$

$$(A_P^{x_1})_I = (A_E^{x_1})_I + (A_W^{x_1})_I + (A_N^{x_1})_I + (A_S^{x_1})_I + (A_F^{x_1})_I + (A_B^{x_1})_I \tag{5.75}$$

$$
\begin{aligned}
(B_P^{x_1})_I &= \dot{S}_{s,1}\Delta x\Delta y\Delta z + \left(\frac{\gamma_{12}|_I\Delta y\Delta z}{\Delta x_{\mathrm{rl}}}\right)(x_2|_E)_I + \left(\frac{\Gamma_{12}|_w\Delta y\Delta z}{\Delta x}\right)(x_2|_W)_I \\
&+ \left(\frac{\Gamma_{12}|_n\Delta x\Delta z}{\Delta y}\right)(x_2|_N)_I + \left(\frac{\Gamma_{12}|_s\Delta x\Delta z}{\Delta y}\right)(x_2|_S)_I + \left(\frac{\Gamma_{12}|_f\Delta x\Delta y}{\Delta z}\right)(x_2|_F)_I \\
&+ \left(\frac{\Gamma_{12}|_b\Delta x\Delta y}{\Delta z}\right)(x_2|_B)_I + \left(\frac{\gamma_{13}|_I\Delta y\Delta z}{\Delta x_{\mathrm{rl}}}\right)(x_3|_E)_I + \left(\frac{\Gamma_{13}|_w\Delta y\Delta z}{\Delta x}\right)(x_3|_W)_I \\
&+ \left(\frac{\Gamma_{13}|_n\Delta x\Delta z}{\Delta y}\right)(x_3|_N)_I + \left(\frac{\Gamma_{13}|_s\Delta x\Delta z}{\Delta y}\right)(x_3|_S)_I + \left(\frac{\Gamma_{13}|_f\Delta x\Delta y}{\Delta z}\right)(x_3|_F)_I \\
&+ \left(\frac{\Gamma_{13}|_b\Delta x\Delta y}{\Delta z}\right)(x_3|_B)_I + \left(\frac{\Gamma_{14}|_e\Delta y\Delta z}{\Delta x_{\mathrm{rl}}}\right)(x_4|_E)_I + \left(\frac{\Gamma_{14}|_w\Delta y\Delta z}{\Delta x}\right)(x_4|_W)_I \\
&+ \left(\frac{\Gamma_{14}|_n\Delta x\Delta z}{\Delta y}\right)(x_4|_N)_I + \left(\frac{\Gamma_{14}|_s\Delta x\Delta z}{\Delta y}\right)(x_4|_S)_I + \left(\frac{\Gamma_{14}|_f\Delta x\Delta y}{\Delta z}\right)(x_4|_F)_I \\
&+ \left(\frac{\Gamma_{14}|_b\Delta x\Delta y}{\Delta z}\right)(x_4|_B)_I \qquad (5.76)
\end{aligned}
$$

where Δx_{rl} is the thickness of the grid in the reaction zone layers in the x-direction.

$$
\begin{aligned}
\text{Electronic Charge}: \left(A_P^{\phi_e}\phi_e|_P\right)_I &= \left(A_E^{\phi_e}\phi_e|_E\right)_I + \left(A_W^{\phi_e}\phi_e|_W\right)_I + \left(A_N^{\phi_e}\phi_e|_N\right)_I + \left(A_S^{\phi_e}\phi_e|_S\right)_I \\
&+ \left(A_F^{\phi_e}\phi_e|_F\right)_I + \left(A_B^{\phi_e}\phi_e|_B\right)_I + \left(B_P^{\phi_e}\right)_I \qquad (5.77)
\end{aligned}
$$

where the coefficients are defined as

$$\left(A_E^{\phi_e}\right)_I = \left(\frac{\sigma_{\mathrm{rl}}^{\mathrm{eff}}}{\sigma_{\mathrm{bl}}^{\mathrm{eff}}}\right)\left(\frac{\Delta y\Delta z}{\Delta x_{\mathrm{rl}}}\right) \qquad (5.78)$$

$$\left(A_W^{\phi_e}\right)_I = \left(\frac{\Delta y\Delta z}{\Delta x}\right) \qquad (5.79)$$

$$\left(A_N^{\phi_e}\right)_I = \left(\frac{\Delta x\Delta z}{\Delta y}\right) \qquad (5.80)$$

$$\left(A_S^{\phi_e}\right)_I = \left(\frac{\Delta x\Delta z}{\Delta y}\right) \qquad (5.81)$$

$$\left(A_F^{\phi_e}\right)_I = \left(\frac{\Delta x\Delta y}{\Delta z}\right) \qquad (5.82)$$

$$\left(A_B^{\phi_e}\right)_I = \left(\frac{\Delta x\Delta y}{\Delta z}\right) \qquad (5.83)$$

$$\left(A_P^{\phi_e}\right)_I = \left(A_E^{\phi_e}\right)_I + \left(A_W^{\phi_e}\right)_I + \left(A_N^{\phi_e}\right)_I + \left(A_S^{\phi_e}\right)_I + \left(A_F^{\phi_e}\right)_I + \left(A_B^{\phi_e}\right)_I \qquad (5.84)$$

$$\left(B_P^{\phi_e}\right)_I = 0 \tag{5.85}$$

$$\begin{aligned}\text{Energy}: \left(A_P^T T|_P\right)_I &= \left(A_E^T T|_E\right)_I + \left(A_W^T T|_W\right)_I + \left(A_N^T T|_N\right)_I + \left(A_S^T T|_S\right)_I \\ &+ \left(A_F^T T|_F\right)_I + \left(A_B^T T|_B\right)_I + \left(B_P^T\right)_I \end{aligned} \tag{5.86}$$

where the coefficients are defined as

$$\left(A_E^T\right)_I = \left(\frac{k_{\text{rl}}^{\text{eff}}}{k_{\text{bl}}^{\text{eff}}}\right)\left(\frac{\Delta y \Delta z}{\Delta x_{\text{rl}}}\right) + \sum_{i=1}^{n}\left[c_{pi}\max\left(-\mathcal{F}_{ix}|_I, 0\right)\right] \tag{5.87}$$

$$\left(A_W^T\right)_I = \left(\frac{\Delta y \Delta z}{\Delta x}\right) + \sum_{i=1}^{n}\left[c_{pi}\max\left(\mathcal{F}_{ix}|_w, 0\right)\right] \tag{5.88}$$

$$\left(A_N^T\right)_I = \left(\frac{\Delta x \Delta z}{\Delta y}\right) + \sum_{i=1}^{n}\left[c_{pi}\max\left(-\mathcal{F}_{iy}|_n, 0\right)\right] \tag{5.89}$$

$$\left(A_S^T\right)_I = \left(\frac{\Delta x \Delta z}{\Delta y}\right) + \sum_{i=1}^{n}\left[c_{pi}\max\left(\mathcal{F}_{iy}|_s, 0\right)\right] \tag{5.90}$$

$$\left(A_F^T\right)_I = \left(\frac{\Delta x \Delta y}{\Delta z}\right) + \sum_{i=1}^{n}\left[c_{pi}\max\left(-\mathcal{F}_{iz}|_f, 0\right)\right] \tag{5.91}$$

$$\left(A_B^T\right)_I = \left(\frac{\Delta x \Delta y}{\Delta z}\right) + \sum_{i=1}^{n}\left[c_{pi}\max\left(\mathcal{F}_{iz}|_b, 0\right)\right] \tag{5.92}$$

$$\left(A_P^T\right)_I = \left(A_E^T\right)_I + \left(A_W^T\right)_I + \left(A_N^T\right)_I + \left(A_S^T\right)_I + \left(A_F^T\right)_I + \left(A_B^T\right)_I \tag{5.93}$$

$$\left(B_P^T\right)_I = \dot{S}_e \Delta x \Delta y \Delta z \tag{5.94}$$

On the other hand, most of the external boundaries are insulated boundaries, where the mass flux of species, electronic current density, ionic current density, and heat flux are zero. Mathemat-

ically, the respective boundary conditions can be expressed as

$$\left.\begin{array}{l} \overrightarrow{N}_i \cdot \overrightarrow{n} = 0 \\ \overrightarrow{J}_e \cdot \overrightarrow{n} = 0 \\ \overrightarrow{J}_i \cdot \overrightarrow{n} = 0 \\ \overrightarrow{q} \cdot \overrightarrow{n} = 0 \end{array}\right\} \tag{5.95}$$

Again, using the above expressions, the conditions required for obtaining the additional equations are derived as

$$\text{Species 1}: \left(\Gamma_{11}\frac{\partial x_1}{\partial y}\right)|_{EB} = -\left(\Gamma_{12}\frac{\partial x_2}{\partial y}\right)|_{EB} - \left(\Gamma_{13}\frac{\partial x_3}{\partial y}\right)|_{EB} - \left(\Gamma_{14}\frac{\partial x_4}{\partial y}\right)|_{EB} \tag{5.96}$$

$$\text{Electronic Charge}: \left(\frac{\partial \phi_e}{\partial y}\right)|_{EB} = 0 \tag{5.97}$$

$$\text{Ionic Charge}: \left(\frac{\partial \phi_i}{\partial y}\right)|_{EB} = 0 \tag{5.98}$$

$$\text{Temperature}: \left(\frac{\partial T}{\partial y}\right)|_{EB} = 0 \tag{5.99}$$

where the subscript "EB" refers to the external boundaries of the computational domain. Similar expressions can be used for insulated boundaries in the other directions of the computational domain.

Integrating the respective governing equations over the boundary control volume, and substituting the above conditions, we obtained the following discretized equations:

$$\begin{aligned} \text{Species 1}: (A_P^{x_1} x_1|_P)_{EB} &= (A_E^{x_1} x_1|_E)_{EB} + (A_W^{x_1} x_1|_W)_{EB} + (A_N^{x_1} x_1|_N)_{EB} \\ &\quad + (A_F^{x_1} x_1|_F)_{EB} + (A_B^{x_1} x_1|_B)_{EB} + (B_P^{x_1})_{EB} \end{aligned} \tag{5.100}$$

where the coefficients are defined as

$$(A_E^{x_1})_{EB} = \left(\frac{\Gamma_{11}|_e}{\Delta x}\right)\Delta y \Delta z \tag{5.101}$$

$$(A_W^{x_1})_{EB} = \left(\frac{\Gamma_{11}|_w}{\Delta x}\right)\Delta y\Delta z \tag{5.102}$$

$$(A_N^{x_1})_{EB} = \left(\frac{\Gamma_{11}|_n}{\Delta y}\right)\Delta x\Delta z \tag{5.103}$$

$$(A_F^{x_1})_{EB} = \left(\frac{\Gamma_{11}|_f}{\Delta z}\right)\Delta x\Delta y \tag{5.104}$$

$$(A_B^{x_1})_{EB} = \left(\frac{\Gamma_{11}|_b}{\Delta z}\right)\Delta x\Delta y \tag{5.105}$$

$$(A_P^{x_1})_{EB} = (A_E^{x_1})_{EB} + (A_W^{x_1})_{EB} + (A_N^{x_1})_{EB} + (A_F^{x_1})_{EB} + (A_B^{x_1})_{EB} \tag{5.106}$$

$$\begin{aligned}(B_P^{x_1})_{EB} &= \dot{S}_{s,1}\Delta x\Delta y\Delta z + \left(\frac{\Gamma_{12}|_e\Delta y\Delta z}{\Delta x}\right)(x_2|_E)_{EB} + \left(\frac{\Gamma_{12}|_w\Delta y\Delta z}{\Delta x}\right)(x_2|_W)_{EB} \\ &+ \left(\frac{\Gamma_{12}|_n\Delta x\Delta z}{\Delta y}\right)(x_2|_N)_{EB} + \left(\frac{\Gamma_{12}|_f\Delta x\Delta y}{\Delta z}\right)(x_2|_F)_{EB} + \left(\frac{\Gamma_{12}|_b\Delta x\Delta y}{\Delta z}\right)(x_2|_B)_{EB} \\ &+ \left(\frac{\Gamma_{13}|_e\Delta y\Delta z}{\Delta x}\right)(x_3|_E)_{EB} + \left(\frac{\Gamma_{13}|_w\Delta y\Delta z}{\Delta x}\right)(x_3|_W)_{EB} + \left(\frac{\Gamma_{13}|_n\Delta x\Delta z}{\Delta y}\right)(x_3|_N)_{EB} \\ &+ \left(\frac{\Gamma_{13}|_f\Delta x\Delta y}{\Delta z}\right)(x_3|_F)_{EB} + \left(\frac{\Gamma_{13}|_b\Delta x\Delta y}{\Delta z}\right)(x_3|_B)_{EB} + \left(\frac{\Gamma_{14}|_e\Delta y\Delta z}{\Delta x}\right)(x_4|_E)_{EB} \\ &+ \left(\frac{\Gamma_{14}|_w\Delta y\Delta z}{\Delta x}\right)(x_4|_W)_{EB} + \left(\frac{\Gamma_{14}|_n\Delta x\Delta z}{\Delta y}\right)(x_4|_N)_{EB} + \left(\frac{\Gamma_{14}|_f\Delta x\Delta y}{\Delta z}\right)(x_4|_F)_{EB} \\ &+ \left(\frac{\Gamma_{14}|_b\Delta x\Delta y}{\Delta z}\right)(x_4|_B)_{EB}\end{aligned} \tag{5.107}$$

$$\begin{aligned}\text{Electronic Charge}: \left(A_P^{\phi_e}\phi_e|_P\right)_{EB} &= \left(A_E^{\phi_e}\phi_e|_E\right)_{EB} + \left(A_W^{\phi_e}\phi_e|_W\right)_{EB} + \left(A_N^{\phi_e}\phi_e|_N\right)_{EB} \\ &+ \left(A_F^{\phi_e}\phi_e|_F\right)_{EB} + \left(A_B^{\phi_e}\phi_e|_B\right)_{EB} + \left(B_P^{\phi_e}\right)_{EB}\end{aligned} \tag{5.108}$$

where the coefficients are defined as

$$\left(A_E^{\phi_e}\right)_{EB} = \left(\frac{\Delta y\Delta z}{\Delta x}\right) \tag{5.109}$$

$$\left(A_W^{\phi_e}\right)_{EB} = \left(\frac{\Delta y\Delta z}{\Delta x}\right) \tag{5.110}$$

$$\left(A_N^{\phi_e}\right)_{EB} = \left(\frac{\Delta x\Delta z}{\Delta y}\right) \tag{5.111}$$

$$\left(A_F^{\phi_e}\right)_{EB} = \left(\frac{\Delta x \Delta y}{\Delta z}\right) \tag{5.112}$$

$$\left(A_B^{\phi_e}\right)_{EB} = \left(\frac{\Delta x \Delta y}{\Delta z}\right) \tag{5.113}$$

$$\left(A_P^{\phi_e}\right)_{EB} = \left(A_E^{\phi_e}\right)_{EB} + \left(A_W^{\phi_e}\right)_{EB} + \left(A_N^{\phi_e}\right)_{EB} + \left(A_F^{\phi_e}\right)_{EB} + \left(A_B^{\phi_e}\right)_{EB} \tag{5.114}$$

$$\left(B_P^{\phi_e}\right)_{EB} = \dot{S}_{e-} \Delta x \Delta y \Delta z \tag{5.115}$$

$$\begin{aligned} \text{Ionic Charge}: \left(A_P^{\phi_i}\phi_i|_P\right)_{EB} &= \left(A_E^{\phi_i}\phi_i|_E\right)_{EB} + \left(A_W^{\phi_i}\phi_i|_W\right)_{EB} + \left(A_N^{\phi_i}\phi_i|_N\right)_{EB} \\ &\quad + \left(A_F^{\phi_i}\phi_i|_F\right)_{EB} + \left(A_B^{\phi_i}\phi_i|_B\right)_{EB} + \left(B_P^{\phi_i}\right)_{EB} \end{aligned} \tag{5.116}$$

where the coefficients are defined as

$$\left(A_E^{\phi_i}\right)_{EB} = \left(\frac{\Delta y \Delta z}{\Delta x}\right) \tag{5.117}$$

$$\left(A_W^{\phi_i}\right)_{EB} = \left(\frac{\Delta y \Delta z}{\Delta x}\right) \tag{5.118}$$

$$\left(A_N^{\phi_i}\right)_{EB} = \left(\frac{\Delta x \Delta z}{\Delta y}\right) \tag{5.119}$$

$$\left(A_F^{\phi_i}\right)_{EB} = \left(\frac{\Delta x \Delta y}{\Delta z}\right) \tag{5.120}$$

$$\left(A_B^{\phi_i}\right)_{EB} = \left(\frac{\Delta x \Delta y}{\Delta z}\right) \tag{5.121}$$

$$\left(A_P^{\phi_i}\right)_{EB} = \left(A_E^{\phi_i}\right)_{EB} + \left(A_W^{\phi_i}\right)_{EB} + \left(A_N^{\phi_i}\right)_{EB} + \left(A_F^{\phi_i}\right)_{EB} + \left(A_B^{\phi_i}\right)_{EB} \tag{5.122}$$

$$\left(B_P^{\phi_i}\right)_{EB} = \dot{S}_{O^{2-}} \Delta x \Delta y \Delta z \tag{5.123}$$

$$\begin{aligned} \text{Energy}: \left(A_P^T T|_P\right)_{EB} &= \left(A_E^T T|_E\right)_{EB} + \left(A_W^T T|_W\right)_{EB} + \left(A_N^T T|_N\right)_{EB} \\ &\quad + \left(A_F^T T|_F\right)_{EB} + \left(A_B^T T|_B\right)_{EB} + \left(B_P^T\right)_{EB} \end{aligned} \tag{5.124}$$

where the coefficients are defined as

$$\left(A_E^T\right)_{EB} = \left(\frac{\Delta y \Delta z}{\Delta x}\right) + \sum_{i=1}^{n} \left[c_{pi} \max\left(-\mathcal{F}_{ix}|_e, 0\right)\right] \tag{5.125}$$

$$\left(A_W^T\right)_{EB} = \left(\frac{\Delta y \Delta z}{\Delta x}\right) + \sum_{i=1}^{n} \left[c_{pi} \max\left(\mathcal{F}_{ix}|_w, 0\right)\right] \tag{5.126}$$

$$\left(A_N^T\right)_{EB} = \left(\frac{\Delta x \Delta z}{\Delta y}\right) + \sum_{i=1}^{n} \left[c_{pi} \max\left(-\mathcal{F}_{iy}|_n, 0\right)\right] \tag{5.127}$$

$$\left(A_F^T\right)_{EB} = \left(\frac{\Delta x \Delta y}{\Delta z}\right) + \sum_{i=1}^{n} \left[c_{pi} \max\left(-\mathcal{F}_{iz}|_f, 0\right)\right] \tag{5.128}$$

$$\left(A_B^T\right)_{EB} = \left(\frac{\Delta x \Delta y}{\Delta z}\right) + \sum_{i=1}^{n} \left[c_{pi} \max\left(\mathcal{F}_{iz}|_b, 0\right)\right] \tag{5.129}$$

$$\left(A_P^T\right)_{EB} = \left(A_E^T\right)_{EB} + \left(A_W^T\right)_{EB} + \left(A_N^T\right)_{EB} + \left(A_F^T\right)_{EB} + \left(A_B^T\right)_{EB} \tag{5.130}$$

$$\left(B_P^T\right)_{EB} = \dot{S}_e \Delta x \Delta y \Delta z \tag{5.131}$$

5.3 Solution Procedure

The discretized governing equations presented in the previous section form a system of algebraic equations having the following general form for a single control volume

$$A_P \psi_P = A_E \psi_E + A_W \psi_W + A_N \psi_N + A_S \psi_S + A_F \psi_F + A_B \psi_B + B_P \tag{5.132}$$

where the coefficients A and B are functions of design and operating parameters, and (or) grid spacing.

The solution for the system of algebraic equations can be obtained using direct or iterative method. For the present problem where the equations are coupled, an iterative method based on Guass-Seidel is used to solve the system of algebraic equations. The solution procedure is illustrated in Figure 5.2. The first step of the solution procedure involves determining the coefficients of the discretized governing equations. The procedure for calculating the coefficients is illustrated in

Figure 5.3.

Once coefficients of the discretized governing equations are determined, the next step is to calculate the updated values of species, electronic and ionic potentials and temperature at the unknown grid locations. The last step in the solution procedure is to calculate the residual and check it with the convergence criteria in order to decide whether the solution converges or not. The residual of a variable is calculated as

$$R_{es}^{\psi} = A_E^{\psi}\psi_E + A_W^{\psi}\psi_W + A_N^{\psi}\psi_N + A_S^{\psi}\psi_S + A_F^{\psi}\psi_F + A_B^{\psi}\psi_B + B_P^{\psi} - A_P^{\psi}\psi_P \tag{5.133}$$

The summation of the residual is taken over all the control volumes for different variables, and the error is taken as the residual of the equations for the mole fraction of the species, electronic and ionic potentials or temperature:

$$\text{error} = \left(\sum_{\mathrm{i,j,k}} \mathrm{R}_{\mathrm{es}}^{\mathrm{x_i}},\ \sum_{\mathrm{i,j,k}} \mathrm{R}_{\mathrm{es}}^{\phi_{\mathrm{e}}},\ \sum_{\mathrm{i,j,k}} \mathrm{R}_{\mathrm{es}}^{\phi_{\mathrm{i}}},\ \sum_{\mathrm{i,j,k}} \mathrm{R}_{\mathrm{es}}^{\mathrm{T}} \right) \tag{5.134}$$

The solution is considered to be converged when the above error satisfies the convergence criteria in the range of 10^{-5} and 10^{-7}. It is worth mentioning that grid sensitivity tests are performed to ensure grid independent solution. For instance, in a cross-sectional domain of the cell, beyond grid size of 30×120, no significant change has been observed in the distribution of interdependent fields in different layers of the cell.

5.4 Summary

The governing equations presented in the previous chapter are discretized using the finite volume method. Since the resulting discretized algebraic equations are non-linear, an iterative solver is used to obtain the solution. The coefficients of the discretized equations are calculated as an initial step of the solution. The conservation of species along with the modified Stefan-Maxwell equations are solved to obtain the distributions of species mole fractions in the anode and cathode layers. Then, the conservation of electronic charge is solved to obtain the distribution of electronic potential

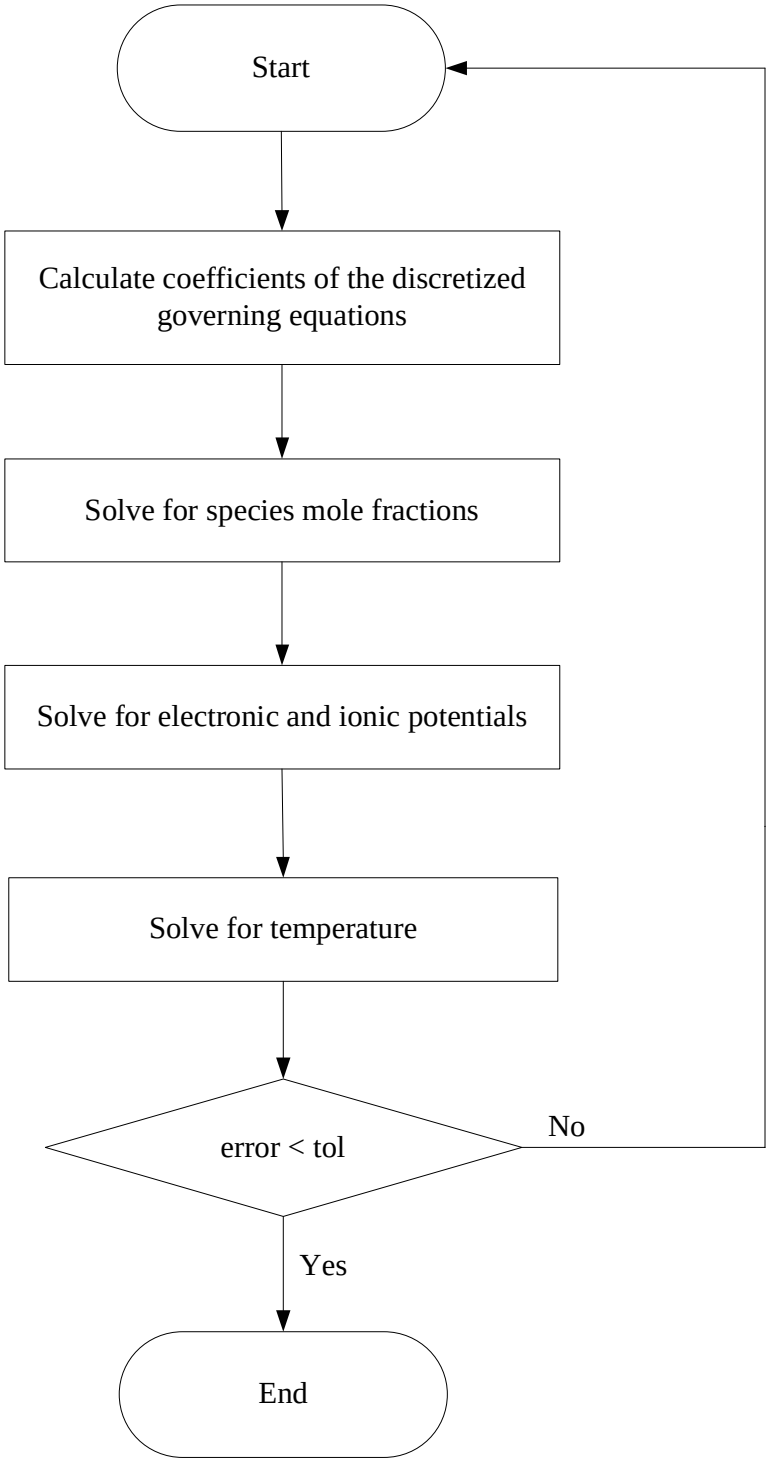

Figure 5.2: The solution procedure.

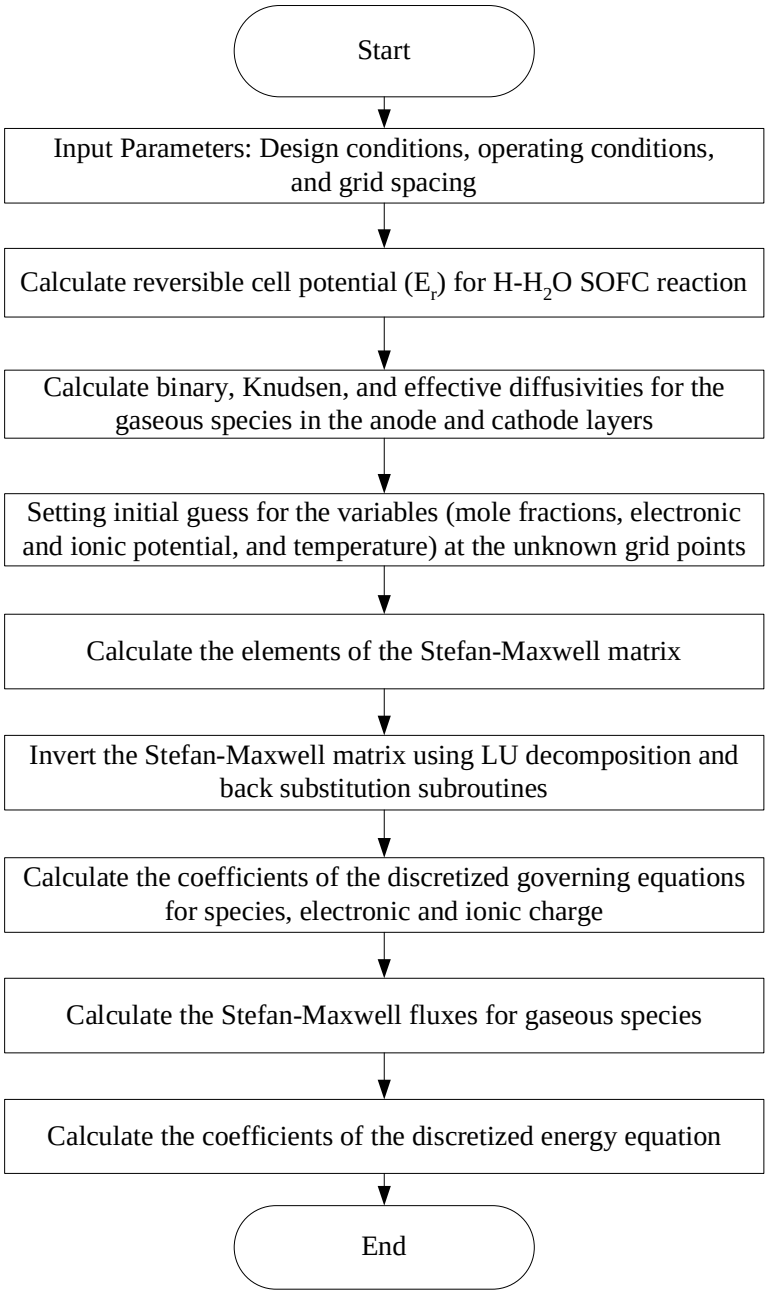

Figure 5.3: The procedure for calculating coefficients of the discretized equations.

in the backing as well as reaction zone layers, while the conservation of ionic charge is solved to obtain the distribution of ionic potential in the reaction zone and electrolyte layers. Finally, the conservation of energy is solved to obtain the temperature distribution inside the cell.

The coefficients of the discretized governing equations and values of the variables at the unknown grid points are updated after each iteration. The residuals of the variables and the solution error are calculated to determine the convergence of the solution.

Chapter 6

Results and Discussion

This chapter presents the results obtained from numerical implementation of the mathematical model presented in the previous chapter. The chapter is divided into different sections. First, validation of the model is presented in section 6.1. Then, section 6.2 presents the verification of modeling an electrode as two distinct layers. Next, the predicted performance of anode-supported and self-supported SOFCs are presented in section 6.3. Then, the results obtained from a parametric study is presented in section 6.4, which examines the effect of various key operating and design parameters on the performance of an anode-supported SOFC. Finally, the predicted phenomena in different layers of an anode-supported SOFC are presented in section 6.5.

6.1 Validation

In order to determine the range of validity and accuracy of the model, the developed model needs to be validated. In this section, validation of the mathematical model is presented with measured data sets available in the literature.

6.1.1 Measured Cell Performance

The parameters used in predicting the cell performance are listed in Table 6.1. The predicted cell performance is compared with measured data published in the literature [90], and is shown

in Figure 6.1. The performance of the cell is predicted when the cell is supplied with 95% H_2 and 5% H_2O as fuel, operating at a temperature and pressure of 1073 K and 1 atm, respectively. Oxygen composition in the ambient air is used as an oxidant. It can be seen that the predicted cell performance is in excellent agreement with measured data. It is worth mentioning that all the parameters used in the model validation are obtained from Rogers et al. [90] except the parameters given with references. Since the value of tortuosity reported by Rogers et al. [90] is unity, the value of tortuosity is varied to obtain the best agreement between the present model prediction and measured results shown in Figure 6.1. The typical tortuosity value for SOFC electrodes is in the range of 2-6 [19, 91]. Hence, the tortuosity value of 2.75 used in the present model prediction is in the typical range for SOFC electrodes and provides the best agreement with experimental results published in the literature. The coefficient of determination (R^2 value), an indicator between 0 and 1, reveals how closely the predicted values correspond to the measured data, is calculated for the present model as 0.988.

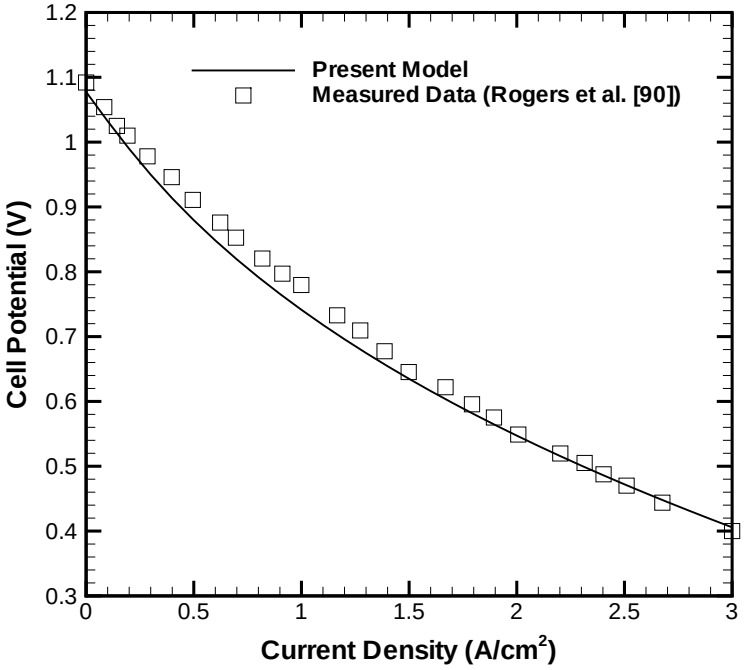

Figure 6.1: Validation with measured cell performance.

Table 6.1: Parameters used in the validation of measured cell performance.

Operating temperature, T_{op}	1073.0 K
Total pressure, p	1.0 atm
Fuel composition, x_{H_2}; x_{H_2O}	0.95; 0.05
Air composition, x_{O_2}; x_{N_2}	0.21; 0.79
Anode conductivity, σ,	71428.57 S/m
Cathode conductivity, σ,	5376.34 S/m
Electrolyte conductivity, κ,	0.64 S/m
Anode electrode layer thickness, t_{abl}	1000.0 μm
Cathode electrode layer thickness, t_{cbl}	50.0 μm
Anode reaction zone layer thickness, t_{arl}	20.0 μm
Cathode reaction zone layer thickness, t_{crl}	20.0 μm
Electrolyte thickness, t_{el}	10.0 μm
Porosity of anode and cathode, ε	0.375
Tortuosity of anode and cathode, τ	2.75 [20]
Pore diameter of anode and cathode, d_p	1.5 μm [9]
Contact angle between electron- and ion-conducting particles, θ	15^o [29]
Radius of electron-conducting particles, r_{el}	0.1 μm [20,32]
Radius of ion-conducting particles, r_{io}	0.1 μm [20,32]
Volume fraction of electron-conducting particles , Φ	0.5 [29,33]
Reference H_2 concentration, c_{H_2}	10.78 mole/m^3
Reference O_2 concentration, c_{O_2}	2.38 mole/m^3
Reference exchange current density for H_2 oxidation, $J_{0,ref}^{H_2}$	1320 A/m^2 [9]
Reference exchange current density for O_2 reduction, $J_{0,ref}^{O_2}$	400 A/m^2 [29]
Reaction order for H_2 oxidation, γ_{H_2}	0.5
Reaction order for O_2 reduction, γ_{O_2}	0.5

Source: Rogers et al. [90].

6.1.2 Measured Concentration Overpotential

The parameters used in predicting the concentration overpotential are listed in Table 6.2. Most of the parameters are obtained from Yakabe et al. [14], who reported measured data for concentration overpotential for a ternary mixture. The thickness of the anode is reported to be 2 mm, of which 50 μm is treated as the thickness of the anode reaction zone layer, which is in accordance with the thickness of the reaction zone layer reported by Lehnert et al. [18] for an anode thickness of 2 mm. Further, the present model requires micro parameters of the electrodes, whose typical values are obtained from published literature and are listed in Table 6.2 with references.

Figure 6.2 shows the comparison between the model prediction and measured data at 0.7 A/cm^2.

Table 6.2: Parameters used in the validation of measured concentration overpotential.

Operating temperature, T_{op}	1023.0 K
Total pressure, p	1.0 atm
Reference fuel composition, x_{H_2}; x_{H_2O}	0.8; 0.2
Anode backing layer thickness, t_{abl}	1950.0 μm
Anode reaction zone layer thickness, t_{arl}	50.0 μm [18]
Resistivity of electron-conducting particles, ρ_{el},	$2.98 \times 10^{-5} \exp\left(-\frac{1332}{T}\right)$ Ωm [39]
Resistivity of ion-conducting particles, ρ_{io},	$2.94 \times 10^{-5} \exp\left(\frac{10350}{T}\right)$ Ωm [39]
Porosity , ε	0.46
Tortuosity , τ	4.5
Pore diameter, d_p	2.6 μm
Contact angle between electron- and ion-conducting particles, θ	15^o [29]
Radius of electron-conducting particles, r_{el}	0.1 μm [20, 32]
Radius of ion-conducting particles, r_{io}	0.1 μm [20, 32]
Volume fraction of electron-conducting particles , Φ	0.5 [20, 33]
Reference H_2 concentration, c_{H_2}	10.78 mole/m^3
Reference exchange current density for H_2 oxidation, $J_{0,ref}^{H_2}$	1320 A/m^2 [9]
Reaction order for H_2 oxidation, γ_{H_2}	0.5

Source: Yakabe et al. [14].

The abscissa of Figure 6.2 represents the variation in reactant concentration, while the ordinate represents the difference between the actual and reference concentration overpotential. The reference concentration overpotential was measured when there was no argon in the system at hydrogen mole fraction equal to 0.8. Argon was added to the system to vary the reactant concentration such that the ratio of mole fractions of hydrogen and water vapor is 4:1. It can be seen from the figure that with the increase of reactant concentration, the concentration overpotential difference decreases. Increasing the reactant concentration at the inlet increases the concentration of the reactant at the reactant sites, which in turn reduces the concentration overpotential. Further, it can be seen that the concentration overpotential difference predicted by the present model is in excellent agreement with measured data published in the literature. The coefficient of determination (R^2 value) is obtained as 0.989.

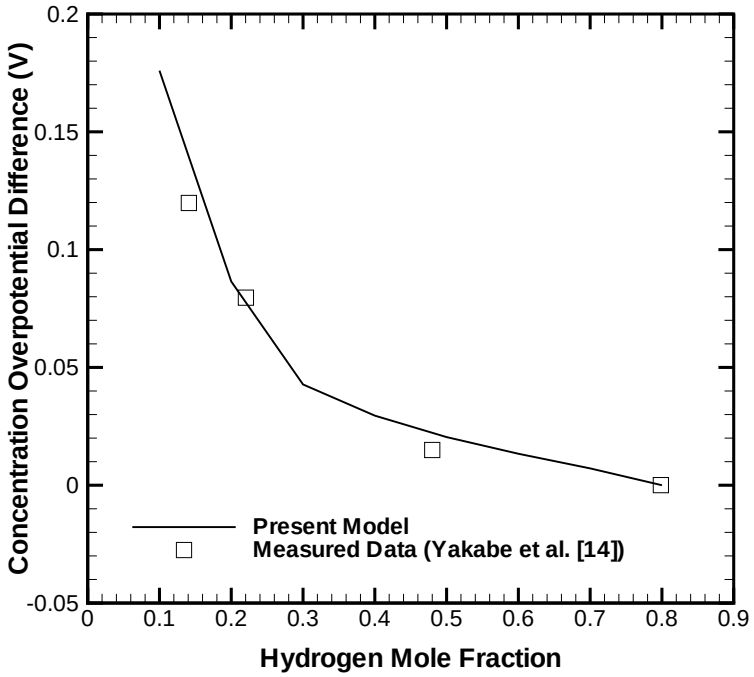

Figure 6.2: Validation with measured concentration overpotential.

6.2 Verification of Modeling an Electrode as Two Distinct Layers

As stated before, one of the novel features of the present SOFC model is its treatment of electrodes. An electrode in the present model is composed of two distinct layers referred to as the backing layer and the reaction zone layer. To verify this distinction of an electrode in the present model, a 2-D simulation has been conducted wherein an electrode is considered as a porous structure of electron- and ion-conducting particles. In other words, an electrode is treated as a reaction zone layer having triple phase boundaries (TPBs) scattered throughout the electrode, consistent with the micro modeling approach of treating electrodes.

The fuel composition and the parameters used in the verification of electrode modeling are listed in Tables 6.3 and 6.4, respectively. Most of electrode parameters used in the simulation are typical values reported in the open literature. The operating temperature and pressure are set as 1073 K and 1 atm, respectively.

Table 6.3: Fuel composition used in the present simulation, which is identical to Lehnert et al. [18].

Species	Mole fraction
CH_4	0.171
H_2	0.263
H_2O	0.493
CO	0.029
CO_2	0.044

Figure 6.3 shows the distributions of dimensionless electronic and ionic current densities along the centerline of an anode at 0.5 A/cm^2. Moreover, similar results have been obtained for electronic and ionic current densities along the top and bottom of an anode, and the values are tabulated in Table 6.5. The solid line in Figure 6.3 represents the electronic current density while the dashed

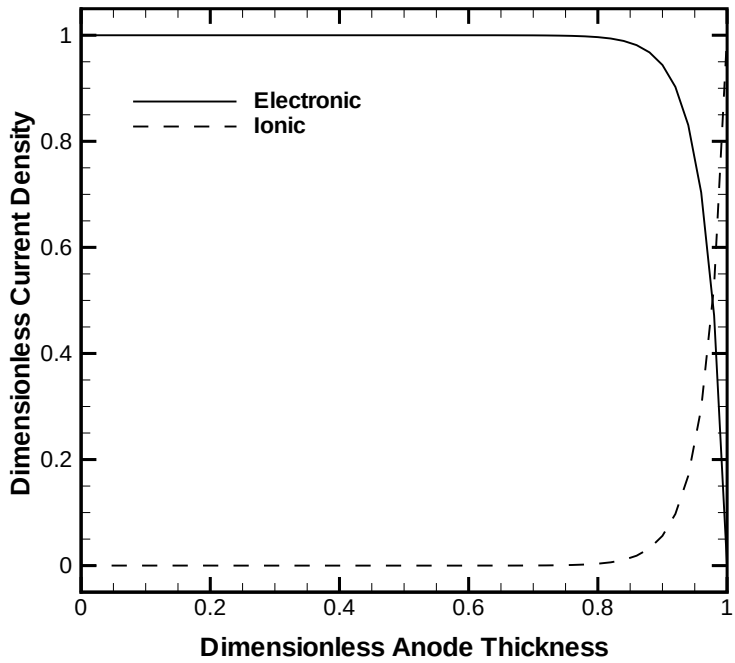

Figure 6.3: Distributions of dimensionless ionic and electronic current densities along the centerline of an SOFC anode.

line represents the ionic current density. It can be seen that electronic current density decreases and ionic current density increases along the thickness of the anode. This is due to the transfer of charge

Table 6.4: Parameters used in the verification of electrode modeling.

Operating temperature, T_{op}	1073.0 K
Total pressure, p	1.0 atm
Oxidant composition, x_{O_2}; x_{N_2}	0.21; 0.79
Anode thickness, t_{an}	150.0 μm
Electrolyte thickness, t_{el}	50.0 μm
Cathode thickness, t_{ca}	150.0 μm
Half-width of the channel interfacing backing layers, $w_{channel}$	1 $\times 10^{-3}$ m
Half-width of the interconnect interfacing backing layers, w_{int}	1 $\times 10^{-3}$ m
Resistivity of electron-conducting particles in anode, ρ_{el},	$2.98 \times 10^{-5} \exp\left(-\frac{1332}{T}\right)$ Ωm [39]
Resistivity of ion-conducting particles, ρ_{io},	$2.94 \times 10^{-5} \exp\left(\frac{10350}{T}\right)$ Ωm [39]
Resistivity of electron-conducting particles in cathode, ρ_{el}	$8.11 \times 10^{-5} \exp\left(\frac{600}{T}\right)$ Ωm [39]
Thermal conductivity of electron-conducting particles, k_{el}	3 W/mK [37]
Thermal conductivity of ion-conducting particles, k_{io}	2 W/mK [37]
Porosity, ε	0.3 [20]
Tortuosity, τ	4.5 [14, 19]
Pore diameter, d_p	1.0 μm [9]
Contact angle between electron- and ion-conducting particles, θ	15^o [29]
Radius of electron-conducting particles, r_{el}	0.1 μm [20, 32]
Radius of ion-conducting particles, r_{io}	0.1 μm [20, 32]
Volume fraction of electron-conducting particles, Φ	0.5 [20, 33]
Reference H_2 concentration, c_{H_2}	10.78 mole/m^3
Reference O_2 concentration, c_{O_2}	2.38 mole/m^3
Reference exchange current density for H_2 oxidation, $J_{0,ref}^{H_2}$	1320 A/m^2 [9]
Reference exchange current density for O_2 oxidation, $J_{0,ref}^{O_2}$	200 A/m^2 [29]
Reaction order for H_2 oxidation, γ_{H_2}	0.5
Reaction order for O_2 oxidation, γ_{O_2}	0.5

between the ion-conducting and electron-conducting particles of the anode. It can also be observed that electronic and ionic current densities remain constant for most of the thickness of the anode before exhibiting their variations at the end of the anode. Further, it can be seen that electronic current density reaches its minimum; whereas, ionic current density reaches its maximum at the end of the anode, indicating the interface between the anode and the electrolyte. It is worthwhile to note that identical distributions have been observed for electronic and ionic current densities in an anode at other current density values, such as 0.7 A/cm^2 and 1.0 A/cm^2. From the distributions of electronic and ionic current densities in the anode, we can deduce some important points. Firstly, since electronic and ionic current densities remains constant for most part of the anode before

Table 6.5: Values of dimensionless electronic and ionic current densities in an anode at different locations.

	Electronic Current Density			Ionic Current Density		
Anode Thickness	Top	Center	Bottom	Top	Center	Bottom
0	0.999993	0.999966	1	7.45E-6	3.40E-5	3.33E-7
0.1	0.999983	0.999942	0.999998	1.69E-5	5.75E-5	2.09E-6
0.2	0.999982	0.999955	0.999996	1.75E-5	4.51E-5	3.86E-6
0.3	0.999982	0.999964	0.999994	1.76E-5	3.63E-5	5.62E-6
0.4	0.999982	0.999969	0.999993	1.77E-5	3.09E-5	7.43E-6
0.5	0.999981	0.999972	0.999990	1.86E-5	2.80E-5	9.92E-6
0.6	0.999968	0.999961	0.999976	3.21E-5	3.87E-5	2.37E-5
0.7	0.999755	0.999751	0.999779	0.000244959	0.000248535	0.000220529
0.8	0.996406	0.996412	0.996611	0.00359385	0.00358784	0.00338863
0.9	0.943822	0.943879	0.945358	0.0561781	0.0561211	0.0546421
1.0	0	0	0	1	1	1

started to vary at the end of the anode, an anode (electrode) can be divided into two distinct layers referred to as the anode (electrode) backing layer and the anode (electrode) reaction zone layer. Secondly, the part of the anode where the electronic current density is unity and ionic current density is zero, which is referred to as the anode (electrode) backing layer, can be considered as an electron-conducting (ion insulator) layer. Lastly, the part of the anode exhibiting variation in the electronic and ionic current densities indicates the reactive sites where electrochemical reaction is most active, and can be treated as the reaction zone layer.

Although in the present simulation (micro-modeling approach), electrochemical reaction is considered throughout the anode but it is most effective within a distance of the order of tens of microns from the electrolyte. For instance, it can be seen from Figure 6.3 that the electronic and ionic current densities vary within dimensionless anode thickness of 0.2, which means for an anode thickness of 150 μm, the electrochemical reaction is most effective within a distance of 30 μm from the electrolyte. In other words, for an anode (electrode) thickness of 150 μm, a thickness of 30 μm from the electrolyte can be considered as the reaction zone layer. However, it should be noted that the thickness of 30 μm for an anode (electrode) thickness of 150 μm is not general, since it is obtained based on the operating and design conditions listed in Table 6.4. The point we are trying to prove here is that whether or not an electrode in an SOFC can be treated as two distinct layers.

From the present simulation, it can be concluded that the electrode in an SOFC can be treated as two distinct layers, referred to as the backing layer and the reaction zone layer for electrochemical reactions in the present model. This distinction is consistent with many studies reported in the open literature that the reactive sites are most active at the electrode/electrolyte interface and most of the electrochemical reactions occur within a distance of the order of tens of microns from the electrolyte [19, 20, 33, 66, 71]. The other important advantage of this distinction is the savings in computational time. For the same fuel composition and operating and design conditions, the computational time required for convergence is listed in Table 6.6. Using the present modeling approach of electrodes as two distinct layers, the computational time is reduced more than half of the time required for micro modeling approach. And because of high computational time, micro modeling approach is applied to single electrode (anode or cathode) models, and no one has applied to complete cell model; only recently, Nam and Jeon [36] integrated this approach to a cell level model, but the thicknesses of the electrodes were set as 50 μm. Therefore, the present modeling approach of treating electrodes as two distinct layers is computationally efficient which can be used for large-scale and stack modeling of SOFCs.

Table 6.6: Computational time for different approaches.

Approach	Time (s)
Micro modeling approach	7380
Present modeling approach	3120

6.3 Performance Prediction

As pointed out earlier, one of the purposes of developing SOFC model is to predict cell performance at different operating and design conditions. In order to predict the cell performance, various overpotentials have to be determined in different components of the cell. The developed model not only predicts the concentration overpotential in the electrodes but also predicts the activation and ohmic overpotentials. The predicted overpotentials in different components of the cell are then subtracted from the reversible cell potential to obtain the overall performance of the cell at specified

operating and design conditions.

The present section deals with performance prediction of two different designs of SOFCs, which can be classified either on their structure or operating temperatures. The conventional self-supported SOFCs are designed for operation between 1073 K and 1273 K, and are also known as high-temperature SOFCs. On the other hand, anode-supported SOFCs are suitable for operation between 823 K and 1073 K, and are also known as intermediate-temperature SOFCs [12]. The results obtained from 2-D model simulation of anode-supported and self-supported SOFCs are presented at the outset. Then, a comparison between the 2-D and 3-D model predictions of cell performance is presented for both anode-supported and self supported designs.

6.3.1 2-D Anode-Supported Model

Anode is the thickest component in an anode-supported SOFC on which all other layers are deposited. Moreover, an anode-supported SOFC is designed for operation in an intermediate temperature range (823-1073 K); therefore, it is also referred to as an intermediate-temperature SOFC.

The fuel composition and the base case parameters used in the simulation of an anode-supported SOFC are listed in Tables 6.3 and 6.7, respectively. The other design parameters are similar to the parameters used in the simulation for verification of modeling an electrode as two distinct layers, which are listed in Table 6.4. The predicted performance of an anode-supported SOFC resulting from the fuel composition and base case parameters listed in Tables 6.3 and 6.7 is shown in Figure 6.4.

Table 6.7: Base case parameters used in the simulation of an anode-supported SOFC.

Operating temperature, T_{op}	1073.0 K
Total pressure, p	1.0 atm
Oxidant composition, x_{O_2}; x_{N_2}	0.21; 0.79
Anode backing layer thickness, t_{abl}	1950.0 μm
Anode reaction zone layer thickness, t_{arl}	50.0 μm
Electrolyte thickness, t_{el}	20.0 μm
Cathode backing layer thickness, t_{cbl}	50.0 μm
Cathode reaction zone layer thickness, t_{crl}	10.0 μm

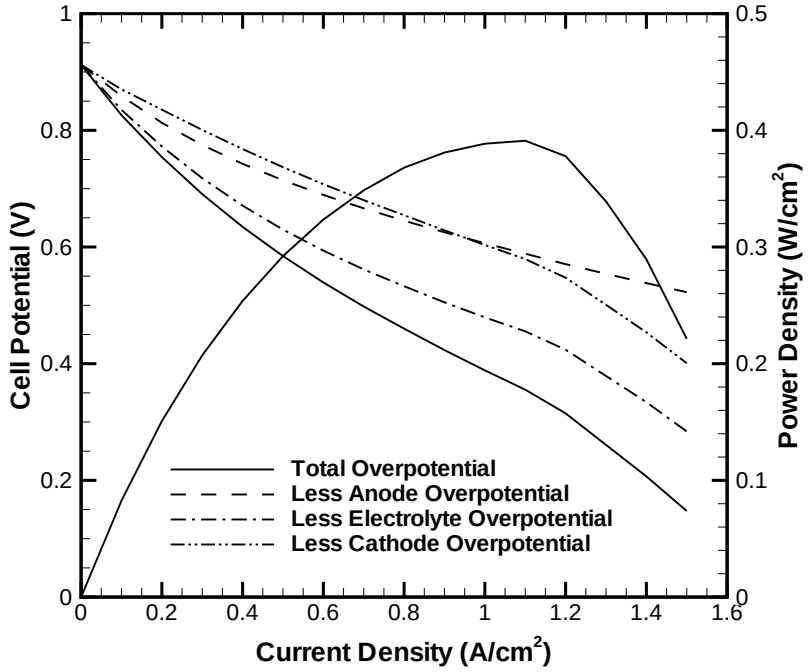

Figure 6.4: Base case performance of an anode-supported SOFC.

The x-axis of Figure 6.4 represents the current density (load), whereas the primary (left) and secondary (right) y-axes represent the cell potential and power density, respectively. The solid line corresponds to the cell potential and power density when all the overpotentials are subtracted from the reversible cell potential. The overpotentials include anode overpotential, cathode overpotential and electrolyte overpotential. Anode and cathode overpotentials include activation overpotentials due to the resistance to the charge transfer reactions, ohmic overpotentials due to the resistance to the flow of electrons and ions in the reaction zone layers and resistance to the flow of electrons in the backing layers, and concentration overpotentials due to the resistance to the flow of reactant species through void spaces. Conversely, the dashed lines correspond to the cell potential when anode overpotential, electrolyte overpotential, and cathode overpotential are not included in obtaining the polarization curves. It can be seen that the solid line representing the total overpotentials exhibits regions of activation and concentration overpotentials at low and high current densities,

respectively. Specifically, these regions of activation and concentration overpotentials are due to the cathode activation and anode concentration overpotentials, which is evident from the dashed lines neglecting the cathode and anode overpotentials, respectively. Additionally, it can be observed that the maximum power density obtained for an anode-supported SOFC using the fuel composition and base case parameters listed in Tables 6.3 and 6.7 is about 0.4 W/cm^2.

It can also be seen from Figure 6.4 that the profiles without anode and cathode overpotentials exhibit almost similar performances for current density upto 1 A/cm^2, indicating comparable magnitudes of anode and cathode overpotentials. However, at current densities beyond 1 A/cm^2, the profile without anode overpotential shows better performance. The reason for better performance at higher current densities is because of anode concentration overpotential, which is not included in the profile without anode overpotential. Further, it is observed that the cathode and electrolyte overpotentials are not negligible even though their thicknesses are negligible relative to the thickness of the anode in an anode-supported SOFC.

To better understand these observations, the anode overpotential at the base case conditions are further investigated, and a typical result is shown in Figure 6.5. It is clear that the ohmic overpotential is the single largest contributor to the overall anode overpotential, and the contribution of activation overpotential is negligible. Moreover, the concentration overpotential in the thick anode remains almost constant and close to zero for most of the current density range considered in the simulation before starting to increase beyond about 1.1 A/cm^2. The reason for anode concentration overpotential being negligible even in the thick anode is because of high reactant concentration due to chemical reactions (methane reforming and water-gas shift). For instance, methane reforming reaction produces three moles of H_2 for every mole of CH_4 consumed during the reaction; similarly, water-gas shit reaction produces a mole of H_2 for every mole of CO consumed during the reaction. A useful comparison of anode concentration overpotential with and without considering these chemical reactions is shown in Figure 6.6. The concentration overpotential in an anode-supported SOFC becomes significant when there are no chemical reactions in the anode and can be as high as 0.1 V at higher current densities. However, it is still three orders of magnitude smaller than the

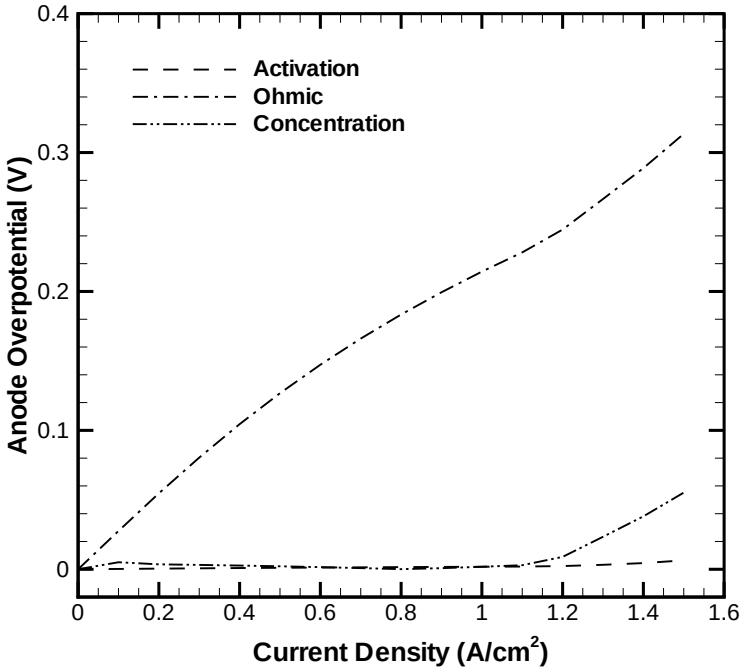

Figure 6.5: Anode overpotentials in an anode-supported SOFC at base case conditions listed in Table 6.7.

anode ohmic overpotential.

In contrast to the anode concentration overpotential, the cathode concentration overpotential in an anode-supported SOFC is negligible. This is due to small thickness of the cathode. However, the contributions of cathode activation and cathode ohmic overpotentials are significant to the total cell potential loss, which can be evident from Figure 6.7. Further, it is clear from Figures 6.5 and 6.7 that the ohmic overpotential is the single largest contributor to the cell potential loss in anode-supported SOFCs. More specifically, it is the temperature dependent ionic conductivity of the ion-conducting particles in the reaction zone layers which is contributing to the overall ohmic overpotential. Hence, ionic conductivity of the ion-conducting particles should be enhanced by developing new materials or designs to improve performance of anode-supported SOFCs.

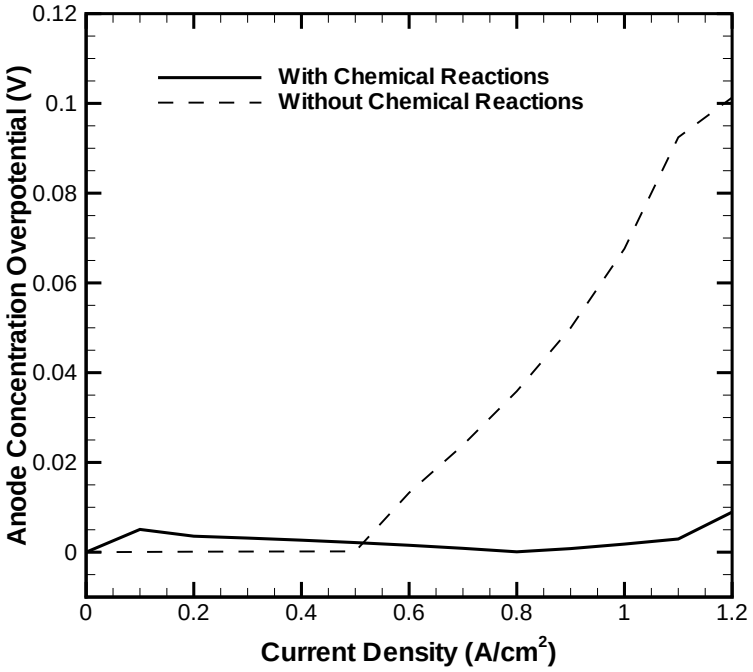

Figure 6.6: Comparison of anode concentration overpotential in an anode-supported SOFC at base case conditions listed in Table 6.7.

6.3.2 2-D Self-Supported Model

In a self-supported SOFC design, the thickness of the electrode and electrolyte layers are of comparable magnitude. Since it is designed for high temperature operation (around 1273 K), it can also be referred to as high-temperature SOFC.

The fuel composition used to simulate the performance of self-supported SOFC is same as anode-supported SOFC listed in Table 6.3. Again, most of the base case parameters used in the simulation

Table 6.8: Base case parameters used in the simulation of a self-supported SOFC.

Operating temperature, T_{op}	1273.0 K
Anode backing layer thickness, t_{abl}	190.0 μm
Anode reaction zone layer thickness, t_{arl}	10.0 μm
Electrolyte thickness, t_{el}	150.0 μm
Cathode backing layer thickness, t_{cbl}	190.0 μm
Cathode reaction zone layer thickness, t_{crl}	10.0 μm

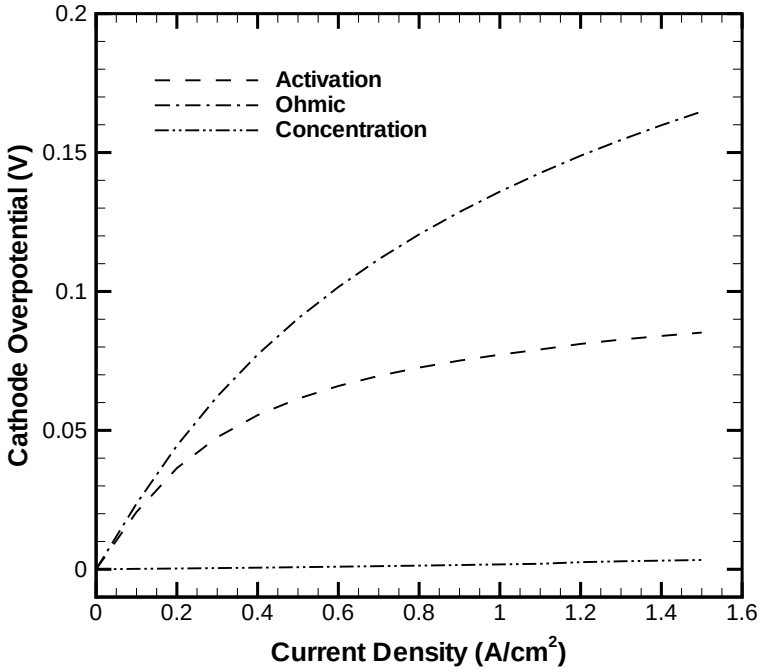

Figure 6.7: Cathode overpotentials in an anode-supported SOFC at base case conditions listed in Table 6.7.

of a self-supported SOFC are similar to the parameters used in the simulation for verification of modeling an electrode as two distinct layers; however, base case parameters which are different from the parameters used in the verification of electrode modeling are listed in Table 6.8.

Figure 6.8 shows the base case performance of a self-supported SOFC resulting from the fuel composition and base case parameters listed in Tables 6.3 and 6.8. The operating temperature and pressure were set as 1273 K and 1 atm, respectively. Again, the solid line represents the actual cell potential and power density when all the overpotentials are subtracted from the reversible cell potential. It can be seen that the actual cell performance curve exhibit the activation overpotential region at low current densities, and does not exhibit the concentration overpotential region at high current densities, indicating the negligible contribution of concentration overpotential in self-supported SOFCs. It can also be seen that the maximum power density obtained from a self-supported SOFC operating at 1273 K is around 0.36 W/cm^2. Further, it is observed that the

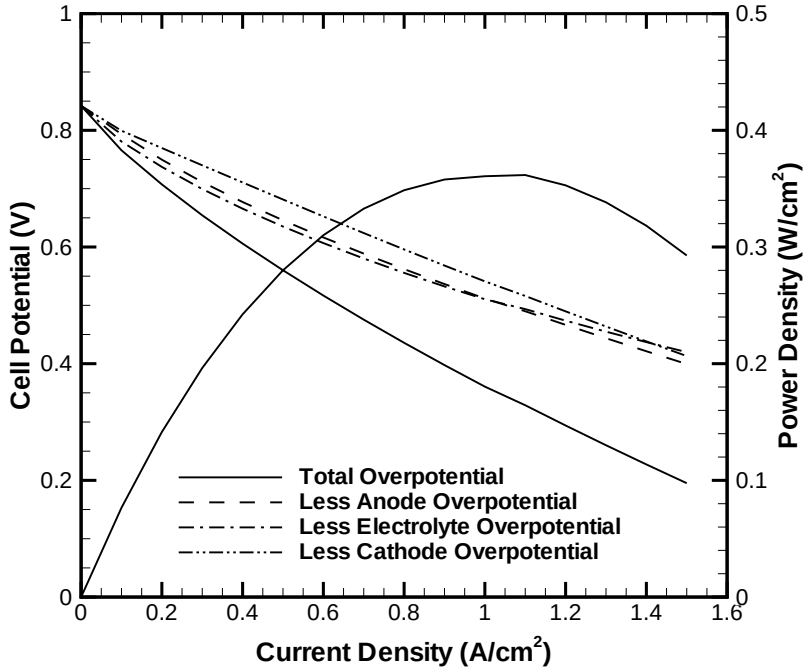

Figure 6.8: Base case performance of a self-supported SOFC.

cathode overpotential is the largest contributor to the cell potential loss; whereas, anode and electrolyte overpotentials are of comparable magnitude for all the current density range considered in the present simulation.

The difference in the anode and cathode overpotentials comes from respective activation overpotentials, which can be evident from Figures 6.9 and 6.10. Unlike in an anode-supported SOFC, the ohmic overpotential is not the single largest contributor to the cell potential loss in a self-supported SOFC. This is due to high temperature operation of self-supported SOFC compared to an anode-supported SOFC, which increases the ionic conductivity of the ion-conducting particles in the reaction zone layers resulting in reducing the contribution of ohmic overpotential. In addition, due to equal thickness of reaction zone layers (anode and cathode) in self-supported SOFC, the ohmic contribution of electrodes is of comparable magnitude. Further, it is observed from Figures 6.9 and 6.10 that the concentration overpotentials of anode and cathode are negligible, which

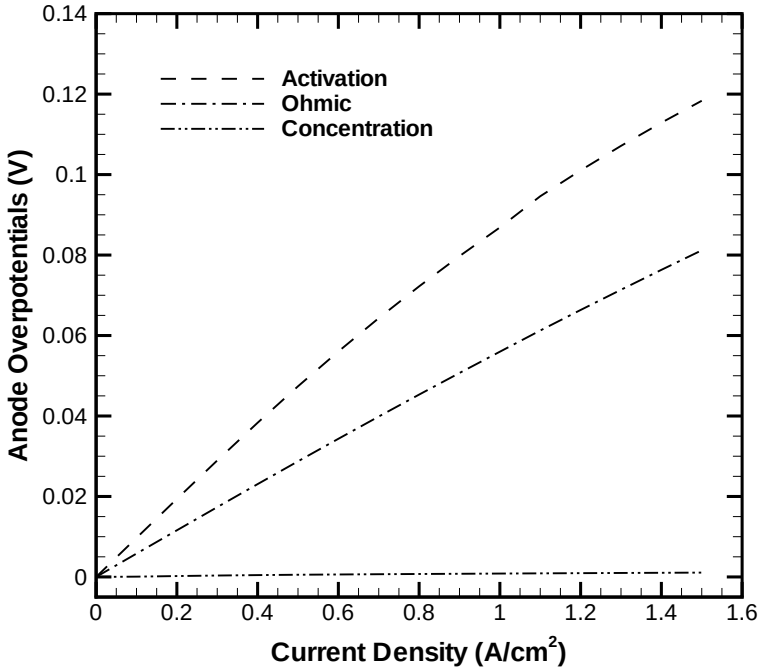

Figure 6.9: Anode overpotentials in a self-supported SOFC at base case conditions listed in Table 6.8.

can be attributed to the small thickness of the electrodes.

The effect of electrolyte thickness on the performance of a self-supported SOFC is shown in Figure 6.11. Again, the operating temperature and pressure were set as 1273K and 1 atm, respectively. It can be seen that decreasing the thickness of the electrolyte layer increases the performance of a self-supported SOFC. Further, it is observed that the maximum power density obtained by reducing the electrolyte layer thickness to 100 μm is above 0.4 W/cm^2. This is due to reduced ohmic contribution of the electrolyte layer, which decreases with the decrease of electrolyte layer thickness. The performance can be enhanced by further reducing the thickness of the electrolyte; however, for a self-supported design, the thickness of each component is of the order of 100 μm.

To examine to effect of reducing the operating temperature on the performance of a self-supported SOFC, the operating temperature is reduced to 1073 K (800^{o}C), similar to base case operating temperature for an anode-supported SOFC. Figure 6.12 shows the effect of operating

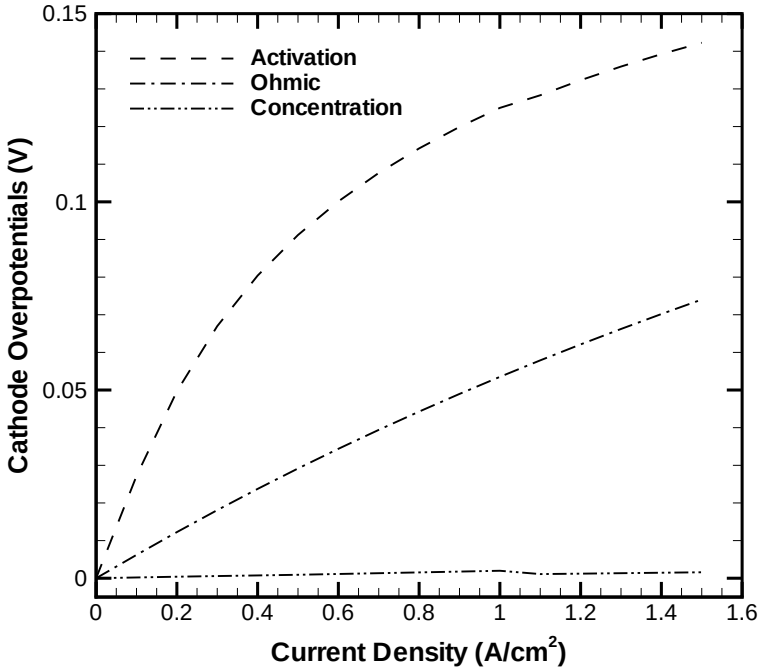

Figure 6.10: Cathode overpotentials in a self-supported SOFC at base case conditions listed in Table 6.8.

temperature on the performance of a self-supported SOFC. The other operating and design parameters are set as base case parameters listed in Table 6.8 except the thickness of the electrolyte, which is reduced to 100 μm instead of 150 μm. Reducing the operating temperature decreases the performance of a self-supported SOFC and limiting current density is reached just about 1 A/cm^2. Further, it is observed that the maximum power density is reduced to about 0.2 W/cm^2 at 1073 K, which is almost half of the maximum power density at 1273 K. The decrease in performance of a self-supported SOFC with temperature is due to decrease in temperature-dependent ionic conductivity of the electrolyte layer and ion-conducting particles of the reaction zone layers; as a result, the ohmic overpotential of the electrolyte and electrode layers increases, which in turn results in decreasing the performance.

A worthwhile comparison of performance between self-supported and anode-supported SOFCs at their base case conditions is shown in Figure 6.13. It should be noted that the base case oper-

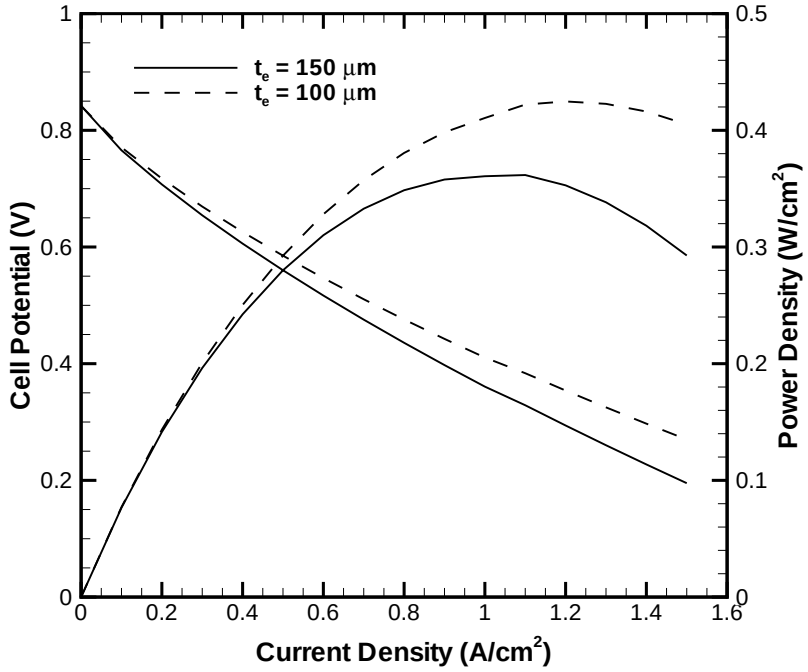

Figure 6.11: Effect of electrolyte thickness on the performance of self-supported SOFC.

ating temperature of a self-supported SOFC is 1273 K (1000^{o}C); whereas, the base case operating temperature of an anode-supported SOFC is 1073 K (800^{o}C). Further, it should be noted that the electrolyte thickness for self-supported SOFC is set as 100 μm instead of 150 μm listed in Table 6.8. It can be seen that both the designs (self-supported and anode-supported) exhibit similar performance in the operating range of SOFC (0.5-0.7 A/cm^2). Moreover, it can be seen that self-supported SOFC shows better performance at higher current densities, which can be attributed to negligible anode concentration overpotential in a self-supported SOFC when compared to an anode-supported SOFC. However, there are material-related problems associated with self-supported SOFCs because of their high operating temperature such as corrosion and/or oxidation. In addition, high operating temperature of self-supported SOFCs require expensive high chrome alloys or oxides for interconnects, thereby increasing the material and manufacturing costs. On the other hand, anode-supported SOFCs exhibit similar performance to that of self-supported SOFCs

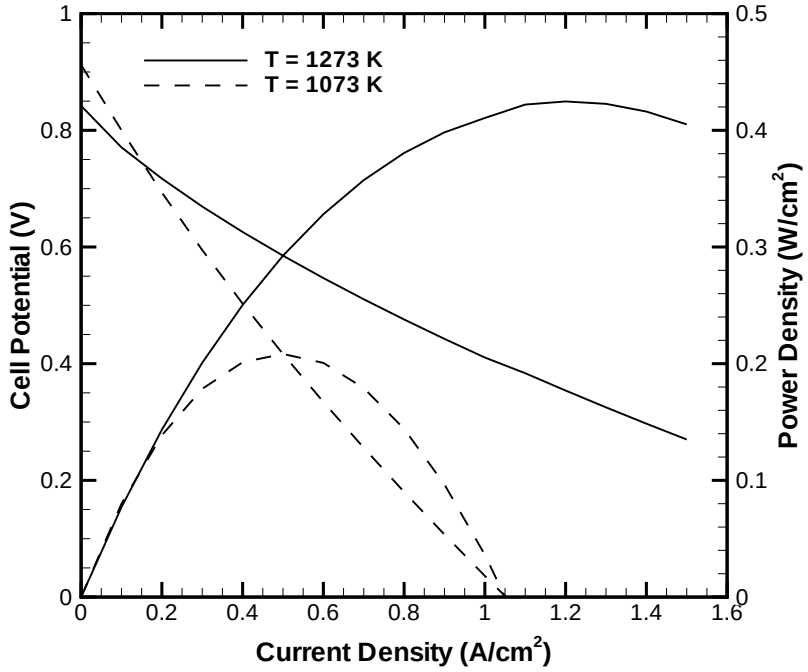

Figure 6.12: Effect of operating temperature on the performance of self-supported SOFC.

at reduced operating temperature. As stated before, reducing the operating temperature of SOFCs through better designs and configurations to around 973 K, many of the material-related problems can be resolved. Thus, anode-supported design of SOFCs is the potential design for operating at reduced temperatures, which can help in speeding the process of commercialization for planar SOFCs.

6.3.3 3-D Anode-Supported Model

As it is known that the reactant composition changes along the flow path over the electrode surface due to consumption of reactants and production of reaction products, the 2D anode-supported SOFC model is extended to third dimension, thereby incorporating the effect of reactant composition change along the flow path over the electrode surface; as a result, a 3D anode-supported SOFC model has been developed. The fuel composition and the base case parameters used in the simu-

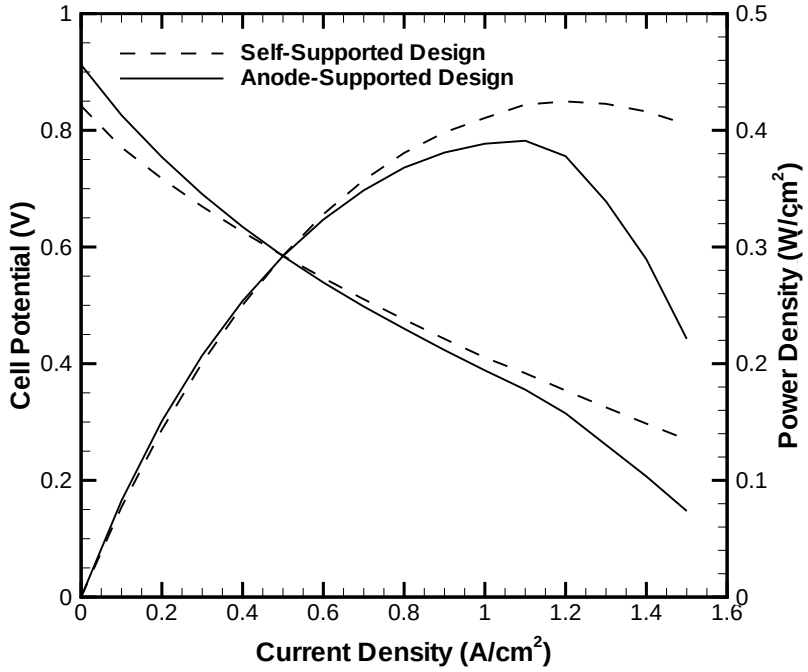

Figure 6.13: Comparison of self-supported SOFC and anode-supported SOFC at their base case conditions.

lation of 3D anode-supported model is similar to 2D anode-supported model listed in Tables 6.3 and 6.7; however, an additional design parameter required for 3D anode-supported SOFC model is the length of the channel (cell), which is set as 20 mm. The predicted performance resulting from the 3D anode-supported model is shown in Figure 6.14.

It can be seen from Figure 6.14 that actual performance profile exhibits both the concave and convex curvatures at low and high current densities, respectively, thereby indicating the regions of activation and concentration overpotentials in an anode-supported SOFC. The maximum power density predicted by the 3D model is about 0.36 W/cm^2. It can also be seen that the anode overpotential is the single largest contributor to the cell potential loss at higher current densities, followed by the cathode and electrolyte overpotentials, consistent with the predictions of 2D anode-supported model shown in Figure 6.4. Additionally, it is observed that the profiles without electrolyte and cathode overpotentials exhibit the convex curvature at high current densities;

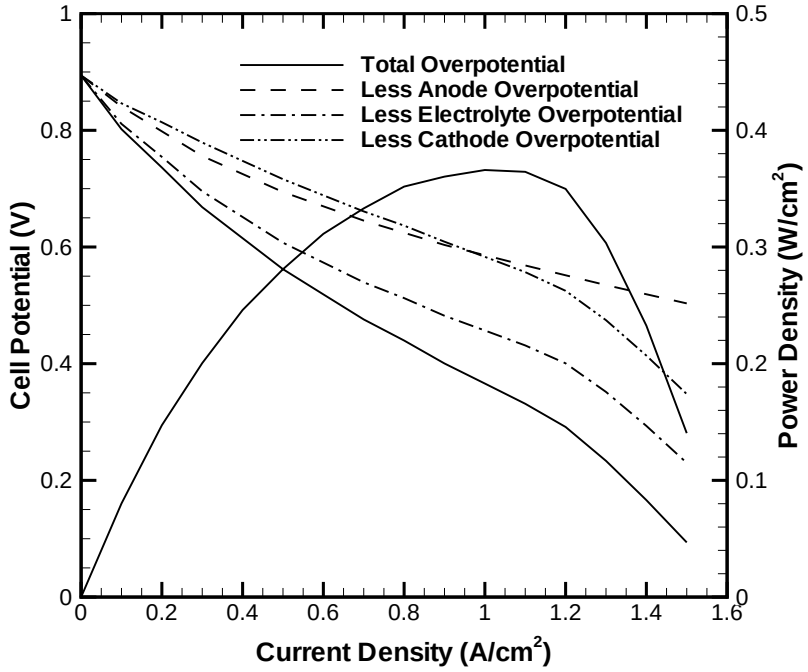

Figure 6.14: Base case performance of a 3D anode-supported SOFC model.

whereas, the profile without anode overpotential does not exhibit the convex curvature at high current densities, thereby attributing the convex portion of the actual performance curve to the anode concentration overpotential.

A comparison of base case performance predicted by 2D and 3D anode-supported SOFC models is shown in Figure 6.15. It can be seen that both performance curves follow similar trends at all the current density range considered in the present simulation. The base case performance predicted by the 3D model is less than the base case performance predicted by the 2D model. The difference in the performance predicted by 2D and 3D models is due to the change in the concentration of the reactants along the length of the channel (cell). Since the reactant concentration changes along the length of the channel, the reversible cell potential, which is a function of temperature, pressure and reactant concentration, also varies along the length of the channel. Due to difference in the value of reversible cell potential, a constant difference can be observed in the performance curves

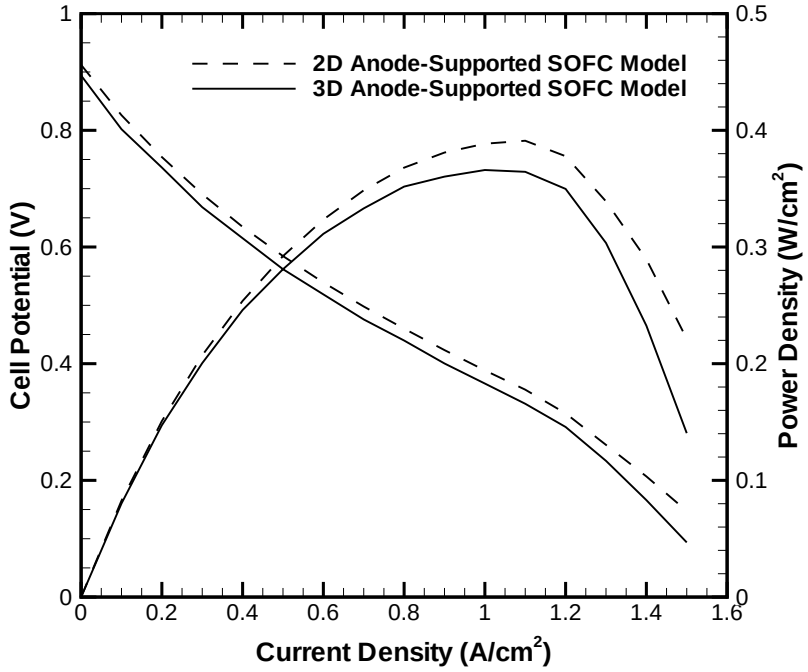

Figure 6.15: Base case performance predicted by 2D and 3D anode-supported SOFC models.

of 2D and 3D models until an appreciable difference is observed at higher current densities. At higher current densities, the difference in the performance curves is due to difference in the anode concentration overpotential, which is shown in Figure 6.16. It can be seen from Figure 6.16 that the anode concentration overpotential predicted by the 3D model is an order of magnitude higher than the anode concentration overpotential predicted by the 2D model at higher current densities. Therefore, the thickness of the anode in an anode-supported SOFC should be reduced to minimize the contribution of anode concentration overpotential at higher current densities.

6.3.4 3-D Self-Supported Model

Similar to 3-D anode-supported SOFC model, 2-D self supported model is extended to third dimension to incorporate the effect of reactant composition change along the flow path over the electrode surface, resulting in the development of a 3-D self-supported SOFC model. Again, the

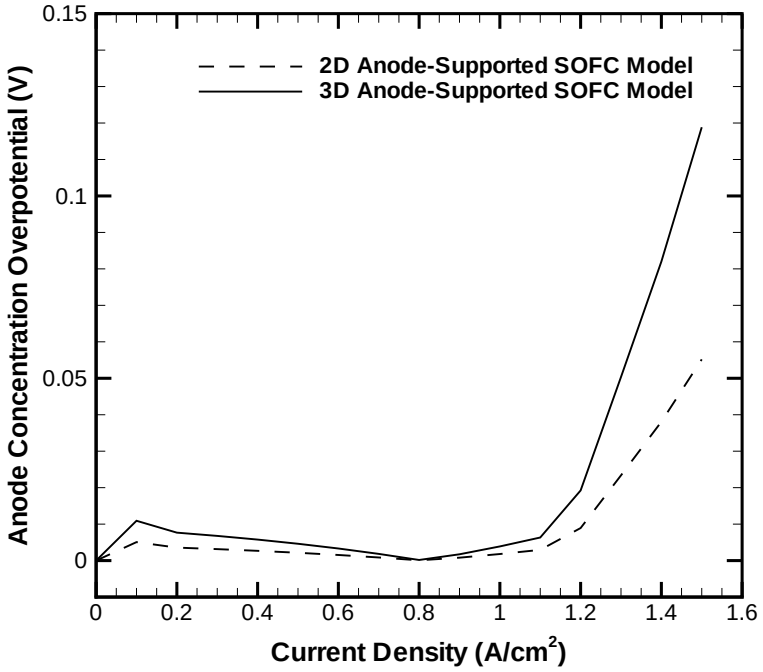

Figure 6.16: Anode concentration overpotential predicted by 2D and 3D anode-supported SOFC models.

fuel composition and the base case parameters used in the simulation of 3-D self-supported model is similar to 2-D self supported model listed in Tables 6.3 and 6.8. Further, an additional design parameter required for 3-D self-supported model is the length of the channel (cell), which is again set as 20 mm. The performance predicted by the 3-D self-supported model is compared with the 2-D self-supported model, and is shown in Figure 6.17. The operating temperature and pressure were set as 1273 K and 1 atm, respectively. It can be seen that the performance curve predicted by the 3-D model is in accordance with the 2-D model for all the current density range considered in the present simulation. However, the performance predicted by the 3-D model is less than the performance predicted by the 2-D model. This is again due to the change in reactant concentration along the length of the channel (cell), which not only affects the reversible cell potential but also the actual cell potential. However, due to small thickness of the backing layers in self-supported SOFCs, there is no significant drop in cell potential at higher current densities.

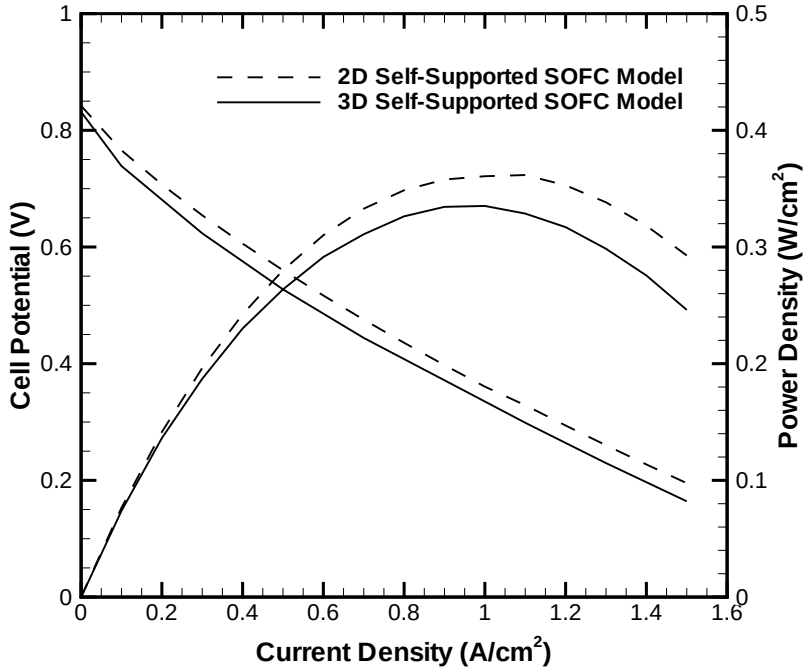

Figure 6.17: Base case performance predicted by 2D and 3D self-supported SOFC models.

6.4 Parametric Study

In order to probe the robustness of the model, a parametric study has been performed to examine the effect of various operating and design conditions on the performance of an anode-supported SOFC. Moreover, as it is rightly stated by Alkhateeb et al. [92] that a comprehensive model would analyze the effect of macroscopic and microscopic characteristics of the electrodes on cell performance.

The model used to examine the effect of various design and operating parameters on the performance of an anode-supported SOFC is a 2-D anode-supported model, and has been chosen due to following reasons. Firstly, it is computationally less expensive than the 3-D anode-supported model. Secondly, the performance predicted by 3-D anode-supported model qualitatively matches well with the 2-D anode-supported model.

6.4.1 Effect of Temperature

To start with, the effect of temperature on the performance of an anode-supported SOFC is shown in Figure 6.18. Anode-supported SOFCs typically operate in an intermediate temperature range between 823 K and 1073 K [12]. In the present simulation, temperature in the typical range is varied to examine its effect on the performance of an anode-supported SOFC. The reaction rate constants for the chemical reactions are valid for the temperature range considered in the present simulation [61]. Further, the other operating and design parameters are kept constant in accordance with the base case parameters. It can be seen that increasing the operating temperature of the cell increases the performance of an anode-supported SOFC. It can also be seen that increasing the operating temperature increases the limiting current density, which corresponds to the current density at the zero cell potential. Moreover, the power density increases with the increase in operating temperature with its peak shifted towards higher current densities at higher temperatures. The reason for the increase in cell performance with temperature is primarily due to the increase in temperature dependent ionic conductivity of the ion-conducting particles in the reaction zone layers, which in turn reduces the contribution of ohmic overpotential of the electrodes. Further, ionic conductivity of the electrolyte layer increases with the increase in operating temperature, resulting in better cell performance. The increase in limiting current density with operating temperature is due to the fact that molecular diffusivity of the species increases with temperature, which reduces the resistance to mass transport in the thick anode, and thereby reduces the anode concentration overpotential with temperature. Although there are many incentives in reducing the operating temperature but there is a significant drop in cell performance just by reducing the temperature from 1073 K to 973 K, which can be evident from Figure 6.18. Hence, ionic conductivity of the ion-conducting particles in the reaction zone and electrolyte layers need to be enhanced in order to operate anode- supported SOFCs below 1073 K.

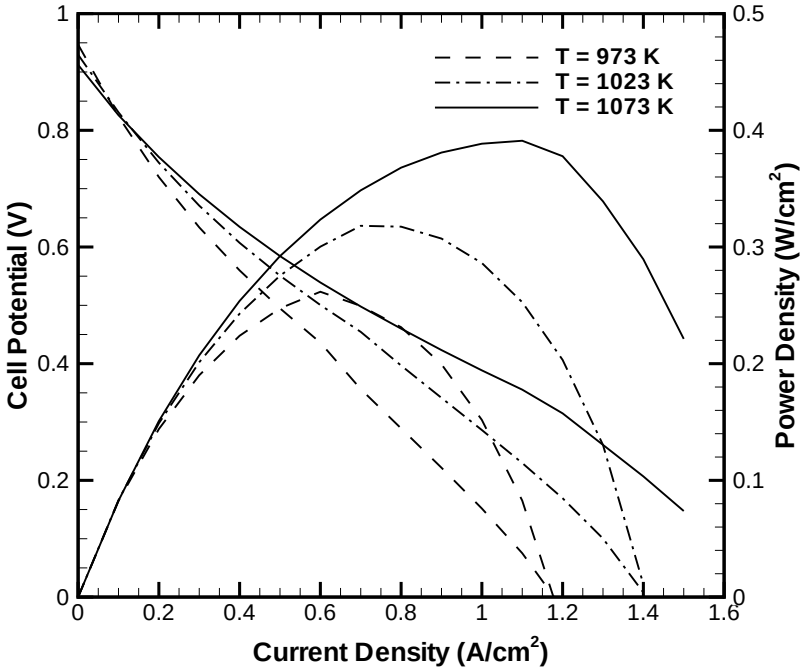

Figure 6.18: Effect of temperature on the performance of an anode-supported SOFC.

6.4.2 Effect of Pressure

The effect of pressure on the performance of an anode-supported SOFC is shown in Figure 6.19. The other operating and design parameters are set as base case parameters. It can be observed that increasing the pressure increases the performance of an anode-supported SOFC. This is due to increase in reactant concentration at the reaction sites, which in turn enhances the rate of electrochemical reactions. Subsequently, the contribution of anode and cathode overpotentials are reduced and hence better performance. However, there are constraints in increasing the pressure such as gas sealing problems, limitations on material selection and mechanical strength of the cell components [93]. Therefore, increasing the pressure is not always the best option to improve performance.

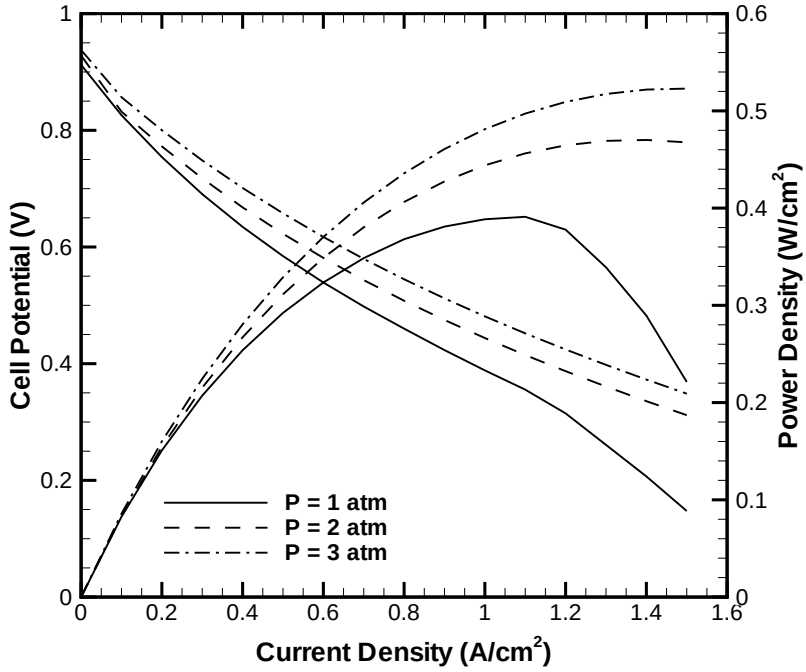

Figure 6.19: Effect of pressure on the performance of an anode-supported SOFC.

6.4.3 Effect of Anode Reaction Zone Thickness

The thickness of the reaction zone layers is one of the important parameters in the electrodes of an SOFC. Different values are reported in the literature based on the thickness of the electrode ranging from 10 μm to 50 μm [18, 19, 21–23]. The effect of anode reaction zone thickness on the performance of an anode-supported SOFC is shown in Figure 6.20. The operating and other design parameters are kept the same as those listed in Table 6.7. In addition, the combined thickness of the anode backing layer and the reaction zone layer is kept as 2 mm. Increasing the reaction zone thickness increases the TPBs in the reaction zone layer resulting in the increased rate of electrochemical reaction, which in turn reduces the activation overpotential. However, increasing the reaction zone thickness increases the distance through which oxide ions and electrons migrate to reach the reaction sites. Due to poor ionic conductivity of the ion-conducting particles, increasing the reaction zone thickness increases the ohmic overpotential. The balance between the decrease in

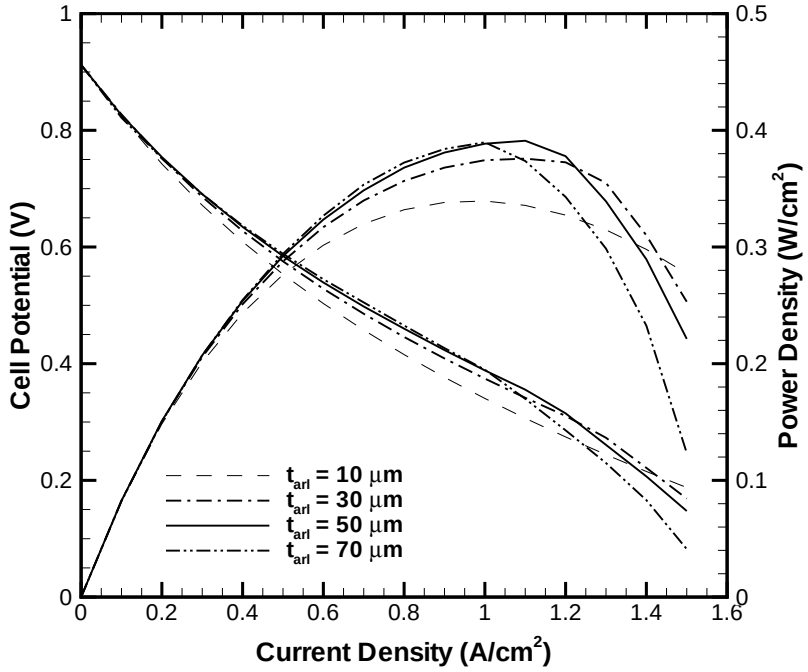

Figure 6.20: Effect of anode reaction zone thickness on the performance of an anode-supported SOFC.

the activation overpotential and the increase in the ohmic overpotential reflects the improvement in cell performance with respect to the increase in the anode reaction zone thickness. A close observation of Figure 6.20 reveals that there is no significant increase in the performance when the anode reaction zone thickness is increased from 30 μm to 70 μm, in fact, the performance is reduced at higher current densities.

6.4.4 Effect of Porosity

The effect of porosity on the performance of an anode-supported SOFC is illustrated in Figure 6.21. All other operating and design parameters are kept the same as for the conditions shown in Table 6.7. It can be observed that increasing the porosity of the porous layers decreases the performance of an anode-supported SOFC; however, the performance increases with increasing the porosity at higher current densities. This is due to reduction in mass transport resistance with

increasing the porosity of the porous layers at higher current densities. In contrary, increasing the porosity decreases the effective conductivities of the porous layers resulting in the increased contribution of ohmic overpotentials for most of the current density range considered in the present simulation.

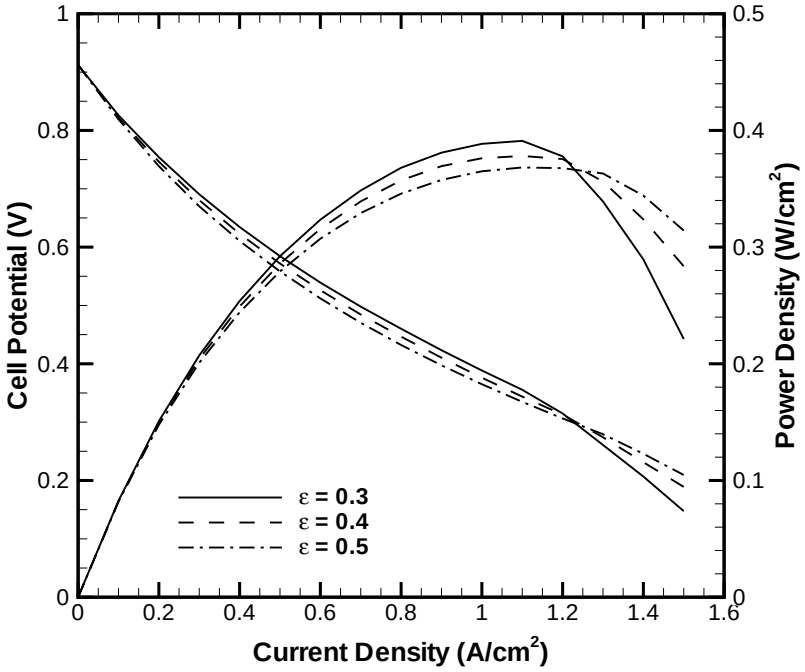

Figure 6.21: Effect of porosity on the performance of an anode-supported SOFC.

6.4.5 Effect of Tortuosity

Figure 6.22 shows the effect of tortuosity of the porous layers on the performance of an anode-supported SOFC. Again, the other design and operating parameters are set equal to the base case parameters listed in Table 6.7. One of the primary deficiencies of some of the earlier models is the need to invoke tortuosities in the range of 10 to 17 [9, 29]. The reason for invoking such high tortuosities is to produce the concentration overpotential [94]. However, tortuosities for the porous layers of SOFC have been experimentally determined to be in the range of 2.5-6.0 [18, 19, 94, 95].

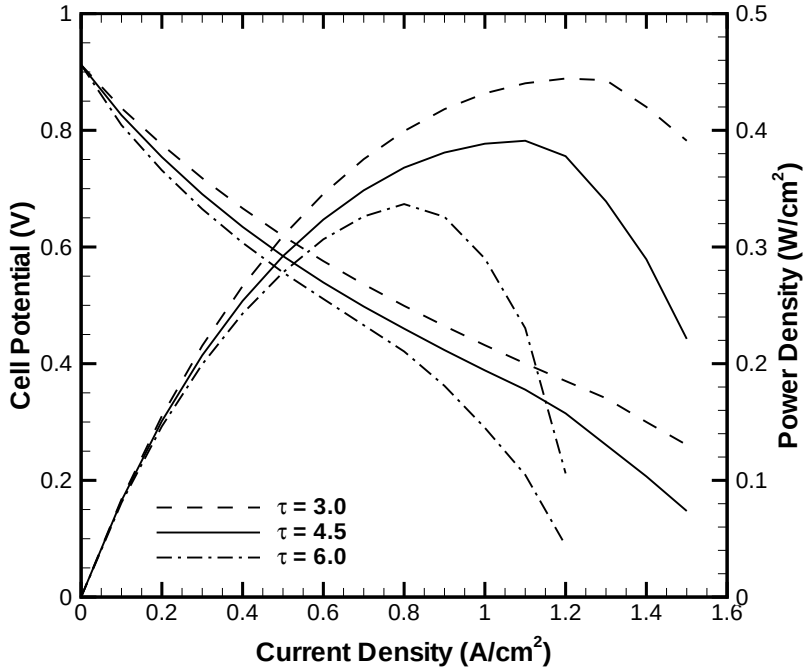

Figure 6.22: Effect of tortuosity on the performance of an anode-supported SOFC.

Therefore, in the present simulation, tortuosity of the porous layers has been varied between 3.0 and 6.0. Increasing the tortuosity of the porous layers increases the resistance to mass diffusion due to increase diffusion path length, which results in the reduction of reactant concentration at the reaction sites; as a result, the contributions of activation and concentration overpotentials to the cell potential loss increases with the increase of tortuosity. Further, the effective conductivities of the porous layers decreases with the increase of tortuosity, resulting in the increase of ohmic contribution of the porous layers and hence cell performance decreases with the increase of tortuosity.

6.4.6 Effect of Composition of Electron-Conducting Particles in the Reaction Zone Layers

The composition of electron-conducting particles in the reaction zone layers is an important parameter affecting the cell performance, and its effect is shown in Figure 6.23. The composition

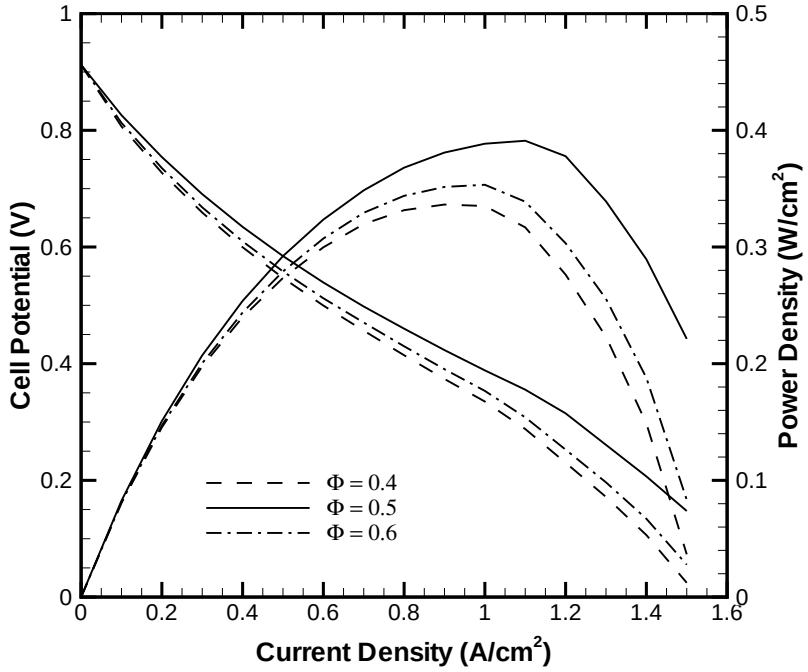

Figure 6.23: Effect of volume fraction of electron-conducting particles on the performance of an anode-supported SOFC.

is represented by the volume fraction of electron-conducting particles (Φ) in the reaction zone layers, which is varied from 0.4 to 0.6. The operating and design conditions remain the same as the base case parameters listed in Table 6.7. It is seen that increasing the volume fraction of electron-conducting particles in reaction zone layers from 0.4 to 0.5 increases the performance of an anode-supported SOFC; however, further increase in the volume fraction of electron-conducting particles in the reaction zone layers results in the reduction of cell performance. This is due to the fact that the largest reactive surface for electrochemical reactions is achieved when the dimensions and volume fractions of electron- and ion-conducting particles are equal and hence better performance [29]. Moreover, the effective electronic and ionic conductivities in the reaction zone layers are functions of the volume fraction of electron-conducting particles; increasing Φ beyond 0.5 increases the effective electronic conductivity but decreases the effective ionic conductivity in the reaction zone layers resulting in an increase in the ohmic overpotential, and thereby decreasing

the cell performance.

6.5 Phenomena Prediction

As stated before, the present model not only predicts the performance of the cell but also predicts various processes in different layers of the cell. This section deals with prediction of various inter-dependent fields in different components of the cell at specified design and operating conditions.

6.5.1 Species Distribution

A cross-sectional distribution of various species in the anode backing layer of an anode-supported SOFC at 0.5 A/cm^2 is shown in Figure 6.24. The fuel composition is similar to the one used to predict the performance, and is listed in Table 6.3. The operating temperature and pressure were set as 1073 K and 1 atm, respectively. Further, it should be noted that there are no chemical reactions (reforming and water-gas shift reactions) considered for the present condition. The horizontal and vertical axis of Figure 6.24 represent the dimensionless width and dimensionless anode backing layer thickness of the physical domain. It can be seen that the concentration or mole fraction of H_2 decreases, while the mole fraction of H_2O increases, as we from top to bottom of their respective sub-plots. This is due to anode reaction zone layer beneath the anode backing layer wherein electrochemical H_2 oxidation occurs, resulting in the consumption of H_2 and production of H_2O. The variation in the concentration or mole fractions of other non-reacting species such as CH_4, CO, and CO_2 along the thickness of the anode backing layer is primarily due to multi-component diffusion, wherein the concentration or mole fraction of one species depends on the concentration or mole fraction of other n-1 species.

Figure 6.25 shows the effect of load or current density change on the cross-sectional distribution of reactant H_2 and reaction product H_2O in the anode backing layer of an anode-supported SOFC. Again, the operating temperature and pressure are set as 1073 K and 1 atm, respectively. Moreover, neither reforming nor water-gas shift reaction is considered for the present situation. It can be seen that increasing the load or current density decreases the mole fraction of H_2 as we move from top

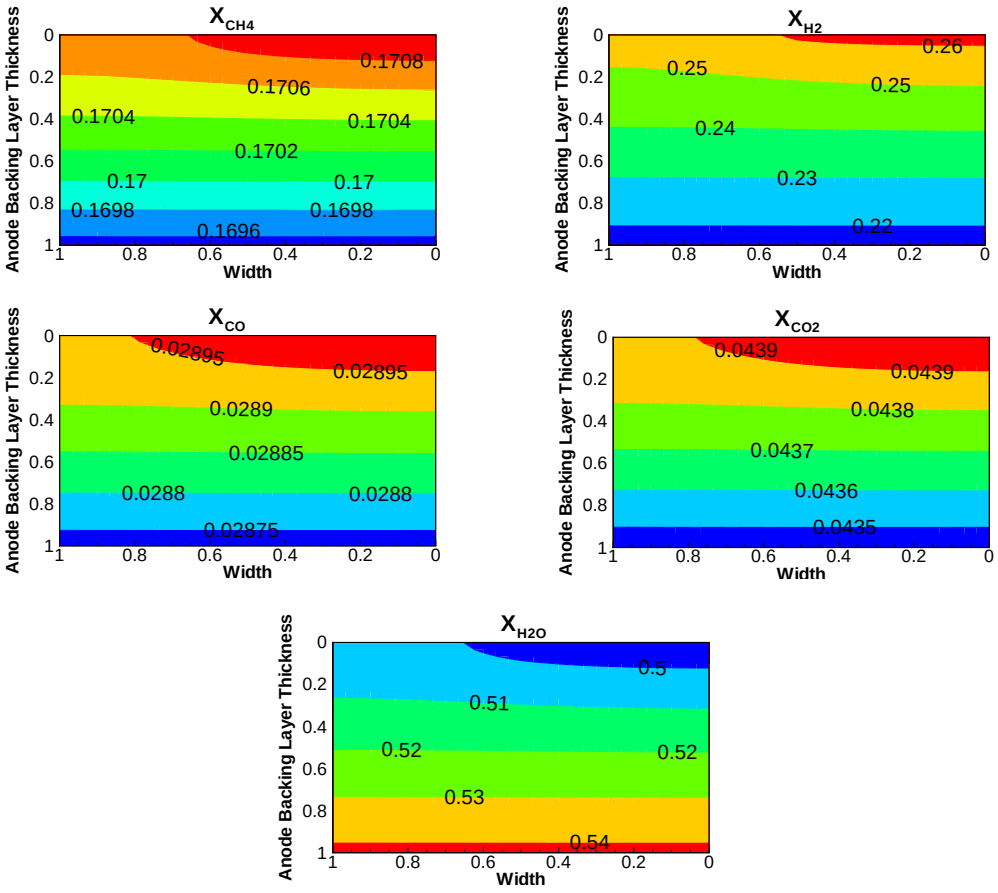

Figure 6.24: Cross-sectional distribution of various species in the anode backing layer of an anode-supported SOFC at 0.5 A/cm^2.

to bottom of the backing layer; on the other hand, mole fraction of H_2O increases with increasing the current density. Increasing the current density increases the consumption of reactant H_2 in the reaction zone layer resulting in increased production of reaction product H_2O, which in turn reduces the concentration or mole fraction of H_2 and enhances the mole fraction of H_2O in the backing layer.

A 3D contour plot illustrating the distribution of H_2 mole fraction in the anode backing layer at 0.5 A/cm^2 is shown in Figure 6.26. The operating temperature and pressure were again set as 1073 K and 1 atm, respectively. Further, there are no chemical reactions in the anode for this particular situation. The 3D affects on the distribution of H_2 are evident from the figure. Due to smaller channel length (2 cm), a better boundary condition at the top of the backing layer surface

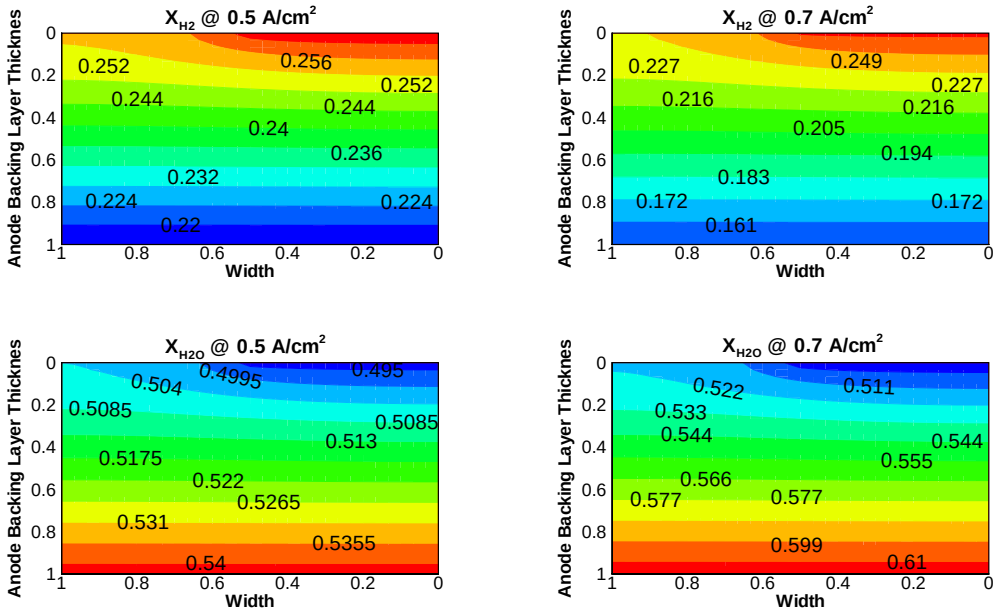

Figure 6.25: Cross-sectional distribution of H_2 and H_2O in the anode backing layer of an anode-supported SOFC at different current densities.

is approximated as constant current density, which resulted in linear variation of H_2 mole fraction along the length of the channel at the top of the backing layer surface. However, the distribution tends to deviate from linearity within the thickness of the backing layer along the length of the channel interfacing the reaction zone layer. This is due to 3D diffusion within the backing layer and consumption of H_2 at the bottom of the backing layer interfacing the reaction zone layer due to electrochemical oxidation reaction.

A 3D slice plot showing the distribution of H_2 mole fraction at different locations along the length of the channel is shown in Figure 6.27. The slices of the 3D plot are taken at the inlet, at half-length from the inlet, and at the exit of the channel. It can be seen that H_2 mole fraction varies at different locations along the channel. Since there are no chemical reactions in the anode for this particular situation, a significant drop in the concentration or mole fraction of H_2 can be observed along the length of the channel. Further, the concentration or mole fraction of H_2 varies within the thickness of the backing layer at different locations along the channel. This is again due to diffusion within the backing layer and electrochemical oxidation reaction at the bottom of the

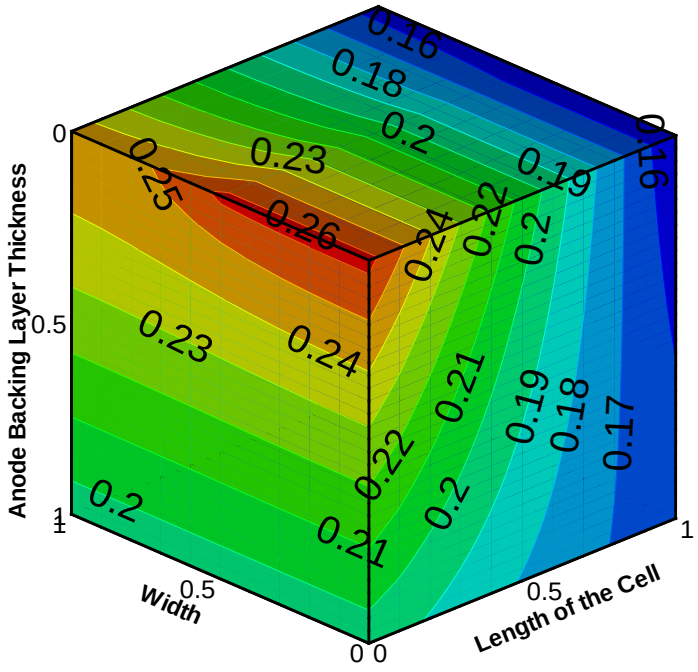

Figure 6.26: 3D contour plot showing the distribution of H_2 in the anode backing layer at 0.5 A/cm^2.

backing layer, which is interfacing the reaction zone layer.

Similarly, a 3D slice plot illustrating the distribution of H_2 mole fraction at different locations along the thickness of the backing layer is shown in Figure 6.28. The slices are taken at the top of the backing layer interfacing the fuel channel, half-thickness of the backing layer and the bottom of the backing layer interfacing the reaction zone layer. A linear distribution of H_2 mole fraction is observed at different thicknesses of the backing layer along the length of the channel. Further, it can be seen that H_2 concentration or mole fraction at the bottom of the backing layer interfacing reaction zone is not constant, which often difficult to predict without resorting to a 3D model.

Finally, a 3D slice plot illustrating the distribution of H_2 mole fraction at different widths of the backing layer is shown in Figure 6.29. Due to small width compared to the thickness of the backing layer and length of the channel, the distribution of H_2 mole fraction at different locations along the width are almost similar. Moreover, there is a finite consumption of reactant H_2 at the

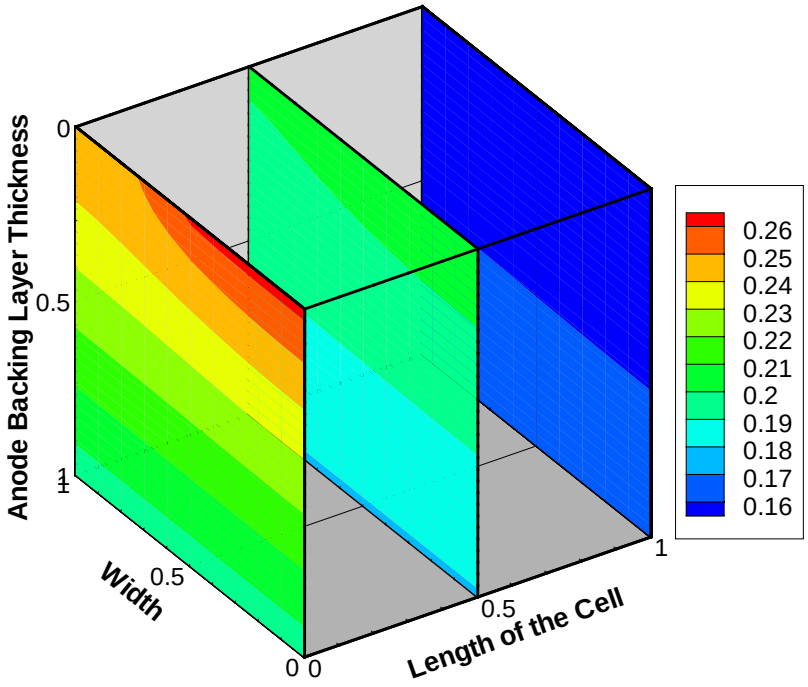

Figure 6.27: 3D slice plot showing the distribution of H_2 mole fraction in the anode backing layer at different locations along the channel.

bottom of the backing layer, which results in non-uniform distribution of H_2 mole fraction within the backing layer.

The effect of chemical reactions (methane reforming and water-gas shift) on the distribution of mole fractions of H_2 and H_2O in the anode backing layer at 0.7 A/cm^2 is shown in Figure 6.30. The figure illustrates the cross-sectional distribution of mole fractions of H_2 and H_2O at the inlet of the channel with and without consideration of chemical reactions. The chemical reactions include methane reforming and water-gas shift reactions. The temperature and pressure were set as 1073 K and 1 atm, respectively. It can be seen that the concentration or mole fraction of H_2 in the backing layer increases to a certain thickness when chemical reactions are considered in the anode; consequently, the concentration or mole fraction of H_2O decreases for the same thickness. This is because of production of 3 moles of H_2 for each mole of H_2O consumed through methane-reforming reaction and 1 mole of H_2 for each mole of H_2O consumed through water-gas shift

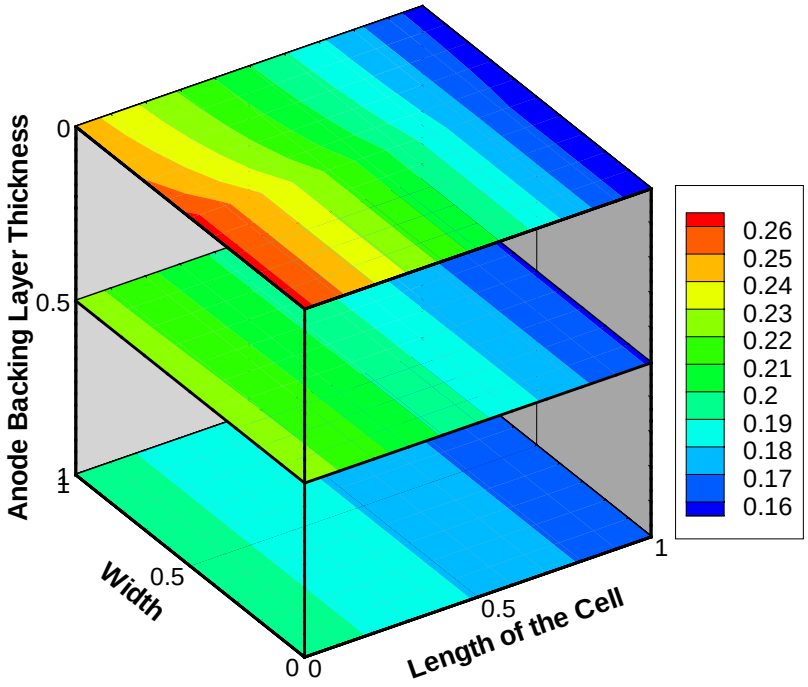

Figure 6.28: 3D slice plot showing the distribution of H_2 fraction in the anode backing layer at different locations along the thickness of the backing layer.

reaction. However, at the bottom of the backing layer, the mole fraction H_2 decreases and the mole fraction H_2O increases, respectively. This is due to higher rate of electrochemical reaction than the rate of methane-reforming and water-gas shift reactions in the reaction zone layer beneath the backing layer, which results in the decrease H_2 mole fraction and increase of H_2O mole fraction at the bottom of the backing layer. Moreover, it can be seen that there is a significant difference in the magnitude of mole fraction of H_2 when chemical reactions are considered in the anode, which clearly exhibits the contribution of chemical reactions in reducing the anode concentration overpotential in thick anodes of anode-supported SOFCs.

Similarly, a cross-sectional distribution of O_2 mole fraction in the cathode backing layer at different densities is shown in Figure 6.31. Due to small thickness when compared to the thickness of the anode backing layer in an anode-supported SOFC, the variation of O_2 mole fraction along the thickness of the cathode backing layer is not significant at both the current densities shown in

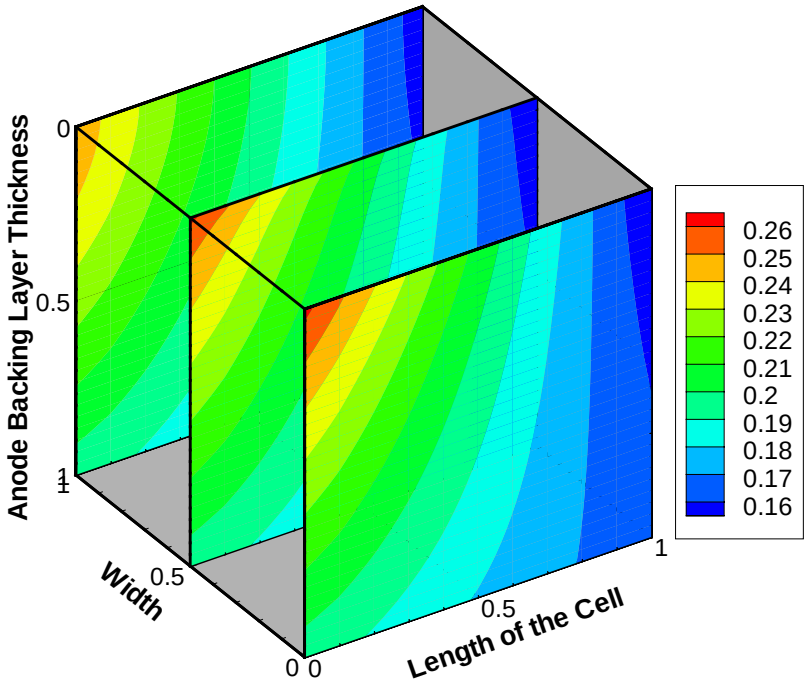

Figure 6.29: 3D slice plot showing the distribution of H_2 fraction in the anode backing layer at different locations along the width of the backing layer.

the figure. However, a 3D slice plot illustrating the distribution of O_2 mole fraction at different locations along the length of the channel exhibits the considerable reduction in the mole fraction of O_2, which can be evident from Figure 6.32.

The cross-sectional distributions of H_2 and H_2O mole fractions in the anode reaction zone layer at 0.5 A/cm^2 is shown in Figure 6.33. Because of electrochemical H_2 oxidation reaction in the anode reaction zone layer, the concentration or mole fraction of H_2 decreases while the concentration or mole fraction of H_2O increases along the thickness of the anode reaction zone. However, the decrease and increase of respective mole fraction of H_2 and H_2O along the thickness of the anode reaction zone is not significant, which can be attributed to small thickness of reaction zone layer when compared to the thickness of the backing layer. Similarly, the cross-sectional distribution of O_2 mole fraction in the cathode reaction zone layer at 0.5 A/cm^2 is shown in Figure 6.34. Due to small thickness of the cathode backing layer in an anode-supported SOFC, there is a significant

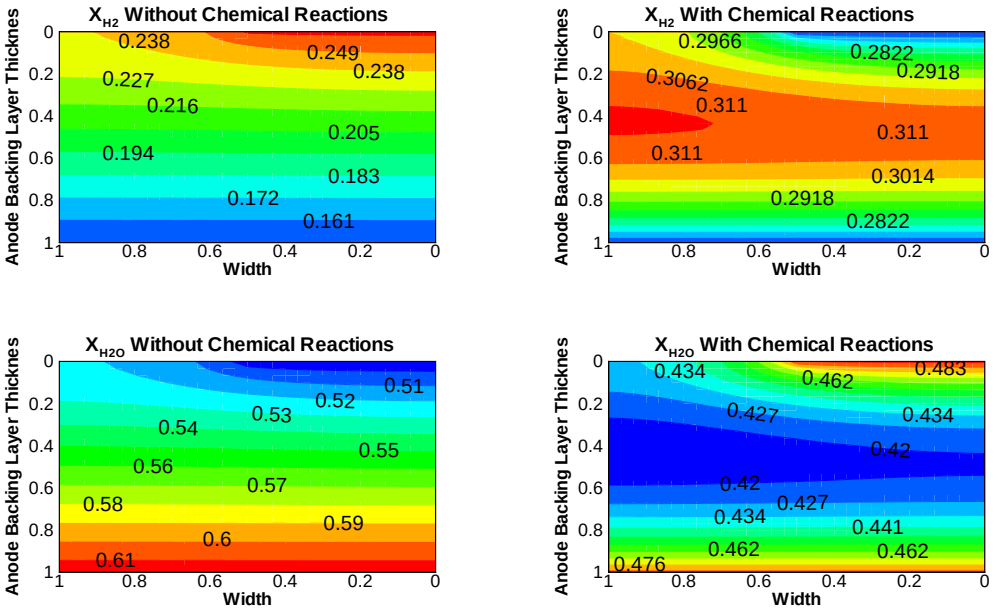

Figure 6.30: Comparison of H_2 and H_2O mole fraction distributions in the anode backing layer with and without consideration of chemical reactions at 0.7 A/cm^2.

difference in the distribution of O_2 mole fraction in the cathode reaction zone when compared to H_2 mole fraction in the anode reaction zone layer. Further, a gradient in O_2 mole fraction can be observed along the width in the cathode reaction zone layer; however, no variation has been observed in the H_2 mole fraction along the width in the anode reaction zone layer, as shown in Figure 6.33. This could be again attributed to small thickness of the cathode relative to the anode.

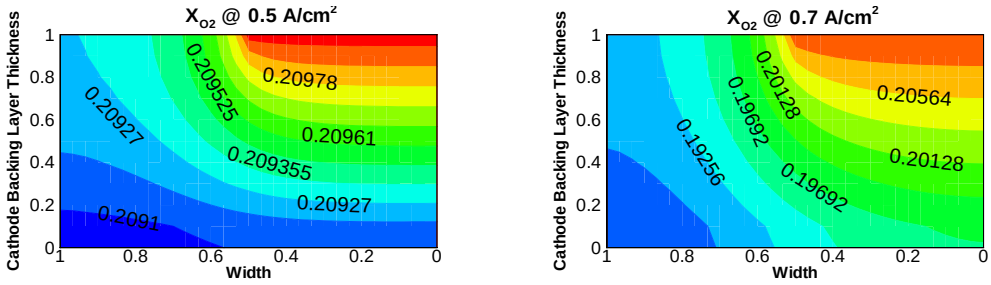

Figure 6.31: Cross-sectional distribution of O_2 mole fraction in the cathode backing layer of an anode-supported SOFC at different current densities.

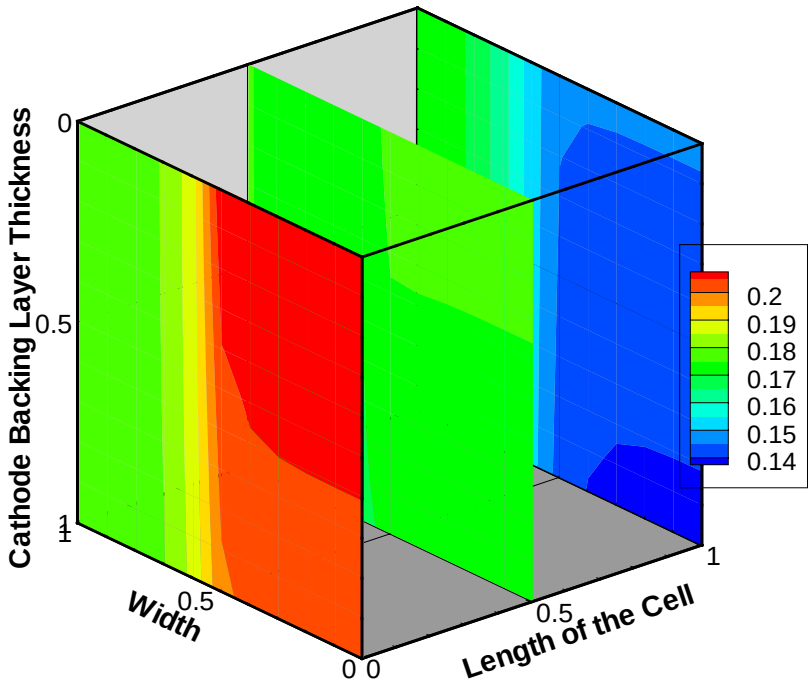

Figure 6.32: 3D slice plot showing the distribution of O_2 mole fraction in the cathode backing layer at different locations along the channel.

6.5.2 Electronic Potential Distribution

A 3D contour plot illustrating the distribution of electronic potential in the anode backing layer at 0.5 A/cm^2 is shown in Figure 6.35. It can be seen that the magnitude of electronic potential increases as we move from the top to the bottom of the backing layer, indicating the direction of current flow from the bottom to the top of backing layer interfacing the solid portion of the interconnect. This is because of production of electrons in the anode reaction zone layer, which results in higher magnitude of electronic potential at the bottom of the backing layer. Moreover, since there is no production or consumption of electrons in the backing layer, uniform distributions of electronic potential are observed at different locations along the thickness of the backing layer, which can be evident from the slice plot shown in Figure 6.28.

The cross-sectional distribution of electronic potential in the anode reaction zone layer is shown in Figure 6.37. Unlike anode backing layer, the distribution of electronic potential exhibits non-

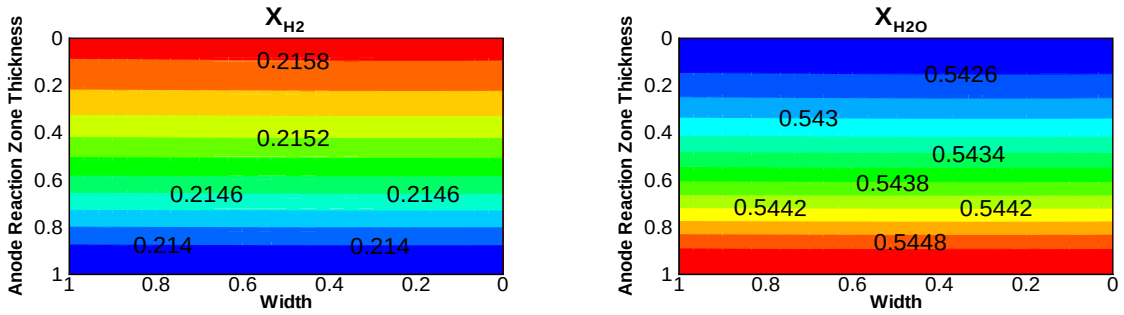

Figure 6.33: Cross-sectional distributions of H_2 and H_2O mole fractions in the anode reaction zone layer of an anode-supported SOFC at 0.5 A/cm^2.

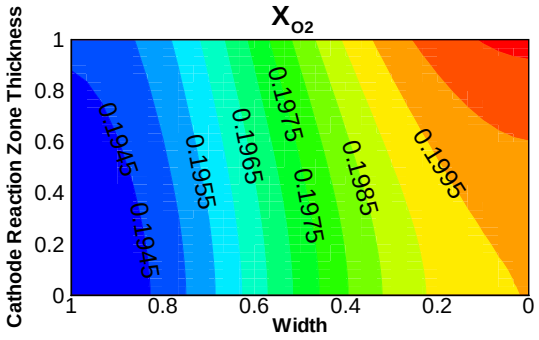

Figure 6.34: Cross-sectional distribution of O_2 mole fraction in the cathode reaction zone layer of an anode-supported SOFC at 0.5 A/cm^2.

uniformity along the thickness and width of the reaction zone layer. This can be attributed to the simultaneous transport and production of electrons in the anode reaction zone layer.

6.5.3 Ionic Potential Distribution

The cross-sectional distribution of ionic potential in the ion-conducting layers is shown in Figure 6.38. The ion-conducting layers are anode reaction zone layer, electrolyte layer and cathode reaction zone layer. Since these layers are placed one underneath the other in the physical domain, the distribution is shown accordingly in the figure. The horizontal-axis represents the width while the vertical-axis represents the thickness of the individual layers. It can be seen that the magnitude of the ionic potential in the cathode reaction zone layer is maximum, wherein oxide ions are produced due to charge transfer reaction. Further, it can be observed from the behavior of the contours

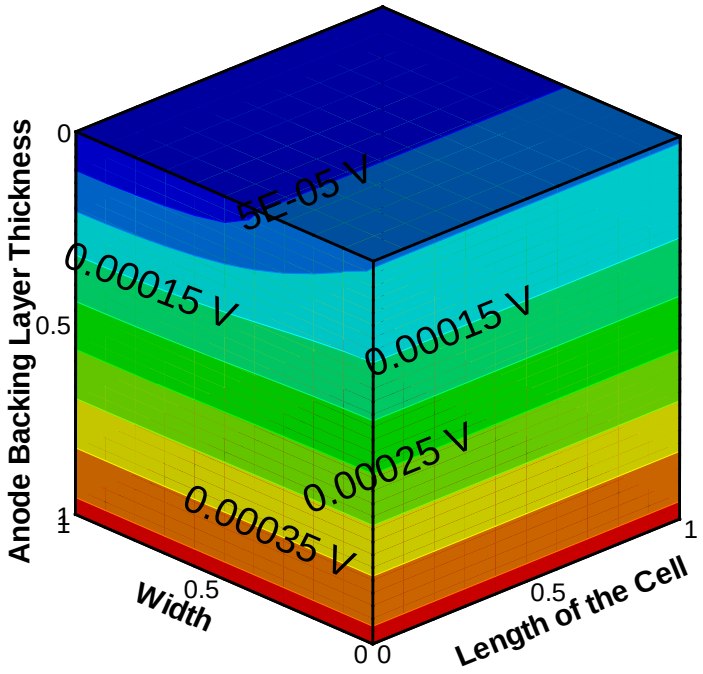

Figure 6.35: 3D contour plot showing the distribution of electronic potential in the anode backing layer at 0.5 A/cm^2.

of ionic potential that the produced oxide ions are transported to the anode reaction zone layer through the electrolyte layer. Moreover, it can be observed that the magnitude of ionic potential reaches its minimum within certain thickness from the interface between the electrolyte and anode reaction zone layer, thereby indicating the spatial limitation of ion transport in the anode reaction zone layer.

6.5.4 Temperature Distribution

Figure 6.39 shows the temperature distribution inside the anode backing and reaction zone layers of an anode-supported SOFC at 0.7 A/cm^2. The operating temperature and pressure were set as 1073 K and 1 atm, respectively. Again, the horizontal-axis represents the width while the vertical axis represents the thickness of the respective layers. The top surface of the anode backing layer is composed of two portions; one is interfacing the interconnect and the other is interfacing the

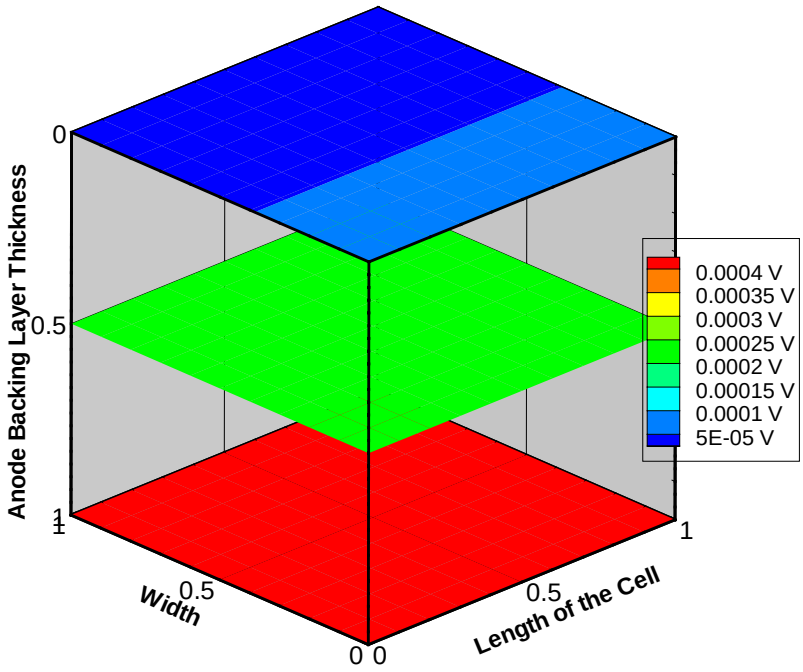

Figure 6.36: 3D slice plot showing the distribution of electronic potential in the anode backing layer at different locations along the thickness of the backing layer.

flow channel. In the present situation, the boundary condition is specified at the top surface of the anode backing layer interfacing the interconnect and the flow channel, equivalent to the operating temperature. The figure shows the difference between the actual and operating temperature in the anode backing and reaction zone layers of an anode-supported SOFC. Since the boundary condition at the top surface of the backing surface is set equal to the operating temperature, the temperature difference is zero at the top surface and increases as we move towards the reaction zone layer. The maximum temperature difference is observed at the interface between the anode reaction zone layer and the electrolyte layer. This is because of heat generation due to electrochemical reaction in addition to Joule heating due to resistance to transport of electrons and ions through the electron- and ion-conducting particles of the anode reaction zone layer, respectively. Additionally, it can be seen that the magnitude of temperature difference within the anode backing and reaction zone layers is negligible, which is attributable to the thinness of the porous layers.

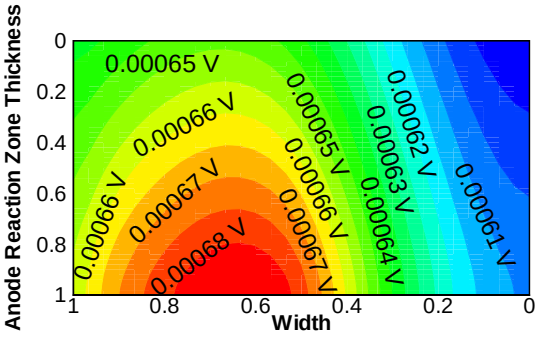

Figure 6.37: Cross-sectional distribution of electronic potential in the anode reaction zone layer.

Similarly, the distribution of temperature difference between the actual and operating temperature in the cathode backing and reaction zone layers is shown in Figure 6.40. Again, the boundary condition at the cathode backing layer surfaces interfacing the interconnect and the flow channel is set equal to the operating temperature. It can be observed that the contour patterns are similar to the anode backing and reaction zone layers. Further, it can be observed that the magnitude of temperature difference in the cathode backing and reaction zone layers is negligible.

6.6 Summary

The solution obtained from numerical implementation of the present SOFC model is presented in this chapter. At first, model validation with measured data sets published in the open literature is presented, which include measured cell performance and measured concentration overpotential. Then, verification of modeling an electrode as two distinct layers is presented. The developed numerical model is then used to predict the performance of two different designs of SOFCs, namely anode-supported and self-supported designs. Initially, the cell performance predicted by 2D anode-supported and 2D self-supported models is presented. Then, a comparison of cell performance between 2D and 3D models of anode-supported and self-supported designs is presented.

It is found that the anode overpotential is the single largest contributor to the cell potential loss at higher current densities in an anode-supported SOFC, followed by the cathode and electrolyte overpotentials. On the other hand, the cathode overpotential is the largest contributor to the

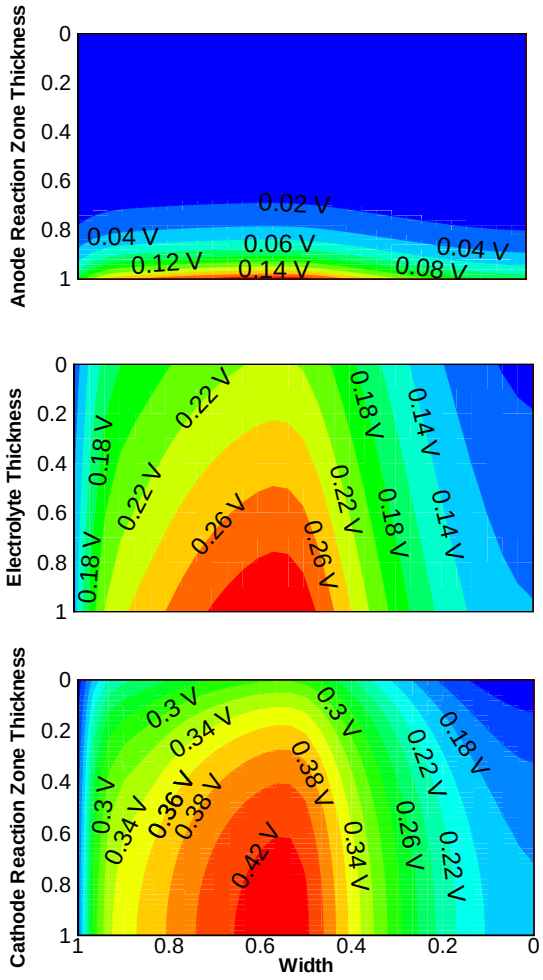

Figure 6.38: Cross-sectional distribution of ionic potential in the ion-conducting layers.

total cell potential loss in self-supported SOFC, while the anode and electrolyte overpotentials are of comparable magnitude. Moreover, the contribution of anode concentration overpotential in an anode-supported SOFC becomes significant when there are no chemical reactions (methane reforming and water-gas shift) in the anode. Conversely, in a self-supported SOFC, the contribution of concentration overpotential to the cell potential loss is negligible. Further, the comparison of 2D and 3D anode-supported models reveals that the performance curves follow similar trend at all the current density range considered in the simulation with 3D model under-predicting the performance.

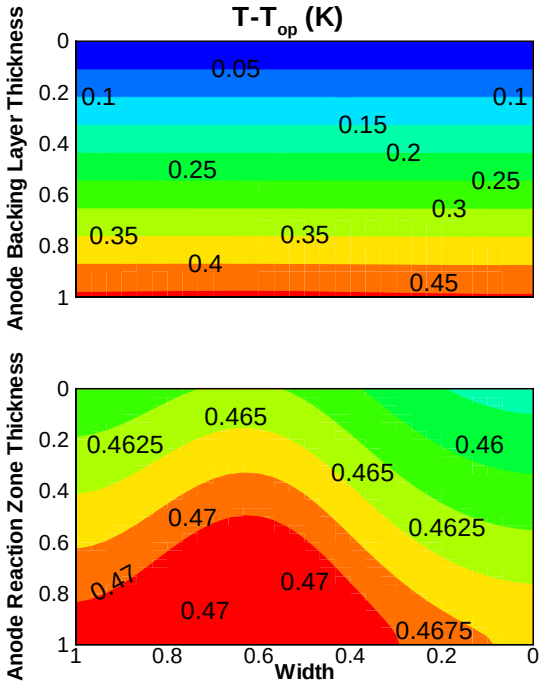

Figure 6.39: Cross-sectional distribution of temperature in the anode backing and reaction zone layers at 0.7 A/cm^2.

Later, the 2D anode-supported model is used to examine the effect of various key operating and design conditions on the performance of an anode-supported SOFC - an exercise to probe the robustness of the model as an optimization tool. It is found that reducing the operating temperature below 1073 K results in a significant drop in the performance of an anode-supported SOFC. In addition, it is found that there is no significant increase in the performance when the anode reaction zone thickness is increased from 30 μm to 50 μm, indicating the spatial limitation of anode reaction zone thickness on cell performance.

Lastly, the developed numerical model is used to predict different phenomena in various layers of an anode-supported SOFC. It is found that the magnitude of H_2 concentration or mole fraction decreases within the thickness of the backing layer at different locations along the channel. This is due to change in H_2 concentration along the channel together with diffusion within the backing layer and electrochemical oxidation reaction in the reaction zone layer interfacing backing layer. In addition, it is found that the consideration of chemical reactions in the anode resulted in increased

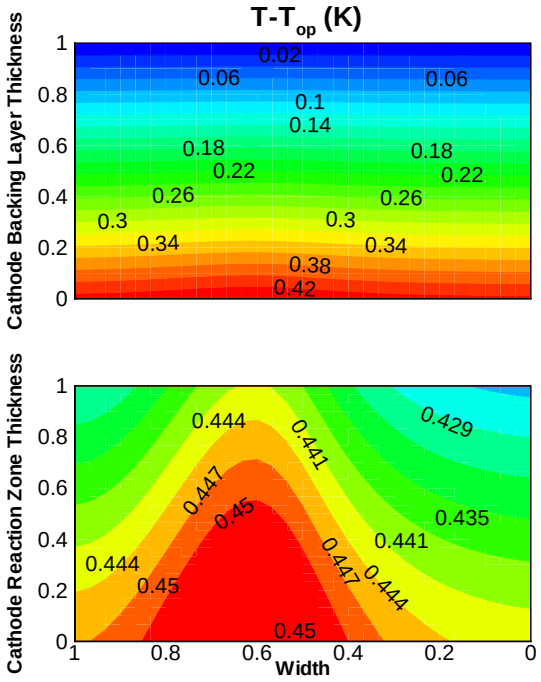

Figure 6.40: Cross-sectional distribution of temperature in the cathode backing and reaction zone layers at 0.7 A/cm^2.

H_2 concentration at the reaction sites in the reaction zone layer. Further, it is found that the magnitude of ionic potential reaches its minimum in the anode reaction zone layer, indicating the spatial limitation of ion transport in the anode reaction zone layer. Finally, it is found that the magnitude of temperature difference in the backing as well as reaction zone layers is negligible.

Chapter 7

Conclusions and Recommendations

7.1 Conclusions

A multi-component and multi-dimensional mathematical model of SOFCs has been developed in this thesis research. The model not only predicts cell performance at different operating and design conditions but also allows computation of interdependent fields of various processes occurring in different layers of SOFC. One of the novelties of the present model is its treatment of electrodes. An electrode in the present model is treated as two distinct layers referred to as the backing layer and the reaction zone layer, thereby serving as a bridge connecting the micro and macro approaches of modeling electrodes. In the micro-modeling approach of modeling electrodes, electrodes are treated as porous structures of electron and ion-conducting particles, and electrochemical reactions are considered to occur throughout the electrodes. Whereas, in the macro-modeling approach, electrodes are modeled as porous structures of electron-conducting particles and electrochemical reactions are considered to occur exclusively at the electrode/electrolyte interfaces, thereby treating the reaction zone layers as boundary conditions. The other important characteristic of the present model is its flexibility in fuel choice, which implies not only pure hydrogen but also any reformate composed of multi-component mixture can be used as a fuel. The modified Stefan-Maxwell equations incorporating Knudsen diffusion are used to model multi-component diffusion in the porous backing and reaction zone layers.

The coupled governing equations of species, charge and energy along with constitutive equations in different layers of the cell are discretized using the finite volume method. The numerical solution is obtained using the developed code written in the computer language of C++ as part of the thesis research. Further, the developed numerical model is validated with multiple measured data sets published in the open literature. An excellent agreement is obtained between the predicted and measured results published in the literature. Furthermore, the distinction of modeling an electrode as two layers in the present model is verified by simulating electrodes as porous structures of electron- and ion-conducting particles, consistent with the micro- modeling approach of treating electrodes.

The numerical model is then used to predict the performance of anode-supported and self-supported SOFCs at different operating and design conditions. In an anode-supported SOFC, anode is the thickest component on which all other layers are deposited, and is designed for intermediate temperature operation. Whereas, in self-supported SOFC, the thickness of each component is such that it can stand by itself, and are suitable for high temperature operation. A parametric study has also been carried out to investigate the effect of various key operating and design parameters on the performance of an anode-supported SOFC.

The following key conclusions can be drawn from the results of this thesis research:

- Based on the simulation of modeling electrodes as porous structures of electron- and ion-conducting particles (micro modeling approach of treating electrodes), it is found that an electrode in an SOFC can be treated as two distinct layer, thereby verified the treatment of electrodes in the present SOFC model.

- In an anode-supported SOFC, the ohmic overpotential is the single largest contributor to the cell potential loss. Also, the cathode and electrolyte overpotentials are not negligible even though their thicknesses are negligible relative to the anode thickness.

- Methane reforming and water-gas shift reactions aid in significantly reducing the concentration overpotential in the thick anode of an anode-supported SOFC.

- Anode-supported SOFC exhibits similar performance as that of self-supported SOFC at reduced operating temperature in the typical operating range (0.5-0.7 A/cm^2); thus, it is found that anode-supported design of SOFCs is the potential design for operating at reduced temperatures.

- Reducing the operating temperature of an anode-supported SOFC from 1073 K to 973 K results in a significant drop in performance; therefore, in order to operate anode-supported SOFCs below 1073 K, the ionic conductivity of the ion-conducting particles need to be enhanced.

- Increasing the anode reaction zone layer beyond certain thickness has no significant effect on the performance of an anode-supported SOFC.

- The distribution of ionic potential in the anode reaction zone layer shows a spatial limitation to ion transport, thereby indicating the influence of anode reaction zone thickness on cell performance.

- The temperature gradients are negligible along the thickness of the backing and reaction zone layers.

7.2 Recommendations

The results obtained from this thesis research suggest several areas for future research:

- Since the boundary conditions for reactant species specified at the interfaces between the gas channels and the backing layers are applicable for constant current density, the channel length considered in the present simulation is small. However, for longer lengths of the channel, the set boundary conditions for reactant species between the gas channels and the backing layers would not be applicable. Therefore, the gas channels need to be integrated into the present model, which require no specified boundary conditions at the interface between

the gas channels and the backing layers. In addition, convection effects can be incorporated into the present electrolyte-electrode-assembly (EEA) model by integrating the gas channels.

- The computational domain of the present model include only the land portions of the interconnects interfacing the backing layers. In order to set the appropriate boundary conditions at the interface between the backing layers and interconnects, the computational domain should include the interconnects. For instance, at the interface between the backing layer and interconnect, the appropriate boundary condition for energy equation is continuous heat flux.

- The present model can be extended to include multiple channels with larger dimensions for large- scale modeling.

- The present single cell model can be used for stack modeling with multiple cells in series.

- The present model can also be integrated with balance-of-plant (BOP) components for system-level modeling.

- The temperature distribution in a component can cause thermal stress effect. Therefore, the present model can be coupled with stress analysis to determine the stress distributions in different components of the cell.

References

[1] C. Wermer, Fuel cell fact sheet, *Environment and Energy Study Institute*, Washington D.C. 20001, 2001.

[2] A. J. Appleby and F. R. Foulkes. *Fuel Cell Handbook*, Van Nostrand reinhold, New York, NY, 583-587, 1989.

[3] X. Li. *Principles of Fuel Cells*, Taylor & Francis, New York, NY 10016, 2006.

[4] I. Dincer. Technical, environmental and exergetic aspects of hydrogen energy systems, *International Journal of Hydrogen Energy*, 27, 265-285, 2002.

[5] K.P. Recknagle, R.E. Williford, L.A. Chick, D.R. Rector, and M.A. Khaleel. Three-dimensional thermo-fluid electrochemical modeling of planar SOFC stacks, *Journal of Power Sources*, 113, 109-114, 2003.

[6] M.A. Khaleel, Z. Lin, P. Singh, W. Surdoval, and D. Collin. A finite element analysis modeling tool for solid oxide fuel cell development: coupled electrochemistry, thermal and flow analysis in MARC, *Journal of Power Sources*, 130, 136-148, 2004.

[7] S.C. Singhal, Solid oxide fuel cells for stationary, mobile, and military application, *Solid State Ionics*, 152-153, 405-410, 2002.

[8] R. Maric, S. Ohara, T. Fukui, H. Yoshida, M. Nishimura, T. Inagaki, and K. Miura. Solid oxide fuel cells with doped lanthanum gallate electrolyte and $LaSrCoO_3$ cathode, and Ni-

samaria-doped ceria cermet anode, *Journal of The Electrochemical Society*, 146(6), 2006-2010, 1999.

[9] J-W. Kim, A.V.Virkar, K-Z. Fung, K. Mehta, and S.C. Singhal. Polarization effects in intermediate temperature, anode-supported solid oxide fuel cells, *Journal of The Electrochemical Society*, 146(1), 69-78, 1999.

[10] A.V. Virkar, J. Chen, C.W. Tanner, J.W. Kim, The role of electrode microstructure on activation and concentration polarizations in solid oxide fuel cells, *Solid State Ionics*, 131, 189-198, 2000.

[11] K. Huang, J-H. Wan, and J.B. Goodenough. Increasing power density of LSGM-based solid oxide fuel cells using new anode materials, *Journal of The Electrochemical Society*, 148, A788-A794, 2001.

[12] P. Aguiar, C.S. Adjiman, and N.P. Brandon, Anode-supported intermediate temperature direct internal reforming solid oxide fuel cell. I: model-based steady-state performance, *Journal of Power Sources*, 138, 120-136, 2004.

[13] J. Yuan, B. Sunden, Analysis of intermediate temperature solid oxide fuel cell transport processes and performance, *Transactions of the ASME, Journal of Heat Transfer*, 127, 1380-1390, 2005.

[14] H. Yakabe, M. Hishinuma, M. Uratani, Y. Matsuzaki, and I. Yasuda. Evaluation and modeling of performance of anode-supported solid oxide fuel cell, *Journal of Power Sources*, 86, 423-431, 2000.

[15] J.H. Hirschenhofer, D.B. Stauffer, R.R. Engelman, and M.G. Klett. *Fuel Cell Handbook*, Fifth Edition, EG & G Services Parsons Inc. 2000.

[16] J. Larminie and A. Dicks. *Fuel Cell Systems Explained*, Wiley, 2000.

[17] U. Pasaogullari and C-Y. Wang. Computational fluid dynamics modeling of solid oxide fuel cells, Electrochemical Engine Center, *Proceedings of SOFC-VIII*, S.C. Singhal and M. Doliya, 1403-1412, 2003.

[18] W. Lehnert, J. Meusinger, and F. Thom. Modelling of gas transport phenomena in SOFC anodes, *Journal of Power Sources*, 87, 57-63, 2000.

[19] R.E. Williford, and L.A. Chick. Surface diffusion and concentration polarization on oxide-supported metal electrocatalyst particles, *Surface Science*, 547, 421-437, 2003.

[20] S. Sunde. Simulations of composite electrodes in fuel cells, *Journal of Electroceramics*, 5, 153-182, 2000.

[21] A. Bieberle, L.P. Meier and L.J. Gauckler. The electrochemistry of Ni pattern anodes used as solid oxide fuel cell model electrodes, *Journal of The Electrochemical Society*, 148, A646-A656, 2001.

[22] G.O. Lauvstad, R. Tunold and S. Sunde. Electrochemical oxidation of CO on Pt and Ni point electrodes in contact with an yttria-stabilized zirconia electrolyte, *Journal of The Electrochemical Society*, 149, E506-E514, 2002.

[23] M. Brown, S. Primdahl and M. Mogensen. Structural/performance relations for Ni/yttria-stabilized zirconia anodes for solid oxide fuel cells, *Journal of The Electrochemical Society*, 147, 475-485, 2000.

[24] R. Maric, S. Ohara, T. Fukui, H. Yoshida, M. Nishimura, T. Inagaki, and K. Miura. Solid oxide fuel cells with doped lanthanum gallate electrolyte and $LaSrCoO_3$ cathode, and Ni-samaria-doped ceria cermet anode, *Journal of The Electrochemical Society*, 146, 2006-2010, 1999.

[25] R.J. Gorte, Recent developments towards commercialization of solid oxide fuel cells, *AIChE Journal*, 51, 2377-2381, 2005.

[26] M.M. Hussain, X. Li, and I. Dincer, Multi-component mathematical model of solid oxide fuel cell anode, *International Journal of Energy Research*, 29, 1083-1101, 2005.

[27] M.M. Hussain, X. Li, and I. Dincer, Mathematical modeling of planar solid oxide fuel cells, *Journal of Power Sources*, 161, 1012-1022, 2006.

[28] S.B. Beale, Y. Li, S.V. Zhubrin, and W. Dong, Computer methods for performance prediction in fuel cells, *Journal of Power Sources*, 118, 79-85, 2003.

[29] P. Costamagna, P. Costa, and V. Antonucci, Micro-modelling of solid oxide fuel cell electrodes, *Electrochimica Acta*, 43, 375-394, 1998.

[30] S.H. Chan, and Z.T. Xia. Anode micro model of solid oxide fuel cell, *Journal of The Electrochemical Society*, 148, A388-A394, 2001.

[31] Z.T Xia, S.H. Chan, and K.A. Khor. An improved anode micro model of SOFC, *Electrochemical and Solid-State Letters*, 7, A63-A65, 2004.

[32] X.J. Chen, S.H. Chan, and K.A. Khor, Simulation of a composite cathode in solid oxide fuel cells, *Electrochimica Acta*, 49, 1851-1861, 2004.

[33] J. Deseure, Y. Bultel, L. Dessemond, and E. Siebert, Theoretical optimisation of a SOFC composite cathode, *Electrochimica Acta*, 50, 2037-2046, 2005.

[34] R. Suwanwarangkul, E. Croiset, M.W. Fowler, P.L Douglas, E. Entchev, and M.A. Douglas. Performance comparison of Fick's, dusty-gas and Stefan-Maxwell models to predict the concentration overpotential of a SOFC anode, *Journal of Power Sources*, 122, 9-18, 2003.

[35] M.M. Hussain, X. Li, and I. Dincer, Modeling and simulation of cathode in solid oxide fuel cells, *Proceeding-The Second International Green Energy Conference*, Oshawa, Ontario, Canada, 2006.

[36] J.H. Nam and D.H. Jeon, A comprehensive micro-scale model for transport and reaction in intermediate temperature solid oxide fuel cells, *Electrochimica Acta*, 51, 3446-3460, 2006.

[37] J.R. Ferguson, J.M. Fiard, and R. Herbin. Three-dimensional numerical simulation for various geometries of solid oxide fuel cells, *Journal of Power Sources*, 58, 109-122, 1996.

[38] R. Krishna, J.A. Wesselingh. The Maxwell-Stefan approach to mass transfer, *Chemical Engineering Science*, 52, 861-911, 1997.

[39] S.H. Chan, K.A. Khor, and Z.T. Xia. A complete polarization model of a solid oxide fuel cell and its sensitivity to the change of cell component thickness, *Journal of Power Sources*, 93, 130-140, 2001.

[40] S. Nagata, A. Momma, T. Kato, and Y. Kasuga. Numerical analysis of output characteristics of tubular SOFC with internal reformer, *Journal of Power Sources*, 101, 60-71, 2001.

[41] S.H. Chan, H.K. Ho, and Y. Tian. Modelling of simple hybrid solid oxide fuel cell and gas turbine power plant, *Journal of Power Sources*, 109, 111-120, 2002.

[42] J. Arriagada, P. Olaussion, A. Selimovic. Artificial neural network simulator for SOFC performance prediction, *Journal of Power Sources*, 112, 54-60, 2002.

[43] H. Yakabe, T. Ogiwara, M. Hishinuma, and I.Yasuda. 3-D model calculation for planar SOFC, *Journal of Power Sources*, 102, 144-154, 2000.

[44] L. Petruzzi, S. Cocchi, and F. Fineschi. A global thermo-electrochemical model for SOFC systems design and engineering, *Journal of Power Sources*, 118, 93-107, 2003.

[45] D. Larrain, J. Van herle, F. Marechal, and D. Favrat. Thermal modeling of a small anode supported solid oxide fuel cell, *Journal of Power Sources*, 118, 367-374, 2003.

[46] H. Zhu, and R.J. Kee. A general mathematical model for analyzing the performance of fuel-cell membrane-electrode assemblies, *Journal of Power Sources*, 117, 61-74, 2003.

[47] W. Dong, S.B. Beale, and R.J. Boersma. Computational modelling of solid oxide fuel cells, *Proceedings of the CFD society of Canada*, 382-387, 2001.

[48] T. Ackmann, L.G.J. de Haart, W. Lehnert, and D. Stolten. Modeling of mass transport in planar substrate type SOFCs, *Journal of The Electrochemical Society*, 150, A783-A789, 2003.

[49] J.D.J. VanderSteen, and J.G.Pharoah. The effect of radiation heat transfer in solid oxide fuel cell modelling, *Combustion Institute/Canadian Section, Spring Technical Meeting*, Queen's University, May 9-12, 2004.

[50] J.D.J. VanderSteen, and J.G.Pharoah. Modeling radiation heat transfer with participating media in solid oxide fuel cells, *Transactions of the ASME, Journal of Fuel Cell Science and Technology*, 3, 62-67, 2006.

[51] D.L. Damm, and A.G. Federov. Spectral radiative heat transfer analysis of the planar SOFC, *Transactions of the ASME, Journal of Fuel Cell Science and Technology*, 2, 258-262, 2005.

[52] K.J. Daun, S.B. Beale, F. Liu, and G.J. Smallwood. Radiation heat transfer in planar SOFC electrolytes, *Journal of Power Sources*, 157, 302-310, 2006.

[53] J. Yuan and B. Sunden, Analysis of intermediate temperature solid oxide fuel cell transport processes and performance, *Transactions of the ASME, Journal of Heat Transfer*, 127, 1380-1390, 2005.

[54] J. Yuan and B. Sunden, Analysis of chemically reacting transport phenomena in an anode duct of intermediate temperature SOFCs, *Transactions of the ASME, Journal of Fuel Cell Science and Technology*, 3, 89-98, 2006.

[55] R. Suwanwarangkul, E. Croiset, E. Entchev, S. Charjrochkul, M.D. Pritzker, M.W. Fowler, P.L Douglas, S. Chewathanakup, and H. Mahaudom. Experimental and modeling study of solid oxide fuel cell operating with syngas fuel, *Journal of Power Sources*, 161, 308-322, 2006.

[56] R.B. Bird, W.E. Stewart, and E.N. Lightfoot. *Transport Phenomena*, John Wiley & Sons, 1960.

[57] S. Litster and N. Djilali. Two-phase transport in porous gas diffusion electrodes, *Institute for Integrated Energy Systems*, University of Victoria, Canada, 2004.

[58] E.L Cussler. *Diffusion-Mass transfer in fluid systems*, Cambridge University Press, New York, 1997.

[59] W. Kast and C.R. Hohenthanner. Mass transfer within the gas-phase of porous media, *International Journal of Heat and Mass Transfer*, 43, 807-823, 2000.

[60] S. Biloe and S. Mauran. Gas flow through highly porous graphite matrices, *Carbon*, 41, 525-537, 2003.

[61] B.A. Haberman, and J.B. Young, Three dimensional simulation of chemically reacting gas flows in the porous support structure of an integrated-planar solid oxide fuel cell, *International Journal of Heat and Mass Transfer*, 47, 3617-3629, 2004.

[62] B. Todd, and J.B. Young, Thermodynamic and transport properties of gases for use in solid oxide fuel cell modeling, *Journal of Power Sources*, 110, 186-200, 2002.

[63] T. Kenjo, S. Osawa, and K. Fujikawa, High temperature air cathodes containing ion conductive oxides, *Journal of The Electrochemical Society*, 138, 349-355, 1991.

[64] T. Kenjo, and M. Nishiya, $LaMnO_3$ air cathodes containing ZrO_2 electrolyte for high temperature solid oxide fuel cells, *Solid State Ionics*, 57, 295-302, 1992.

[65] J. Abel, A.A. Kornyshev, and W. Lehnert, Correlated resistor network study of porous solid oxide fuel cell anodes , *Journal of The Electrochemical Society*, 144, 4253-4259, 1997.

[66] D.H. Jeon, J.H. Nam, and C-J Kim, A random resistor network analysis on anodic performance enhancement of solid oxide fuel cells by penetrating electrolyte structures, *Journal of Power Sources*, 139, 21-29, 2005.

[67] A.S. Ioselevich and A.A. Kornyshev. Phenomenological theory of solid oxide fuel cell anode, *Fuel Cells*, 1, 40-65, 2001.

[68] M. Ihara, T. Kusano and C. Yokohama. Competitive adsorption reaction mechanism of Ni/yttria-stabilized zirconia cermet anode in H_2-H_2O solid oxide fuel cells, *Journal of The Electrochemical Society*, 148, A209-A219, 2001.

[69] X. Wang, N. Nakagawa and K. Kato. Anodic polarization related to the ionic conductivity of zirconia at Ni-zirconia/zirconia electrodes, *Journal of The Electrochemical Society*, 148, A565-A569, 2001.

[70] J. Newman, and K.E. Thomas-Alyea, *Electrochemical Systems (3rd edn)*, Wiley: New Jersey, 2004.

[71] J. Fleig. On the width of the electrochemically active region in mixed conducting solid oxide fuel cell cathodes, *Journal of Power Sources*, 105, 228-238, 2002.

[72] J. Van Herle, A.J. McEvoy and K.R. Thampi. A study on the $La_{1-x}Sr_xMnO_3$ oxygen cathode, *Electrochimica Acta*, 41, 1447-1454, 1996.

[73] A. Mitterdorfer and L.J. Gauckler. $La_2Zr_2O_7$ formation and oxygen reduction kinetics of the $La_{0.85}Sr_{0.15}Mn_yO_3$, $O_{2(g)}$—YSZ system, *Solid State Ionics*, 111, 185-218, 1998.

[74] E.P. Murray, T. Tsai and S.A. Barnett. Oxygen transfer processes in $(La, Sr)MnO_3/Y_2O_3 - stabilizedZrO_2$ cathodes: an impedance spectroscopy study, *Solid State Ionics*, 110, 235-243, 1998.

[75] M.J. Jorgensen and M. Mogensen. Impedance of solid oxide fuel cell LSM/YSZ composite cathodes, *Journal of The Electrochemical Society*, 148, A433-A442, 2001.

[76] A. Endo, M. Ihara, H. Komiyama and K. Yamada. Cathodic reaction mechanism for dense Sr-doped lanthanum manganite electrodes, *Solid State Ionics*, 86-88, 1191-1195, 1996.

[77] H. Kamata, A. Hosaka, J. Mizusaki and H. Tagawa. High temperature electrocatalytic properties of the SOFC air electrode $La_{0.8}Sr_{0.2}MnO_3/YSZ$, *Solid State Ionics*, 106, 237-245, 1998.

[78] S.P. Jiang, J.G. Love and Y. Ramprakash. Electrode behaviour at $(La, Sr)MnO_3/Y_2O_3-ZrO_2$ interface by electrochemical impedance spectroscopy, *Journal of Power Sources*, 110, 201-208, 2002.

[79] M.J. Ostergard and M. Mogensen. ac impedance study of the oxygen reduction mechanism on $La_{1-x}Sr_xMnO_3$ in solid oxide fuel cells, *Electrochimica Acta*, 38, 2015-2020, 1993.

[80] S. Wang, Y. Jiang, Y. Zhang, J. Yan and W. Li. The role of 8 mol % yttria stabilized zirconia in the improvement of electrochemical performance of lanthanum manganite composite electrodes, *Journal of The Electrochemical Society*, 145, 1932-1939, 1998.

[81] R. Bove, and S. Ubertini, Modeling solid oxide fuel cell operation: approaches, techniques and results, *Journal of Power Sources*, 159, 543-559, 2006.

[82] U.G. Bossel, Facts and figures, final report on SOFC data, IEA report *Swiss Federal Office of Energy*, Operating Task II, Berne, 1992.

[83] S.V. Patankar. *Numerical Heat Transfer and Fluid Flow* (series in computational methods in mechanics and thermal sciences), McGraw-Hill, New York, 1980.

[84] R. Peyret and T.D. Taylor. *Computational Methods for Fluid Flow*, Springer-Verlag, New York, 1983.

[85] H.K. Versteeg and W. Malalasekera. *An Introduction to Computational Fluid Dynamics The Finite Volume Method*, John Wiley & sons Inc, New York, 1995.

[86] J.M. Fiard and R. Herbin. Comparison between finite volume and finite element methods for an elliptic system arising in electrochemical engineering, *Computational Methods in Applied Mechanics and Engineering*, 115, 315-338, 1994.

[87] N.R. Amundson, E. Morano and R. Sanders. Techniques for the numerical solution of steady reaction-diffusion systems employing Stefan-Maxwell diffusion, *East-West Journal of Numerical Mathematics*, 6, 9-25, 1998.

[88] J.M. Stockie, K. Promislow and B.R. Wetton. A finite volume method for multicomponent gas transport in a porous fuel cell electrode, *International Journal for Numerical Methods in Fluids*, 41, 577-599, 2003.

[89] B. Todd. Mass transfer in solid oxide fuel cell electrodes, *2nd International Conference on Heat Transfer, Fluid Mechanics and Thermodynamics*, Victoria, Zambia, 2003.

[90] W.A. Rogers, R.S. Gemmen, C. Johnson, M. Prinkey, M. Shahnam, Validation and application of a CFD-based model for solid oxide fuel cells and stacks, *Fuel Cell Science, Engineering and Technology, ASME*, 517-520, 2003.

[91] M. Iwata, T. Hikosaka, M. Morita, T. Iwanari, K. Ito, K. Onda, Y. Esaki, Y. Sakaki, S. Nagata, Performance analysis of planar-type unit SOFC considering current and temperature distributions, *Solid State Ionics*, 132, 297-308, 2000.

[92] M.K. Alkhateeb, S.J. Parulekar, J.R. Selman, and S. Al-Hallaj, Macrohomogenous modeling of porous SOFC electrodes, *Electrochemical Society Proceedings Volume 2005-07*, 738-748, 2005.

[93] N.Q. Minh, and T. Takahashi, *Science and Technology of Ceramic Fuel Cells*, Elsevier Science B.V., Amsterdam, The Netherlands, 1995.

[94] R.E. Williford, L.A. Chick, G.D. Maupin, and S.P. Simner, Diffusion limitations in the porous anodes of SOFCs, *Journal of The Electrochemical Society*, 150, A1067-A1072, 2003.

[95] I. Drescher, W. Lehnert, and J. Meusinger, Structural properties of SOFC anodes and reactivity, *Electrochimica Acta*, 43, 3059-3068, 1998.

[96] Y.A. Cengel, and M.A. Boles. *Thermodynamics- An Engineering Approach*, Third Edition, McGraw-Hill, 1998.